NUREG/CR-4667, Vol. 24
ANL-98/6

Environmentally Assisted Cracking in Light-Water Reactors

Semiannual Report
January 1997 - June 1997

Manuscript Completed: March 1998
Date Published: April 1998

Prepared by
O. K. Chopra, H. M.Chung, E. E. Gruber/ANL
T. M. Karlsen/OECD
T. F. Kassner, J.-H. Park, W. E. Ruther/ANL
J. E. Sanecki, W. J. Shack, J. L. Smith/ANL
W. K. Soppet, R.V. Strain, N. J. Zaluzec/ANL

Argonne National Laboratory
9700 South Cass Avenue
Argonne, IL 60439

Subcontractor:

OECD Halden Reactor Project
Halden N-1751
Norway

M.B. McNeil, NRC Project Manager

DISTRIBUTION OF THIS DOCUMENT IS UNLIMITED

Prepared for
Division of Engineering Technology
Office of Nuclear Regulatory Research
U.S. Nuclear Regulatory Commission
Washington, DC 20555-0001
NRC Job Code W6610

MASTER

Previous Documents in Series

Environmentally Assisted Cracking in Light Water Reactors Semiannual Report April—September 1985, NUREG/CR-4667 Vol. I, ANL-86-31 (June 1986).

Environmentally Assisted Cracking in Light Water Reactors Semiannual Report October 1985—March 1986, NUREG/CR-4667 Vol. II, ANL-86-37 (September 1987).

Environmentally Assisted Cracking in Light Water Reactors Semiannual Report April—September 1986, NUREG/CR-4667 Vol. III, ANL-87-37 (September 1987).

Environmentally Assisted Cracking in Light Water Reactors Semiannual Report October 1986—March 1987, NUREG/CR-4667 Vol. IV, ANL-87-41 (December 1987).

Environmentally Assisted Cracking in Light Water Reactors Semiannual Report April—September 1987, NUREG/CR-4667 Vol. V, ANL-88-32 (June 1988).

Environmentally Assisted Cracking in Light Water Reactors Semiannual Report October 1987—March 1988, NUREG/CR-4667 Vol. 6, ANL-89/10 (August 1989).

Environmentally Assisted Cracking in Light Water Reactors Semiannual Report April—September 1988, NUREG/CR-4667 Vol. 7, ANL-89/40 (March 1990).

Environmentally Assisted Cracking in Light Water Reactors Semiannual Report October 1988—March 1989, NUREG/CR-4667 Vol. 8, ANL-90/4 (June 1990).

Environmentally Assisted Cracking in Light Water Reactors Semiannual Report April—September 1989, NUREG/CR-4667 Vol. 9, ANL-90/48 (March 1991).

Environmentally Assisted Cracking in Light Water Reactors Semiannual Report October 1989—March 1990, NUREG/CR-4667 Vol. 10, ANL-91/5 (March 1991).

Environmentally Assisted Cracking in Light Water Reactors Semiannual Report April—September 1990, NUREG/CR-4667 Vol. 11, ANL-91/9 (May 1991).

Environmentally Assisted Cracking in Light Water Reactors Semiannual Report October 1990—March 1991, NUREG/CR-4667 Vol. 12, ANL-91/24 (August 1991).

Environmentally Assisted Cracking in Light Water Reactors Semiannual Report April—September 1991, NUREG/CR-4667 Vol. 13, ANL-92/6 (March 1992).

Environmentally Assisted Cracking in Light Water Reactors Semiannual Report October 1991—March 1992, NUREG/CR-4667 Vol. 14, ANL-92/30 (August 1992).

Environmentally Assisted Cracking in Light Water Reactors Semiannual Report April—September 1992, NUREG/CR-4667 Vol. 15, ANL-93/2 (June 1993).

Environmentally Assisted Cracking in Light Water Reactors Semiannual Report October 1992—March 1993, NUREG/CR-4667 Vol. 16, ANL-93/27 (September 1993).

Environmentally Assisted Cracking in Light Water Reactors Semiannual Report April—September 1993, NUREG/CR-4667 Vol. 17, ANL-94/26 (June 1994).

Environmentally Assisted Cracking in Light Water Reactors Semiannual Report October 1993—March 1994, NUREG/CR-4667 Vol. 18, ANL-95/2 (March 1995).

Environmentally Assisted Cracking in Light Water Reactors Semiannual Report April—September 1994, NUREG/CR-4667 Vol. 19, ANL-95/25 (September 1995).

Environmentally Assisted Cracking in Light Water Reactors Semiannual Report October 1994—March 1995, NUREG/CR-4667 Vol. 20, ANL-95/41 (January 1996).

Environmentally Assisted Cracking in Light Water Reactors Semiannual Report April—December 1995, NUREG/CR-4667 Vol. 21, ANL-96/1 (July 1996).

Environmentally Assisted Cracking in Light Water Reactors Semiannual Report January 1996—June 1996, NUREG/CR-4667 Vol. 22, ANL-97/9 (June 1997).

Environmentally Assisted Cracking in Light Water Reactors Semiannual Report July 1996—December 1996, NUREG/CR-4667 Vol. 23, ANL-97/10 (October 1997).

Environmentally Assisted Cracking in Light Water Reactors
Semiannual Report January 1997–June 1997

by

O. K. Chopra, H. M. Chung, E. E. Gruber, T. F. Kassner, J.-H. Park, W. E. Ruther,
J. E. Sanecki, W. J. Shack, J. L. Smith, W. K. Soppet, R. V. Strain, and N. J. Zaluzec
(Argonne National Laboratory)

T. M. Karlsen
(OECD Halden Reactor Project)

Abstract

This report summarizes work performed by Argonne National Laboratory on fatigue and environmentally assisted cracking (EAC) in light water reactors from January 1997 to June 1997. Topics that have been investigated include (a) fatigue of carbon, low–alloy, and austenitic stainless steels (SSs) used in reactor piping and pressure vessels, (b) irradiation–assisted stress corrosion cracking of Types 304 and 304L SS, and (c) EAC of Alloys 600 and 690. Fatigue tests were conducted on ferritic and austenitic SSs in water that contained various concentrations of dissolved oxygen (DO) to determine whether a slow strain rate applied during various portions of a tensile–loading cycle is equally effective in decreasing fatigue life. Slow–strain–rate–tensile tests were conducted in simulated boiling water reactor (BWR) water at 288°C on SS specimens irradiated to a low fluence in the Halden reactor and the results were compared with similar data from a control–blade sheath and neutron-absorber tubes irradiated in BWRs to the same fluence level. Crack–growth–rate tests were conducted on compact–tension specimens from several heats of Alloys 600 and 690 in low-DO, simulated pressurized water reactor environments.

Contents

Figures

Tables

Executive Summary

Environmental Effects on Fatigue Strain-versus-Life (S–N) Behavior of Primary Pressure Boundary Materials

Cyclic loadings on a structural component occur because of changes in the mechanical and thermal loadings as the system goes from one load set (e.g., pressure, temperature, moment, and force loading) to any other load set. For each pair of load sets, an individual fatigue usage factor is determined by the ratio of the number of cycles anticipated during the lifetime of the component to the allowable cycles. Figures I–9.1 through I–9.6 of Appendix I to Section III of the ASME Boiler and Pressure Vessel Code specify fatigue design curves that define the allowable number of cycles as a function of applied stress amplitude. The cumulative usage factor (CUF) is the sum of the individual usage factors, and the ASME Code Section III requires that the CUF at each location must not exceed 1.

Subsection NB–3121 of Section III of the Code states that the data on which the fatigue design curves are based did not include tests in the presence of corrosive environments that might accelerate fatigue failure. Article B–2131 in Appendix B to Section III states that the owner's design specifications should provide information on any reduction to fatigue design curves necessitated by environmental conditions. Recent fatigue strain–versus–life (S–N) data illustrate potentially significant effects of light water reactor (LWR) coolant environments on the fatigue resistance of carbon steels (CS) and low–alloy steels (LAS). Under certain conditions of loading and environment, fatigue lives of carbon steels can be a factor of 70 lower in the environment than those in air. These results raise the issue of whether the fatigue design curves in Section III are appropriate for the purposes intended and whether they adequately account for environmental effects on fatigue behavior.

This report summarizes work performed by Argonne National Laboratory on fatigue of CS and LAS steels in simulated LWR environments. The existing fatigue S–N data, foreign and domestic, for these steels have been evaluated to establish the effects of various material and loading variables such as steel type, strain range, strain rate, temperature, sulfur content in steel, orientation, and dissolved oxygen (DO) level in water on the fatigue lives of these steels. The influence of reactor environments on the formation and growth of short fatigue cracks is discussed. Decreases in fatigue lives of these steels in high–DO water are caused primarily by the effect of environment on growth of short cracks < 100 μm in depth. The material and loading parameters that influence fatigue life in LWR environments are defined. Fatigue life is decreased significantly when five conditions are satisfied simultaneously, viz., applied strain range, service temperature, DO in water, and sulfur content in steel are above a threshold level, and loading strain rate is below a threshold value. Statistical models have been developed for estimating the fatigue life of these steels in LWR environments. The significance of the effect of environment on the current Code design curve is evaluated. Sample fatigue evaluations have been performed for CS and LAS components.

Irradiation-Assisted Stress Corrosion Cracking

Slow-strain-rate-tensile (SSRT) tests in simulated BWR water at 288°C were completed for 14 SS alloys that were irradiated to a fluence of $\approx 0.45 \times 10^{21}$ $\text{n}\cdot\text{cm}^{-2}$ (E >1 MeV) at 288°C in helium in the Halden reactor. Fractographic analysis by scanning electron microscopy (SEM) has been also completed to determine susceptibilities to intergranular and transgranular stress corrosion cracking (IGSCC and TGSCC). Heat-to-heat variations in susceptibilities to IGSCC and TGSCC were very significant, indicating that heat-to-heat variation in crack growth rate also will be strong. High-purity (HP) heats of Types 304 and 316 SS exhibited less ductility during SSRT tests and were more susceptible to IGSCC than commercial-purity (CP) heats. This behavior is similar to that observed for BWR neutron-absorber tubes fabricated from HP heats of Type 304 SS. Type 304 SS alloys that contain either high levels of oxygen or sulfur exhibit low ductility, even in the nonirradiated condition.

Total elongation of the irradiated specimens tested in simulated BWR water were correlated with the combined concentrations of nitrogen and silicon of the alloy. Alloys that contain low levels of nitrogen (<0.01 wt.%) and silicon (<0.5 wt.%) exhibited low ductility, irrespective of the carbon content. This trend was also valid in terms of susceptibility to TGSCC; alloys that contain low levels of nitrogen and silicon exhibited high susceptibility to TGSCC. Alloys that contain high silicon (≈1.2 wt.%) exhibited low susceptibility to TGSCC and a high ductility despite a very low nitrogen content of ≈0.001 wt.%. A higher silicon content appears to be conducive to less irradiation-induced hardening, a lower density of Frank loops, a lower stacking fault energy, and a lower susceptibility to TGSCC and IGSCC after irradiation. When the nitrogen content was >≈0.015 wt.%, neither low ductility nor high susceptibility to TGSCC was observed regardless of silicon content. As fluence increases, high susceptibility to IGSCC was observed in an alloy that exhibits high susceptibility to TGSCC at low fluence. Therefore, it is desirable to avoid alloys that contain <0.01 wt.% nitrogen and <0.5 wt.% silicon.

To provide a better understanding of cracking of BWR core shroud welds, shielded-metal-arc (SMA) welds were prepared from Types 304, 304L, and 316 SS to simulate BWR core-shroud welds. Microchemistry and microstructure of the welds were then characterized by secondary ion mass spectroscopy (SIMS) and transmission electron microscopy (TEM). Significant contamination by oxygen and fluorine was observed in the heat-affected zones (HAZs) of all of the SMA welds examined, whereas contamination in gas-tungsten-arc (GTA) welds was insignificant. Small precipitates rich in calcium, oxygen, and fluorine were also observed near the fusion line of the SMA welds. Contamination by these impurities originates from the coating on the welding electrode and the air atmosphere. Essentially similar contamination was also observed in the HAZ of a low-carbon Type 304L SS core shroud weld that cracked in BWR-C.

Cracking incidents in Type 304L SS core shrouds has increased significantly in recent years, and many investigators have suspected that significant grain-boundary chromium depletion can occur in the HAZ of Type 304L SS welds during long-term irradiation under LWR conditions even if the total accumulated fluence is low. However, results from characterization by field-emission-gun advanced analytical electron microscopy (FEG-AAEM) showed neither grain-boundary carbides nor grain-boundary chromium depletion in the HAZ of the Type 304L BWR-C core shroud weld. A similar TEM characterization that was conducted subsequently on laboratory-produced SMA welds of the Type 304 SSs also revealed no grain-boundary carbides, and hence classical thermal sensitization, even in the high-carbon material. Analysis of a specimen from the HAZ of a core shroud weld fabricated from Type 304 SS (0.063 wt.% carbon) that had cracked in BWR-D again revealed that grain-boundary carbides were absent. We believe that contamination by oxygen can occur during SMA or submerged-arc (SA) welding of a core shroud and it is conducive to preferential binding of chromium atoms to oxygen atoms in the weld HAZ, which thereby prevents the formation of chromium-rich $M_{23}C_6$ carbides even in high-carbon Type 304 SS. In view of these observations, it is difficult to explain BWR core shroud cracking (fabricated with either Type 304 or 304L SS) on the basis of either the thermal sensitization or grain-boundary chromium-depletion model of IASCC. At the same time, it is important to obtain a crack growth data base from SMA- or SA-welded core shrouds to compare with those from TIG-welded or thermally sensitized materials (i.e., materials sensitized in laboratory).

Fluorine content in the heat-affected zone was higher on grain boundaries than in the base metal of core shroud welds. Several literature reports indicate that weld-related fluorine contamination exacerbates the susceptibility of welds to IGSCC during bend-beam tests in water. Because of the direct association of oxygen and fluorine contamination, this type of IGSCC has been termed "oxyfluorine-assisted" SCC. Thus, the failure of Type 304L and Type 304 SS core shrouds could be explained by a model based on oxyfluorine-assisted SCC, in which a synergism among oxygen, chromium, and fluorine plays a primary role. According to the model, susceptibility to IGSCC is influenced strongly by oxygen and fluorine on grain boundaries, because higher oxygen is conducive to more chromium bonded to oxygen on the grain boundaries. Hence, higher fluoride ion and lower chromium ion concentrations in the crack-tip water allow the strong catalytic role of fluoride on metal dissolution at the crack tip. The presence of calcium oxyfluoride precipitates appears to exacerbate the process because the precipitates dissolve readily in water, thereby releasing fluorine more rapidly in the crack-tip water.

Environmentally Assisted Cracking of Alloys 600 and 690 in Simulated LWR Water

Corrosion–fatigue experiments were conducted on compact–tension specimens of solution-annealed and thermally treated specimens of a low-carbon-content heat of Alloy 600 in simulated PWR water at 320°C to investigate the effects of load ratio and maximum stress intensity on crack growth rates (CGRs). Crack growth experiments were also conducted on solution-annealed specimens of Alloy 600 and 690 in simulated PWR water at 289°C. "Best-fit" correlations for the CGR of alloys in water versus ΔK were obtained for each specimen and for the combined data from several specimens of the low-carbon Alloy 600 material with various heat treatments. The effect of low-DO PWR water on the CGRs of this alloy relative to that in air was determined from the ratio of the CGRs in water at 320°C and in air at 289°C. This information was compared with similar data at 289°C for this heat of Alloy 600 in simulated BWR water that contained 300 ppb DO.

Over the stress intensity range ΔK of ≈ 3 to 47 $\text{MPa}\cdot\text{m}^{1/2}$, CGRs of the low-carbon heat of Alloy 600 were higher in simulated BWR than in PWR water. The ratios of the CGRs in water and air were >1 at ΔK values <18 and <10 $\text{MPa}\cdot\text{m}^{1/2}$ in BWR and PWR water, respectively, and were lower in water than in air (ratio <1) at higher values of ΔK. For high load ratios (i.e., $R \geq 0.95$) and a K_{max} of ≈ 40 $\text{MPa}\cdot\text{m}^{1/2}$, which correspond to ΔK values of ≤ 2 $\text{MPa}\cdot\text{m}^{1/2}$, the rates in water are higher than in air by a factor of ≈ 10. Intuitively, the results are consistent with premise that CGRs of nickel-base alloys and austenitic SS increase with DO concentration in high-temperature water. The results suggest that temperature (320 versus 289°C) plays a lesser role in crack propagation because the CGRs are lower in simulated PWR than in BWR water in these experiments despite the higher temperature of the low-DO PWR environment, which also contains 23-39 $\text{cm}^3\cdot\text{kg}^{-1}$ H_2, 1200 ppm boron (as H_3BO_3), and 2.25

ppm lithium (as LiOH). Based on results from four specimens in each environment, heat treatment conditions did not have a significant effect on the CGRs in simulated PWR or BWR water.

The morphology of corrosion-fatigue cracks in the Alloy 600 and 690 specimens was transgranular because of the strong contribution of mechanical cyclic loading in tests at load ratios of 0.1-0.8 and because of the relatively small degree of crack extension that occurred in tests at load ratios >0.8.

Acknowledgments

The authors thank W. F. Burke, T. M. Galvin, J. Tezak, and D. R. Perkins for their contributions to the experimental effort. This work is sponsored by the Office of Nuclear Regulatory Research, U.S. Nuclear Regulatory Commission, under Job Code W6610; Program Manager: Dr. M. B. McNeil.

1 Introduction

The U.S. Nuclear Regulatory Commission (NRC) and its predecessor, the U.S. Atomic Energy Commission, have conducted research programs that address aging of reactor components. The results of the research have been used to evaluate and establish regulatory guidelines to ensure acceptable levels of reliability for light water reactor (LWR) components. The products of this program have been technical reports, methodologies for evaluating licensee submittals, and other inputs to the regulatory process. The results have led to the resolution of regulatory issues, as well as the development, validation, and improvement of regulations and regulatory guides. The present research on the effects of simulated reactor coolant environments on cracking of reactor components was initiated to resolve remaining critical technical issues related to cracking phenomena in LWR components. Initially, this project addressed cracking of boiling water reactors (BWR) pipes, and, subsequently, in response to the NRC Division of Nuclear Reactor Regulation (NRR) requests for assistance in dealing with developing cracking problems in aging reactors, the focus has shifted to other problems in environmentally assisted cracking (EAC) of LWR components.

The overall objective of this program is to provide data and physical models to be used by the NRC staff in assessing environmentally assisted degradation of primary pressure boundary components in LWRs. The research is divided into five tasks:

(a) *Environmental effects on fatigue, crack growth, and stress corrosion cracking*
Fatigue and EAC of piping, pressure vessels, and core components in LWRs are important concerns in plant operation and for extended reactor lifetimes. The degradation processes in U.S. reactors include fatigue, intergranular stress corrosion cracking (IGSCC), and propagation of fatigue or stress corrosion cracks that initiate in the weld-sensitized heat-affected zone (HAZ) of stainless steel (SS) components. Occurrences of mechanical–vibration– and thermal–fluctuation–induced fatigue failures in LWR plants have also been documented. The objective of this task is to improve fatigue design curves and assess the additivity of fatigue damage in piping and vessel steels under load histories typical of LWR components. The results of this work will be used to assess industry fatigue evaluations related to license renewal.

(b) *Component vulnerability to irradiation-assisted stress corrosion cracking*
Irradiation–assisted stress corrosion cracking (IASCC) of in–core components of both BWRs and pressurized-water reactors (PWRs) is becoming a more common problem as reactors age. The general pattern of the observed failures indicates that, as nuclear plants age and neutron fluence increases, many apparently nonsensitized austenitic materials become susceptible to intergranular failure by IASCC. Some of these failures have been reported for components subjected to relatively low or negligible stress levels, e.g., control–blade sheaths and handles and instrument dry tubes of BWRs. Although most failed components can be replaced, some safety–significant structural components, such as the BWR top guide, core plate, and shroud, would be very difficult or impractical to replace. The objective of this task is to provide data and models that are needed to assess industry analyses of the likelihood of degradation and failure of core internal components due to IASCC, and to evaluate licensee submissions concerning inspection and remediation.

(c) *Cracking of nickel alloy components of LWR primary systems*
Internal components of reactor vessels are made of nickel-base alloys, e.g., Alloys 600, X750, and 182, which are susceptible to IGSCC. The causes and mechanisms of this cracking are not adequately understood and increase the uncertainty when licensee submissions are evaluated for factors such as damage accumulation and inspection intervals. The objective of this task is to provide technical data on the effects of cracks in nickel–alloy components on residual life, inspection, and repair. The results will be used to support NRR staff assessments of industry crack growth models, and potential detection and mitigation measures.

(d) *Analyses of postwelding heat treatment processes and validation of flaw acceptance criteria*
The objective of this task is to evaluate the effect of postwelding heat treatment on long–term resistance to environmental cracking by assessing sensitization and other microstructural changes. This evaluation will provide NRC with insights for use in reviewing licensee submittals.

(e) *Assess industry crack-growth models*
This task has two objectives. The first is to perform an independent evaluation of industry models that are used to establish inspection intervals and repair criteria. The second objective is to perform more detailed analyses of flaw acceptance criteria.

Research during the past six months has focused on fatigue of carbon steels (CSs) and low–alloy ferritic steels (LASs) and SSs used in piping and pressure vessels, IASCC during slow-strain-rate tensile (SSRT) tests in simulated BWR water of SS specimens that were irradiated to a low fluence in the Halden reactor, and EAC of Alloys 600 in high-purity (HP) oxygenated water.

2 Environmental Effects on Fatigue Strain-versus-Life (S–N) Behavior of Primary Pressure Boundary Materials

Experience with operating nuclear plants worldwide reveals that many failures may be attributed to fatigue. Examples of such failures include: emergency core cooling or residual heat removal systems (USNRC Bulletin No. 88–08), pressurizer surge lines (USNRC Bulletin No. 88–11), PWR feedwater lines (USNRC Information Notice No. 79–13), BWR pressure vessels (USNRC Information Notice No. 90–29), PWR steam generator vessels (USNRC Information Notice No. 90–04), steam generator feedwater distribution piping (USNRC Information Notice No. 91–19 and No. 93–20), and reactor coolant thermal barrier housing (USNRC Information Notice No. 97–31). These failures may be classified into three categories: thermal fatigue caused by thermal stratification, cycling, and striping loadings; mechanical fatigue due to vibratory loading; and corrosion fatigue resulting from the exposure to aqueous environments. Significant thermal loadings due to stratification were not included in the original design basis analysis. Some of these fatigue sensitive locations in nuclear power plants are routinely monitored worldwide to better define the transients and for more accurate assessment of cumulative usage factors (CUF). Occurrences of mechanical–vibration– and thermal–fluctuation–induced fatigue failures in LWR plants in Japan have also been documented.[1]

Cyclic loadings on a structural component occur because of changes in the mechanical and thermal loadings as the system goes from one set of pressure, temperature, moment, and force loading to any other load set. For each pair of load sets, an individual fatigue usage factor is determined by the ratio of the number of cycles anticipated during the lifetime of the component to the allowable cycles. Figures I-9.1 to I-9.6 of Appendix I to Section III of the ASME Boiler and Pressure Vessel Code specifies fatigue design curves that define the allowable number of cycles as a function of applied stress amplitude. The CUF is the sum of the individual usage factors, and the ASME Code Section III requires that the CUF at each location must not exceed 1.

The Code design fatigue curves were based on strain–controlled tests of small polished specimens at room temperature in air. The design fatigue curves were obtained by first adjusting the best–fit curves for the effects of mean stress and then the curves are decreased by a factor of 2 on stress or 20 on cycles, whichever was more conservative, at each point on the best–fit curve. As described in the Section III criteria document, these factors were intended to account for the differences and uncertainties in relating the fatigue lives of laboratory test specimens to those of actual reactor components. Although the factors of 2 and 20 were intended to be somewhat conservative, they should not be considered as safety margins but rather conversion factors that must be applied to the experimental data to obtain reasonable estimates of the lives of actual reactor components. These results raise the issue whether the design fatigue curves in Section III are appropriate for the purposes intended and whether they adequately account for environmental effects on fatigue behavior.

Subsection NB–3121 of Section III of the Code states that the data on which the fatigue design curves (Figs. I–9.1 to I-9.6) are based did not include tests in the presence of corrosive environments that might accelerate fatigue failure. Article B–2131 in Appendix B to Section III states that the owner's design specifications should provide information about any reductions to fatigue design curves that are necessitated by environmental conditions. Recent fatigue S–N data[2–22] demonstrate potentially significant effects of LWR coolant environments on the fatigue resistance of carbon and low–alloy steels, and austenitic SSs, Fig. 1. Under certain conditions of loading and environment, fatigue lives of carbon steels can be a factor of 70 lower in the environment than those in air. Therefore, the margins in the ASME Code may be less conservative than originally intended.

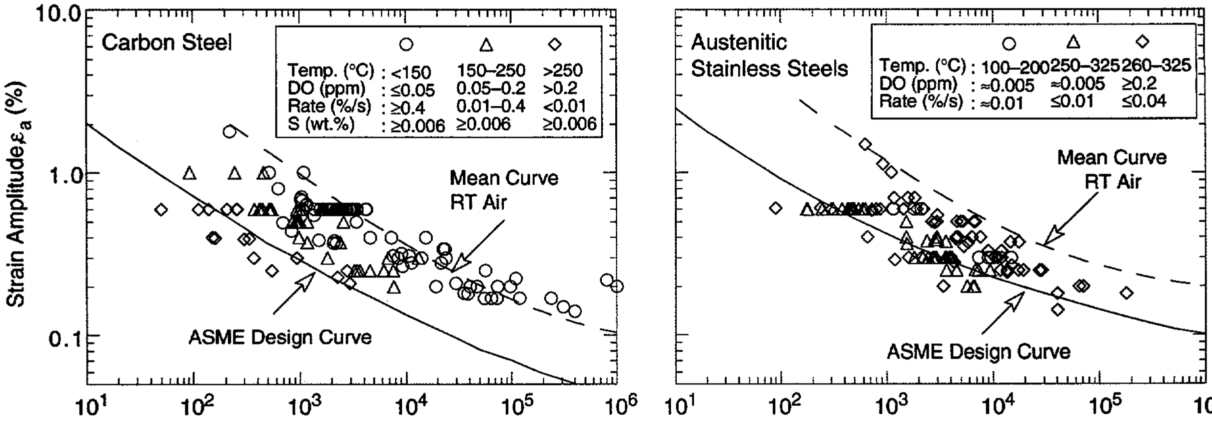

Figure 1. Fatigue S–N data for carbon steels and austenitic stainless steels in water

In 1991, the USNRC issued a draft Branch Technical Position (BTP) for fatigue evaluation of nuclear plant components for license renewal. The BTP raised a concern about the adequacy of the ASME Code in addressing the effects of environment on fatigue resistance of materials in operating PWRs and BWRs, whose primary-coolant pressure–boundary components are constructed as specified in Section III of the Code. Researchers at Argonne National Laboratory (ANL) have compiled and reviewed the existing fatigue S–N data to identify key variables that influence the fatigue lives of primary pressure boundary materials.[16–19] A program was initiated at ANL to obtain fatigue data under conditions that are not addressed in the existing data base. Based on the existing S–N data, researchers at ANL have developed interim design fatigue curves that address the effects of environment on fatigue life of CSs, LASs, and austenitic SSs.[23] Statistical models have also been developed at ANL for estimating the effects of various material and loading conditions on fatigue lives of these materials.[24,25] Results of the statistical analysis have been used to estimate the probability of fatigue cracking in reactor components. The Pressure Vessel Research Council (PVRC) has also been compiling and evaluating fatigue S–N data related to the effects of LWR coolant environments on the fatigue life of pressure boundary materials; the results have been presented by Van Der Sluys and Yukawa.[26]

In 1993, the NRC directed its staff to treat fatigue as a potential safety issue within the existing regulatory process for operating reactors. The staff developed a Fatigue Action Plan (FAP) to resolve three principal issues: (a) the adequacy of fatigue resistance of older vintage plants designed to the United States of America Standard (USAS) B31.1 Code that did not require an explicit fatigue analysis of components, (b) the effect of LWR environments on the fatigue resistance of primary pressure boundary materials, and (c) the appropriate corrective action required when the Code fatigue allowable limits have been exceeded, i.e., when the CUF is >1. The Idaho National Engineering Laboratory assessed the significance of the interim fatigue design curves by performing fatigue evaluations of several components in the reactor coolant pressure boundary.[27] In all, six locations were evaluated from facilities designed by each of the four U.S. nuclear steam supply system vendors. Selected components from older vintage plants designed to comply to B31.1 Code were also included in the evaluation. An assessment of risk to reactor coolant pressure boundary components from failure due to fatigue was performed under Generic Safety Issue (GSI) 78, "Monitoring of Fatigue Transient Limits for the Reactor Coolant System." On the basis of these studies, it was concluded* that no immediate action is necessary to deal with fatigue issues addressed in the FAP. The risk study indicated that a fatigue failure of piping is not a significant contributor to core–melt frequency. Although fatigue cracks may occur, they may not propagate to failure and, even if failure did occur, safety systems, such as the emergency core cooling system (ECCS), mitigate the consequences. On the basis of the risk assessment, a backfit of the environmental fatigue data to operating plants cannot be justified.

The objective of this task is to provide data and models for predicting the effects of environment on fatigue design curves and to assess the additivity of fatigue damage in piping and vessel steels under load histories typical of LWR components. The data will be used by the NRC staff to assess industry fatigue evaluations related to license renewal. The information, which will be helpful in assessing applicant submissions with regard to residual lifetimes of components subjected to fatigue in reactor coolant environments, and will be

---

*Policy Issue, SECY–95–245, Completion of the Fatigue Action Plan, Sept. 25, 1995.

provided to the ASME to help improve the design curves. Fatigue tests are being conducted to establish the effects of various loading and environmental variables on the fatigue S–N behavior of pressure boundary steels. The experimental effort is currently focused on the effects of dissolved oxygen (DO) and strain rate on the fatigue lives of wrought and cast austenitic SSs and to establish the threshold strain range below which environmental effects on fatigue life either do not occur or are insignificant. A topical report has been prepared that summarizes work performed by ANL on fatigue of carbon and low–alloy steels in LWR environments.

2.1 Carbon and Low–Alloy Steels (O. K. Chopra and W. J. Shack)

2.1.1 Overview of Fatigue S–N Data

The primary sources of relevant S–N data for CSs and LASs are the tests performed by General Electric Co. (GE) in a test loop at the Dresden 1 reactor[2,3] and by the Electric Power Research Institute;[4,5] the work at Mechanical Engineering Associates (MEA);[6,7] the present work at ANL on fatigue of pressure vessel and piping steels;[16–18] the JNUFAD* data base for "Fatigue Strength of Nuclear Plant Component;" and recent studies at IHI, Hitachi, and Mitsubishi Heavy Industries in Japan.[8–12] The data base is composed of ≈1200 tests, ≈600 each in air and water environments. Carbon steels include ≈10 heats of A333–Grade 6, A106–Grade B, A516–Grade 70, and A508–Class 1 steel, and the LASs include ≈15 heats of A533–Grade B, A302–Gr B, and A508–Class 2 and 3 steels.

The existing fatigue S–N data for CSs and LASs have been evaluated to establish the effects of various material and loading variables such as steel type, strain range, strain rate, temperature, sulfur content in steel, orientation, and DO level in water on the fatigue life of these steels. The significant results are summarized below.

Air Environment

In air, the fatigue lives of CSs and LASs depend on steel type, temperature, orientation (rolling or transverse), and strain rate. The fatigue lives of CSs are a factor of ≈1.5 lower than that of LASs. For both steels, life decreases by a factor of ≈1.5 when temperature increases from room temperature to 288°C. In the temperature range of dynamic strain aging (200–370°C), some heats of CSs and LASs are sensitive to strain rate. The effect of strain rate on fatigue life is not clear; life may either be unaffected, decrease for some heats, or increase for others. In this temperature range, however, cyclic stresses increase with decreasing strain rate. Also, based on the distribution and morphology of sulfides, the fatigue properties in the transverse orientation may be inferior to those in the rolling orientation.

The data indicate significant heat–to–heat variation; at 288°C, fatigue life may vary up to a factor of 5 above or below the mean value. The results also indicate that the ASME mean curve for LASs is in good agreement with the experimental data, and for CSs, the curve is somewhat conservative. At strain amplitudes <0.2%, the mean curve for CSs predicts significantly lower fatigue lives than those observed experimentally.

---

*Private communication from M. Higuchi, Ishikawajima–Harima Heavy Industries Co., Japan, to M. Prager of the Pressure Vessel Research Council, 1992. The old data base "FADAL" has been revised and renamed "JNUFAD."

LWR Environments

The fatigue lives of both CSs and LASs decrease significantly when five conditions are satisfied simultaneously, viz., applied strain amplitude, service temperature, DO level in the water, and sulfur content of the steel are above a minimum threshold level, and the loading strain rate is below a threshold value. Although the microstructures and cyclic–hardening behavior of CSs and LASs are significantly different, environmental degradation of fatigue life of these steels is identical. For both steels, only a moderate decrease in life (by a factor of less than 2) is observed when any one of these conditions is not satisfied. The effects of various material and loading parameters on fatigue life and the threshold values of the critical parameters are summarized below.

(a) *Strain Amplitude*: A minimum threshold strain is required for environmentally assisted decrease in fatigue life of these steels.[16–18] This behavior is consistent with the slip oxidation/dissolution mechanism[28,29] for enhancement of crack growth rates; threshold strain most likely corresponds to the rupture strain of the surface oxide film. Limited data suggest that the threshold value is ≈20% higher than the fatigue limit for the steel.[18]

(b) *Strain Rate*: When any one of the threshold conditions is not satisfied, e.g., DO <0.05 ppm or temperature <150°C, the effects of strain rate are consistent with those in air, i.e., heats that are sensitive to strain rate in air also show a decrease in life in water. When all of the other threshold conditions are satisfied, Fig. 2, fatigue life decreases logarithmically with decreasing strain rate below 1%/s; the effect of environment on life saturates at ≈0.001%/s.[8–12,16–18]

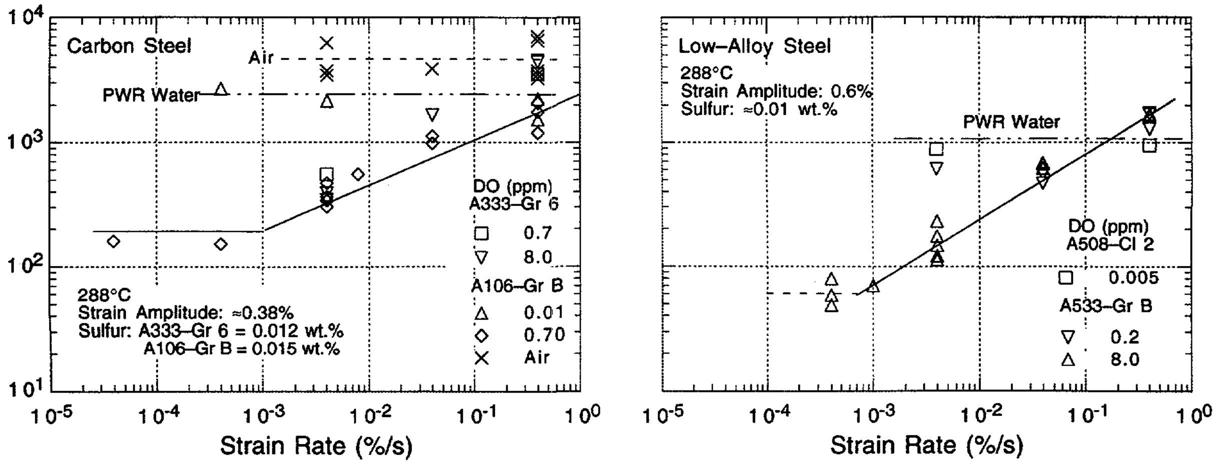

Figure 2. Dependence of fatigue life of carbon and low–alloy steels on strain rate

(c) *Loading Cycle*: Environmental effects on fatigue life occur primarily during the tensile–loading cycle, and at strain levels greater than the threshold value required to rupture the surface oxide film. The compressive–loading cycle has little or no effect on life. Results from exploratory tests,[10,16–18] in which the slow strain rate is applied during only a fraction of the tensile loading cycle, are shown in Fig. 3; variation in fatigue life is plotted as a function of the fraction of loading strain at slow strain rate. Open symbols indicate tests where the slow portions occurred near the maximum tensile strain. Closed symbols indicate tests in which the slow portions occurred near the maximum compressive strain.

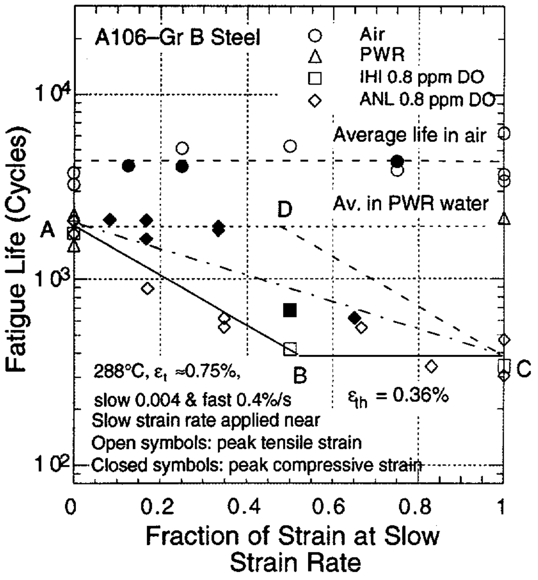

Figure 3.
Fatigue lives of carbon and low–alloy steels tested with loading waveforms in which slow strain rate is applied during a fraction of tensile loading cycle

In Fig. 3, if the relative damage were totally independent of strain amplitude, fatigue life should decrease linearly from A to C along the chain–dot line. Instead, the results indicate that the relative damage due to slow strain rate is independent of strain amplitude once the amplitude exceeds a threshold value to rupture the passive surface film. Consequently, loading and environmental conditions, e.g., strain rate, temperature, and DO level, during the tensile–loading cycle in excess of the oxide rupture strain, are important parameters for environmentally assisted reduction in fatigue life of these steels.

(d) *Temperature*: When other threshold conditions are satisfied, fatigue life decreases linearly with temperature above 150°C and up to 320°C (Fig. 4).[8,9,12] Fatigue life is insensitive to temperature below 150°C or when any other threshold condition is not satisfied. Estimates of fatigue life from a trained Artificial Neural Network (ANN) also show a similar effect of temperature on the fatigue life of CSs and LASs.[30] Furthermore, experimental data from tests, in which both strain and temperature were varied during each cycle[11] indicate a threshold temperature of 150°C below which environmental effects on life either do not occur or are insignificant. For service histories involving variable loading and environmental conditions, service temperature may be represented by the average of 150°C and the maximum temperature.

(e) *Dissolved Oxygen in Water*: When other threshold conditions are satisfied, fatigue life decreases logarithmically with DO above 0.05 ppm; the effect saturates at ≈0.5 ppm DO, Fig. 5.[8,12] Estimates of fatigue life from a trained ANN also show a similar dependence of life on DO level.[30]

(f) *Sulfur Content in Steel*: Although sulfur content and morphology are the most important parameters that determine susceptibility of CSs and LASs to environmentally enhanced fatigue crack growth rates,[31–38] the existing fatigue S–N data are inadequate to establish unequivocally the effect of sulfur content on the fatigue life of these steels. When any one of the threshold conditions is not satisfied, environmental effects on life are minimal and relatively insensitive to changes in sulfur content. When the threshold conditions are satisfied, i.e., in high–temperature high–DO water, the fatigue lives of LASs decrease with

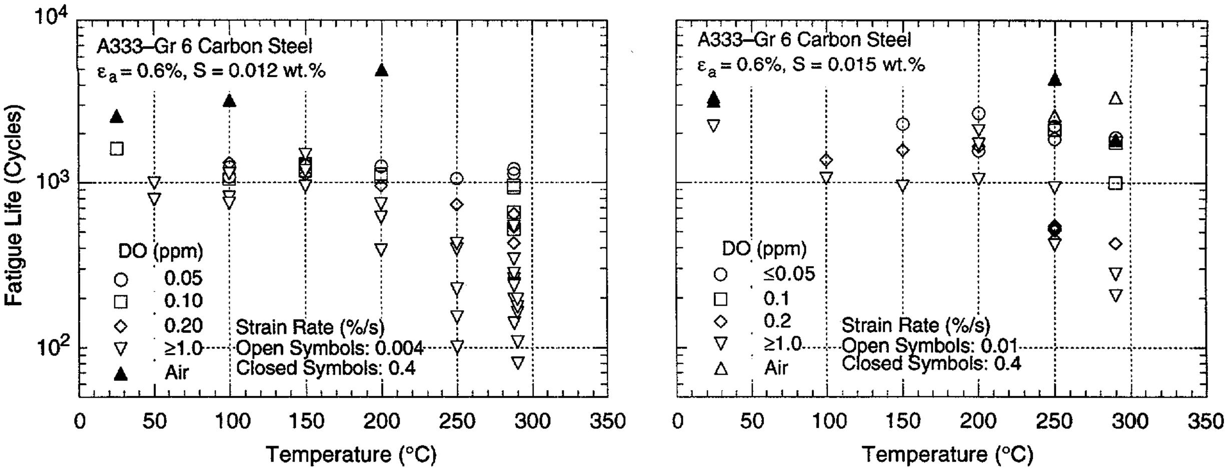

Figure 4. Change in fatigue life of A333–Gr 6 carbon steel with temperature and DO

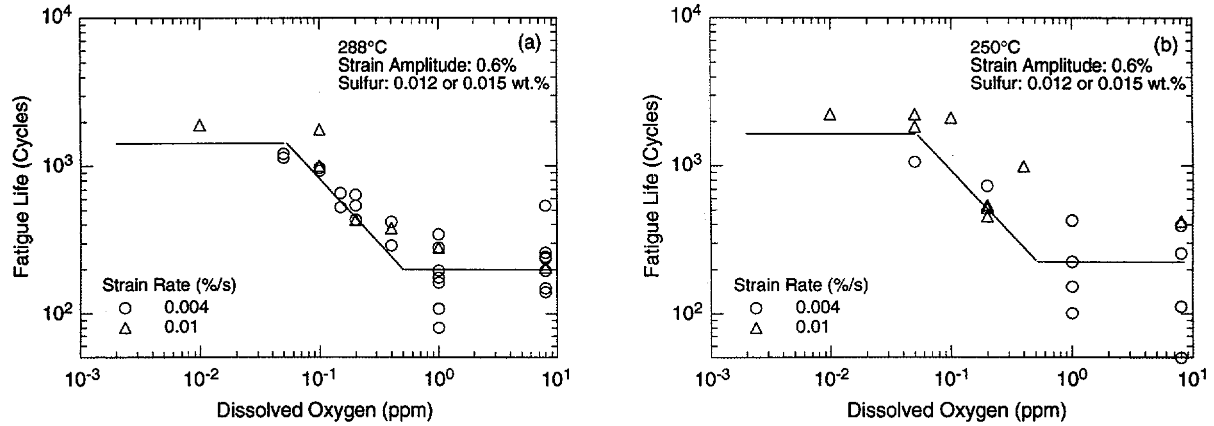

Figure 5. Dependence on DO of fatigue life of carbon steel

increasing sulfur content.[8,9] Limited data suggest that the effects of environment on life saturate at sulfur contents above 0.012 wt.%.[39] However, in high–temperature high–DO water, the fatigue lives of CSs seem to be insensitive to sulfur content in the range of 0.002–0.015 wt.%.* The variation in fatigue life of CSs and LASs with different sulfur content is plotted as a function of strain rate in Fig. 6. For LASs, environmental effects on fatigue life increase as sulfur content increases, whereas fatigue lives of CSs seem to be independent of sulfur content in the range of 0.002–0.015 wt.%. The effect of sulfur on the growth of short cracks (during crack initiation) may be different than for long cracks, and this needs to be further investigated.

(g) *Orientation*: Orientation is expected to affect fatigue life because of differences in the distribution and morphology of sulfide inclusions, and is well known in crack growth studies with precracked specimens.[34–37] Existing fatigue S–N data indicate that in high–DO water (≥0.1 ppm DO), the fatigue lives of LASs are insensitive to the differences in sulfide distribution and size.[39] Sulfide morphology may influence fatigue life in low–DO

---

*M. Higuchi, presented at the Pressure Vessel Research Council Meeting, June 1995, Milwaukee, WI.

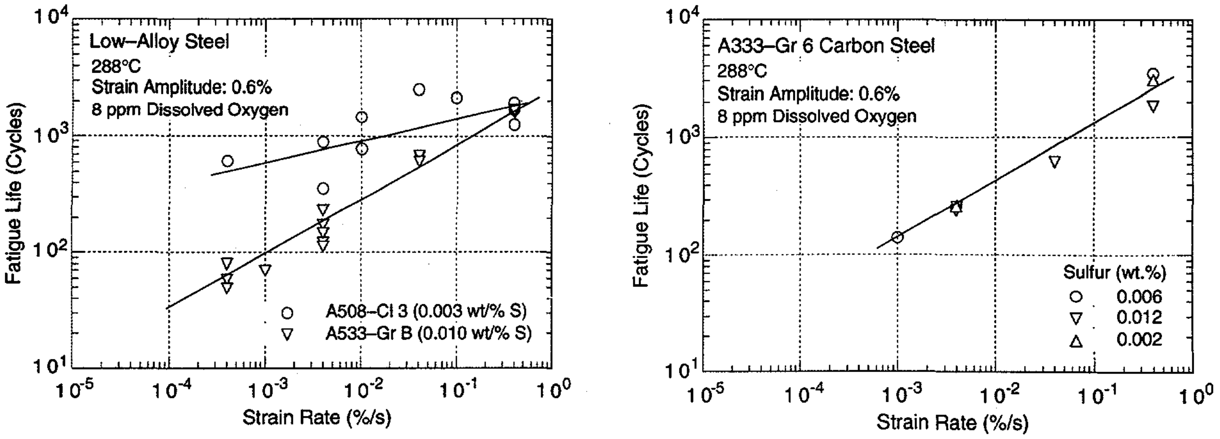

Figure 6. Effect of strain rate on fatigue life of carbon and low–alloy steels with different sulfur contents

PWR environments, but the difference would be insignificant because environmental effects on life are minimal in low–DO environments.

(h) *Flow Rate*: Studies of fatigue crack growth behavior of CSs and LASs indicate that flow rate influences the rate of crack growth.[31,36,40,41] Corrosion fatigue growth rates are controlled by the synergistic effects of sulfur content, environmental conditions, and flow rate.[36] However, experimental data to establish either the dependence of fatigue life on flow rate or the threshold flow rate for environmental effects to occur are not available and should be developed.

2.1.2 Mechanism of Fatigue Crack Initiation

Deformation and microstructural changes in surface grains control initiation of fatigue cracks. During cyclic straining, microcracks form within persistent slip bands (PSBs); at the edges of slip–band extrusions; in notches that develop at grain, twin, or phase boundaries (e.g., ferrite/pearlite); or by cracking of second–phase particles (e.g., sulfide or oxide inclusions). Once a microcrack forms, it continues to grow along its slip plane or a PSB as a Mode II (shear) crack in Stage I growth (the orientation of the crack is usually 45° to the stress axis). At low strain amplitudes, a Stage I crack may extend across several grain diameters before the increasing stress intensity of the crack promotes slip on systems other than the primary slip. Because slip is no longer confined to planes at 45° to the stress axis, the crack begins to propagate as a Mode I (tensile) crack, normal to the stress axis in Stage II growth. At high strain amplitudes, the stress intensity is quite large and the crack propagates entirely by the Stage II process. Stage II crack propagation continues until the crack reaches an engineering size (≈3 mm deep). In air or mildly corrosive environments, Stage II cracking is characterized by fatigue striations.

The formation of surface cracks and their growth as shear and tensile cracks (Stage I and II growth) to an "engineering" size (e.g., a 3-mm–deep crack) constitute the fatigue life of a material, which is represented by the fatigue S–N curves. The curves specify, for a given stress or strain amplitude, the number of cycles needed to form an engineering crack. Fatigue life, has conventionally been represented by two stages: (a) initiation, which represents the cycles N_i for formation of microcracks on the surface; and (b) propagation, which represents cycles

N_p for propagation of the surface cracks to an engineering size. Thus, fatigue life N is the sum of the two stages, $N = N_i + N_p$. The former is considered to be sensitive to the stress or strain amplitude, e.g., at low strain amplitudes, most of the life may be spent in initiating a crack, whereas at high strain amplitudes, cracks initiate easily.

Reduction of fatigue life in high–temperature water has been attributed to the presence of micropits, which form in both CSs and LASs due to dissolution of MnS inclusions or by corrosion reactions, that act as stress raisers and provide preferred sites for the formation of fatigue cracks.[8] The strain rate effects in water have been explained on the basis of a higher density of micropits at lower strain rates, i.e., longer test durations in slow strain rate tests produce a higher density of micropits, and hence a shorter period for formation of surface microcracks.

If micropits are responsible for a reduction in fatigue life of CSs and LASs in LWR environments, then the following behavior should be observed: (a) specimens tested in high–DO water should show more surface cracks and (b) specimens preexposed to high–DO water and then tested in air should also show a decrease in life. Experimental data indicate the contrary. The frequency of cracks (i.e., number of cracks per unit gauge length) in CS and LAS specimens tested in air and high–DO water is identical, although fatigue life is lower by more than a factor of 8 in water.[42] Also, the fatigue lives of A106–Gr B CS and A533–Gr B LAS specimens preoxidized at 288°C in high–DO water (≈0.7 ppm DO) and then tested either in air or low–DO water (<0.01 ppm DO) are identical to those of nonoxidized specimens (Fig. 7).[16–18] A decrease in life would be expected if surface micropits facilitate the formation of fatigue cracks. Furthermore, if micropits were responsible for the decrease in fatigue life in LWR environments, then the fatigue limit of these steels should be lower in water than in air. Data in high–DO water indicate that the fatigue limit in water is either the same or ≈20% higher than in air. Irrespective of environment, cracks in CSs and LASs form along slip bands, carbide particles, or at ferrite/pearlite phase boundaries.[20,42]

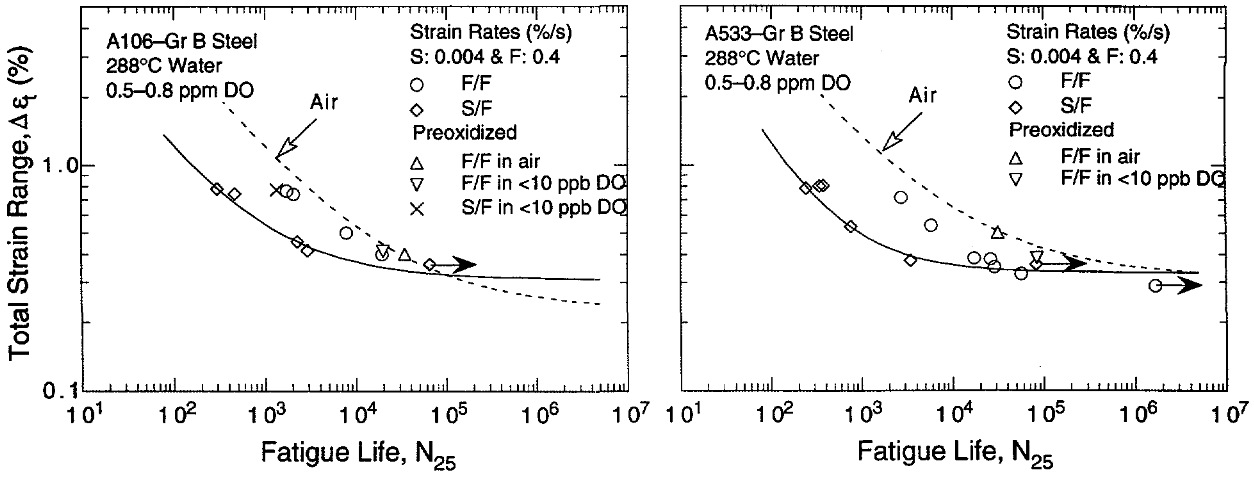

Figure 7. Environmental effects on formation of fatigue cracks in carbon and low–alloy steels. Preoxidized specimens were exposed at 288°C for 30–100 h in water with ≈0.7 ppm DO.

Recent studies indicate that the fatigue life of engineering structures and components is composed entirely of the growth of short fatigue cracks.[43] For polycrystalline materials, the period for formation of surface cracks is negligible; surface cracks, 10 μm or longer, form quite early in life,[20,44–46] i.e., <10% of life even at low strain amplitudes (Fig. 8). Fatigue damage in a material is the current size of the fatigue crack and damage accumulation is the rate of crack growth. Growth of short fatigue cracks may be divided into three regimes shown in Fig. 9a: (a) an initial period that involves growth of microstructurally small cracks (MSCs) that is very sensitive to microstructure and is characterized by a decelerating growth rate, region AB; (b) a final period of growth that can be predicted from fracture mechanics methodology and is characterized by an accelerating crack growth rate, region CD; and (c) a transition period controlled by a combination of the two regimes, region BC.

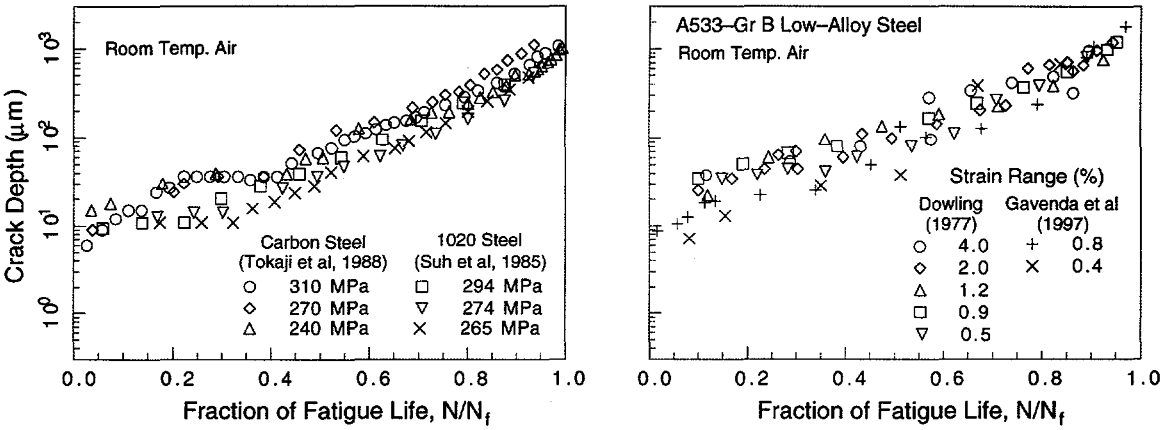

Figure 8. Crack depth as a function of fractional life for carbon and low–alloy steels tested in room–temperature air

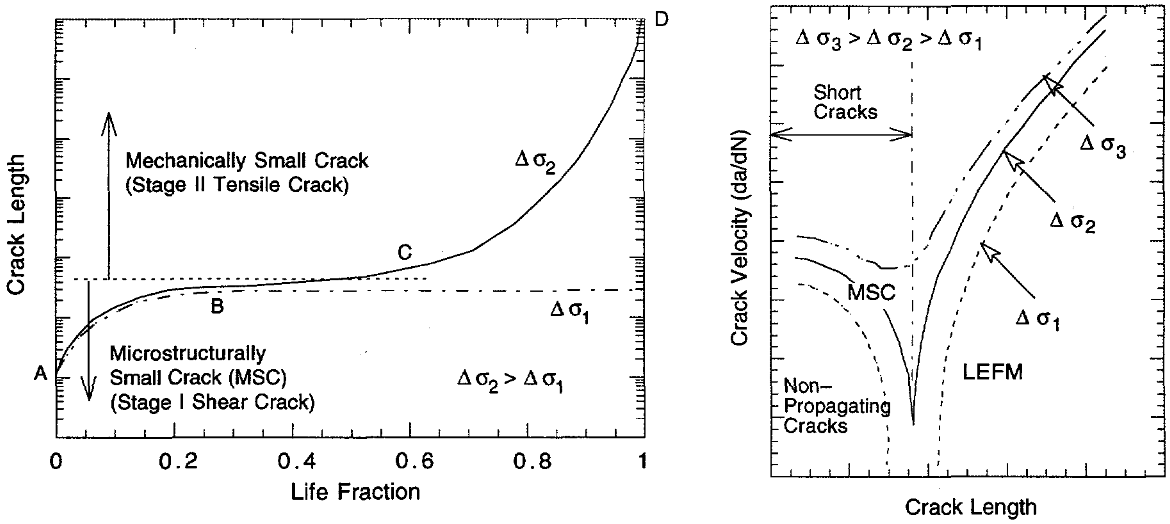

(a) (b)

Figure 9. Schematic illustration of short crack behavior in smooth fatigue specimens: (a) crack growth as a function of life fraction and (b) crack velocity as a function of crack length

The MSCs correspond to Stage I cracks and grow along slip planes as shear cracks; their growth is very sensitive to microstructure.[46–52] The growth rates decrease markedly because of grain boundaries, triple points, and ferrite/pearlite phase boundaries. In ferritic–pearlitic steels, fatigue cracks initiate and propagate preferentially in the ferrite phase that forms as long allotriomorphs at prior austenite phase boundaries.[46,51,52] Fatigue cracks greater than the critical length of MSCs show little or no influence of microstructure and are termed mechanically small cracks.[48,49] For a stress ratio of –1, the transition from MSC to a mechanically small crack for several materials has been estimated to be ≈8 times the unit size of the microstructure.[49] Mechanically small cracks correspond to Stage II, or tensile, cracks characterized by striated crack growth, with a fracture surface normal to the maximum principal stress. For ferritic–pearlitic steels, Stage II crack propagation occurs when the stress intensity and mode of growth attain a critical level and break through the pearlite and join other ferrite cracks.[51] At low stress levels, e.g., $\Delta\sigma_1$ in Fig. 9, the transition from MSC growth to accelerating crack growth does not occur and the cracks are nonpropagating. This circumstance represents the fatigue limit for the smooth specimen. Although cracks can form below the fatigue limit, they can grow to engineering size only at stresses greater than the fatigue limit.

Studies on the formation and growth characteristics of short cracks in smooth fatigue specimens in LWR environments indicate that the decrease in fatigue life of CSs and LASs in high–DO water is primarily caused by the effects of environment on the growth of cracks <100 μm deep.[20] In high–temperature high–DO water, the period for region ABC in Fig. 9a is decreased, or crack velocities for MSC regime in Fig. 9b are increased. Relative to air, crack growth rates in high–DO water are nearly two orders of magnitude higher during the initial stages of crack growth (for crack sizes <100 μm), and are one order of magnitude higher for crack sizes >100 μm (Fig. 10).

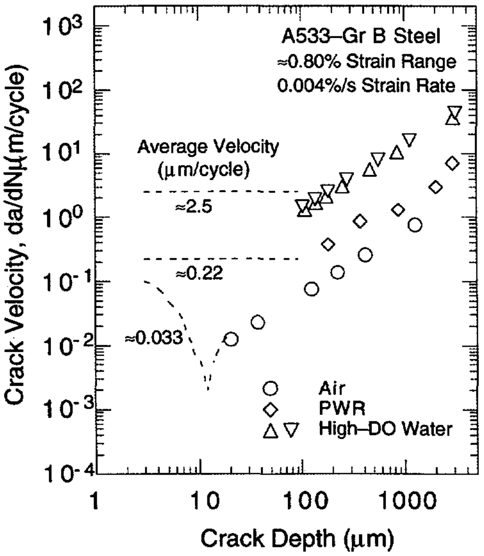

Figure 10.
Crack growth rates plotted as a function of crack depth for A533–Gr B low–alloy steel tested in air and water environments

In high–DO water, surface cracks grow entirely as tensile cracks normal to the stress (Fig. 11).[20] In air and low–DO water, growth of surface cracks occurs initially as shear cracks ≈45° to the stress axis, and then as tensile cracks normal to the stress axis when slip is no longer confined to planes at 45° to the stress axis. Also, for CSs, Stage I crack growth in air and low–DO water occur entirely along the soft ferrite grains, whereas in high–DO water

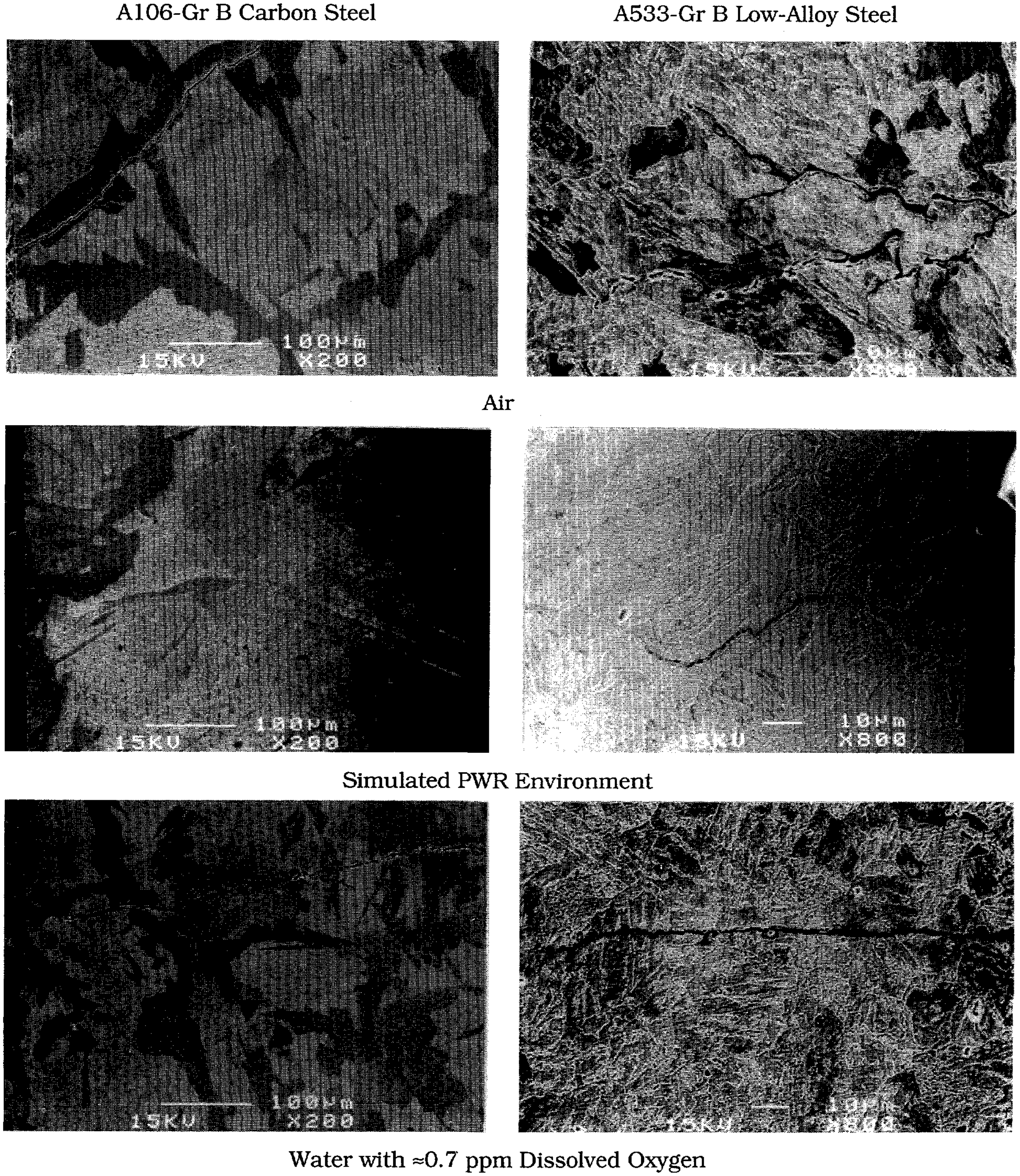
A106-Gr B Carbon Steel

A533-Gr B Low-Alloy Steel

Air

Simulated PWR Environment

Water with ≈0.7 ppm Dissolved Oxygen

Figure 11. Photomicrographs of surface cracks along longitudinal sections of A533–Gr B and A106–Gr B steels in air, simulated PWR environment, and high–DO water

the cracks propagate across both ferrite and pearlite regions. Fracture surfaces of specimens tested in water exhibit a typical ductile fatigue fracture; an example of a typical fracture morphology is shown in Fig. 12. Faint fatigue striations are also observed on some specimens at crack depths greater than ≈0.8 mm. However, the striations seem to be produced by rupture of the surface oxide film rather than by the formation of double notches or "ears" at

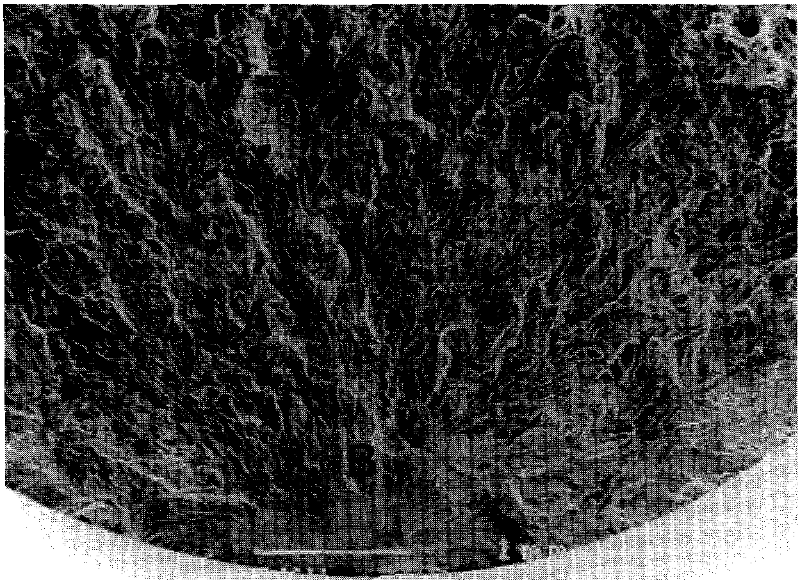

Region A

Region B

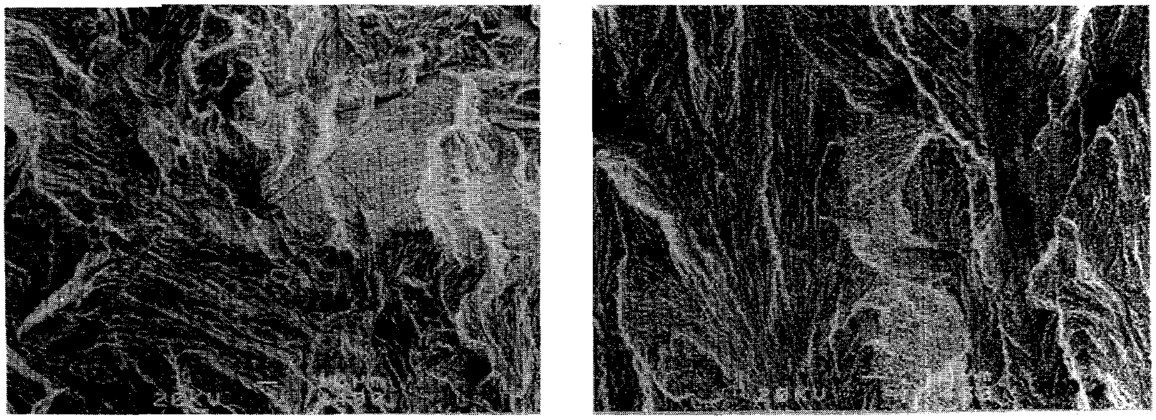

Before Chemical Cleaning

Before Chemical Cleaning

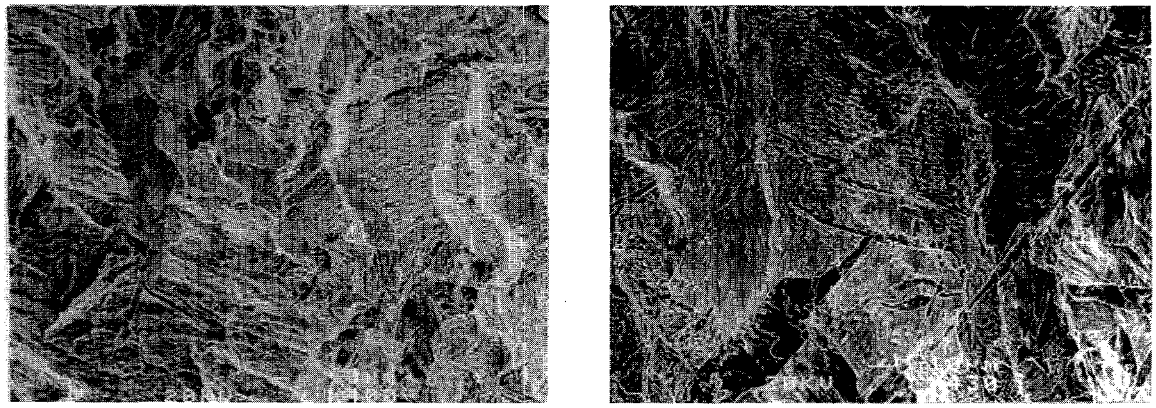

After Chemical Cleaning

After Chemical Cleaning

Figure 12. Fracture morphology of A106–Gr B carbon steel tested in high–DO water at 288°C and ≈0.4% strain range

the crack tip; striations are not observed after the specimens are descaled. Fracture morphologies indicative of hydrogen–induced cracking, e.g., quasi–cleavage facets or fanlike features extending from sulfide inclusions or a terraced morphology produced by linkage of hydrogen–induced cracks at a sulfide/matrix interface ahead of the main crack,[36,53–55] are not observed in CS or LAS specimens tested in LWR environments.

The absence of quasi–cleavage facets and Stage I crack growth, and the propagation of cracks across pearlite regions suggest that factors other than mechanical fatigue are important for growth of short surface cracks in high–DO water. These results are consistent with the slip oxidation/dissolution mechanism of crack growth, i.e., growth of MSCs occurs by slip dissolution/oxidation. In LWR environments, formation of engineering cracks may be explained as follows: (a) surface microcracks form quite early in fatigue life at PSBs, edges of slip–band extrusions, notches that develop at grain or phase boundaries, or second–phase particles; (b) during cyclic loading, the protective oxide film ruptures at strains greater than the fracture strain of surface oxides, and the microcracks or MSCs grow by anodic dissolution of the freshly exposed surface to sizes greater than the critical length of MSCs; and (c) growth of these large cracks is characterized by accelerating growth rates. Growth rates during the final stage are controlled by both environmental and mechanical factors and may be represented by the proposed ASME Section XI reference curves for CSs and LASs in water environments.[56] Growth rates during the initial stage are controlled primarily by the environment, but mechanical fatigue is required for film rupture.

2.1.3 Statistical Model

The fatigue S–N curves are generally expressed in terms of the Langer equation, which may be used to represent either strain amplitude in terms of life or life in terms of strain amplitude. The parameters of the equation are commonly established through least–squares curve–fitting of the data to minimize the sum of the square of the residual errors for either strain amplitude or fatigue life. A predictive model based on a least–squares fit on life is biased for low strain amplitude. The model leads to probability curves that converge to a single value of strain, and it fails to address the fact that at low strain values, most of the error in life is due to uncertainty associated with either measurement of strain or variation in fatigue limit caused by material variability. On the other hand, a least–squares fit on strain does not work well for higher strain amplitudes.

In the present study, statistical models have been developed by combining the two approaches to minimize the sum of the squared Cartesian distances from the data point to the predicted curve (Fig. 13). For low ε_a, this is very close to optimizing the sum of squared errors in predicted ε_a; at high ε_a, it is very close to optimizing the sum of squared errors in predicted life; and at medium ε_a, the model combines both factors. However, because the model includes many nonlinear transformations of variables and because different variables affect different parts of the data, the actual functional form and transformations are partly responsible for minimizing the squares of the errors. The functional forms and transformations were based on experimental observations and data trends.

Based on the existing fatigue S–N data base, statistical models have been developed for estimating the effects of material and loading conditions on the fatigue lives of CSs and LASs.[24,25] The models have been further optimized with a larger fatigue S–N data base. Because of the conflicting possibilities that with decreasing strain rate, fatigue life may either

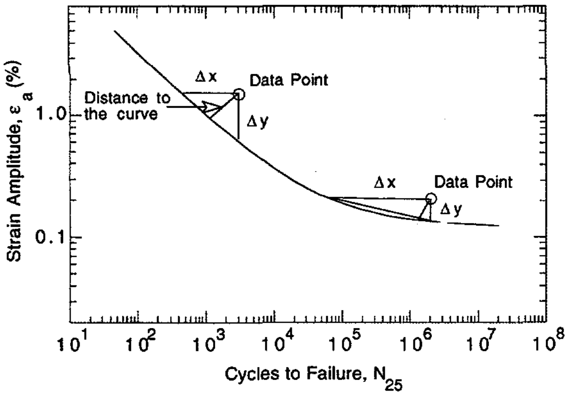

Figure 13.
Schematic of least-squares curve-fitting of data by minimizing sum of squared Cartesian distances from data points to predicted curve

be unaffected, decrease for some heats, or increase for others, effects of strain rate in air were not explicitly considered in the model. The effects of orientation, i.e., size and distribution of sulfide inclusions, on fatigue life were also excluded because the existing data base does not include information on sulfide distribution and morphology. In air, the fatigue data for CSs are best represented by

$$\ln(N_{25}) = 6.595 - 1.975 \ln(\varepsilon_a - 0.113) - 0.00124\, T \qquad (1a)$$

and for LASs by

$$\ln(N_{25}) = 6.658 - 1.808 \ln(\varepsilon_a - 0.151) - 0.00124\, T, \qquad (1b)$$

where N_{25} is fatigue life of a smooth test specimen defined as number of cycles for the tensile stress to drop 25% from its peak value (which corresponds to a crack depth of ≈3 mm), ε_a is applied strain amplitude (%), and T is test temperature (°C). In LWR environments, the fatigue data for CSs are best represented by

$$\ln(N_{25}) = 6.010 - 1.975 \ln(\varepsilon_a - 0.113) + 0.101\, S^*\, T^*\, O^*\, \dot{\varepsilon}^* \qquad (2a)$$

and for LASs by

$$\ln(N_{25}) = 5.729 - 1.808 \ln(\varepsilon_a - 0.151) + 0.101\, S^*\, T^*\, O^*\, \dot{\varepsilon}^*, \qquad (2b)$$

where S^*, T^*, O^*, and $\dot{\varepsilon}^*$ = transformed sulfur content, temperature, DO, and strain rate, respectively, defined as follows:

$S^* = S$ $(0 < S \le 0.015$ wt.%)
$S^* = 0.015$ $(S > 0.015$ wt.%) (3a)

$T^* = 0$ $(T < 150°C)$
$T^* = T - 150$ $(T = 150–350°C)$ (3b)

$O^* = 0$ (DO <0.05 ppm)
$O^* = \ln(DO/0.04)$ (0.05 ppm ≤DO ≤0.5 ppm)
$O^* = \ln(12.5)$ (DO >0.5 ppm) (3c)

$\dot{\varepsilon}^* = 0$ $(\dot{\varepsilon} > 1$ %/s)
$\dot{\varepsilon}^* = \ln(\dot{\varepsilon})$ $(0.001 \le \dot{\varepsilon} \le 1$ %/s)
$\dot{\varepsilon}^* = \ln(0.001)$ $(\dot{\varepsilon} < 0.001$ %/s) (3d)

The model is recommended for predicted fatigue lives $\leq 10^6$ cycles. For fatigue lives of 10^6 to 10^8 cycles, the results should be used with caution because in this range, the model is based on very limited data from relatively few heats of material.

2.1.4 Fatigue Life Correction Factor

An alternative approach for incorporating the effects of reactor coolant environments on fatigue S–N curves has been proposed by the Environmental Fatigue Data (EFD) Committee of Thermal and Nuclear Power Engineering Society (TENPES) of Japan.* The effects of coolant environment on fatigue life are expressed in terms of a fatigue life correction factor F_{en}, which is the ratio of the life in air at room temperature to that in water at the service temperature. To incorporate environmental effects into the ASME Code fatigue evaluation, a fatigue usage for a specific load pair based on the current Code fatigue design curve is multiplied by the correction factor. The specific expression for F_{en}, proposed initially by Higuchi and Iida,[9] assumes that life in the environment N_{water} is related to life in air N_{air} at room temperature through a power–law dependence on the strain rate

$$F_{en} = \frac{N_{air}}{N_{water}} = (\dot{\varepsilon})^{-P} \tag{4a}$$

or

$$\ln(F_{en}) = \ln(N_{air}) - \ln(N_{water}) = -P\ln(\dot{\varepsilon}). \tag{4b}$$

In air at room temperature, the fatigue life N_{air} of CSs is expressed as

$$\ln(N_{air}) = 6.653 - 2.119\ \ln(\varepsilon_a - 0.108) \tag{5a}$$

and for LASs by

$$\ln(N_{air}) = 6.578 - 1.761\ \ln(\varepsilon_a - 0.140), \tag{5b}$$

where ε_a is the applied strain amplitude (%). Only the tensile loading cycle is considered to be important for environmental effects on fatigue life. The exponent P is a product of a environmental factor R_p, which depends on temperature T (°C) and DO level (ppm), and a material factor P_c, which depends on the ultimate tensile strength σ_u (MPa) and sulfur content S (wt.%) of the steel. Thus

$$P = R_p\ P_c, \tag{6a}$$

$$P_c = 0.864 - 0.00092\ \sigma_u + 14.6\ S, \tag{6b}$$

$$R_p = \frac{R_{pT} - 0.2}{2.64}\ln(DO) + 1.75R_{pT} - 0.035, \qquad 0.2 \leq R_p \leq R_{pT} \tag{6c}$$

and

$$R_{pT} = 0.198\ \exp(0.00557T). \tag{6d}$$

---

*Presented at the Pressure Vessel Research Council Meeting, April 1996, Orlando, FL.

The fatigue lives of CSs and LASs measured experimentally and those estimated from the statistical and EFD models are shown in Figs. 14–18. Although the EFD correlations for exponent P have been based entirely on data for CSs, Eqs. 6a–6d were also used for estimating the fatigue lives of LASs. Also, σ_u in Eq. 6b was assumed to be 520 and 650 MPa, respectively, for CSs and LASs. The significant differences between the two models are:

(a) The EFD correlations have been developed from data for CSs alone.

(b) The statistical model considers that the effects of strain rate on fatigue life saturate below 0.001%/s (Fig. 17). Such a saturation is not considered in the EFD model.

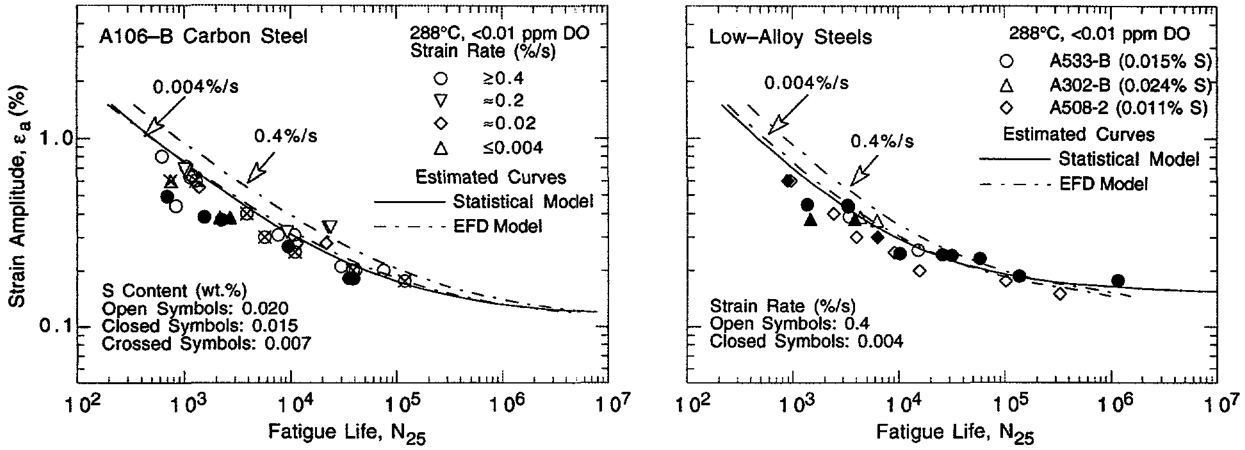

Figure 14. Experimental fatigue lives and those estimated from the statistical and EFD models for carbon and low–alloy steels in simulated PWR water

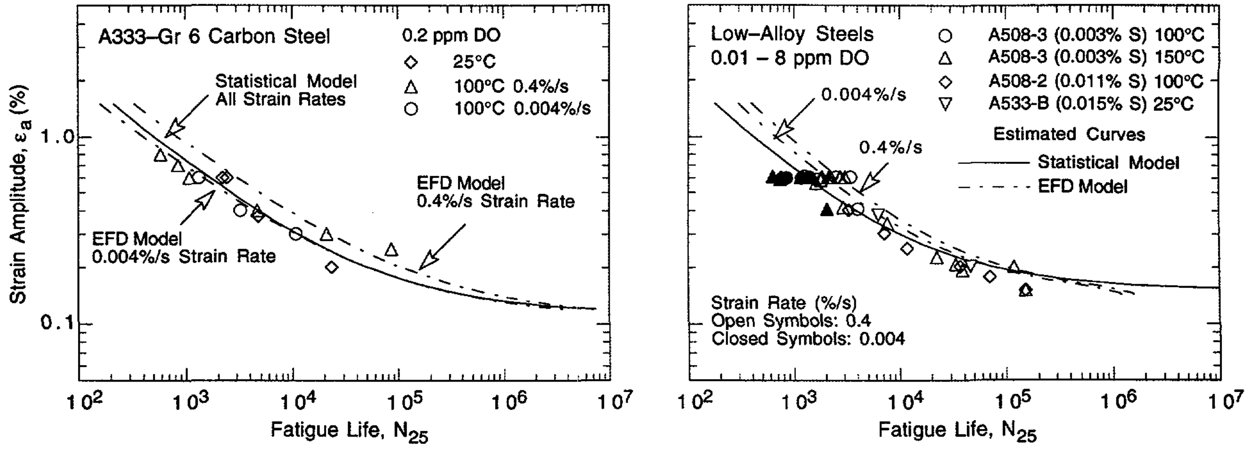

Figure 15. Experimental fatigue lives and those estimated from the statistical and EFD models for carbon and low–alloy steels in water at temperatures below 150°C

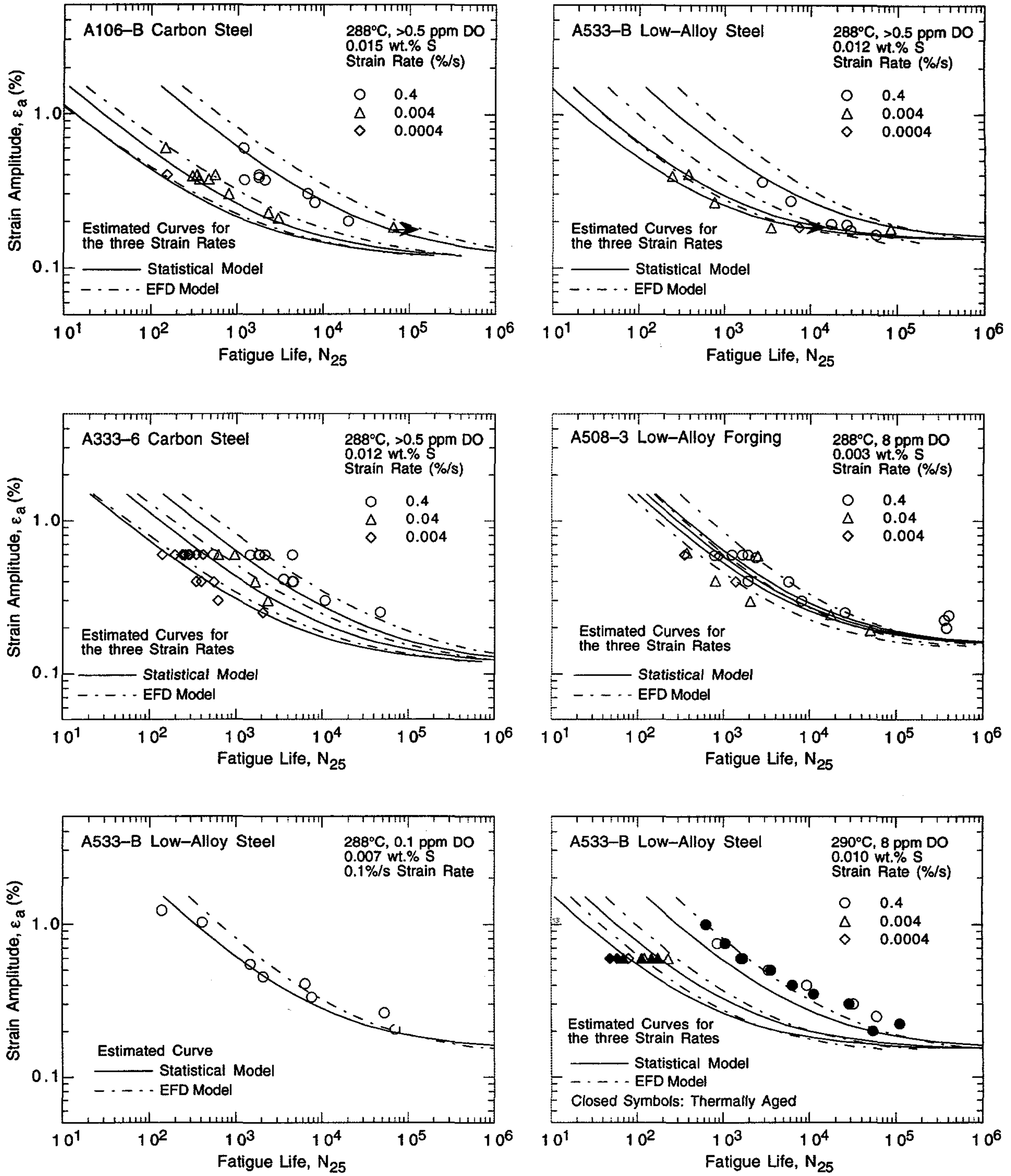

Figure 16. Experimental fatigue lives and those estimated from the statistical and EFD models for carbon and low–alloy steels in high–DO water

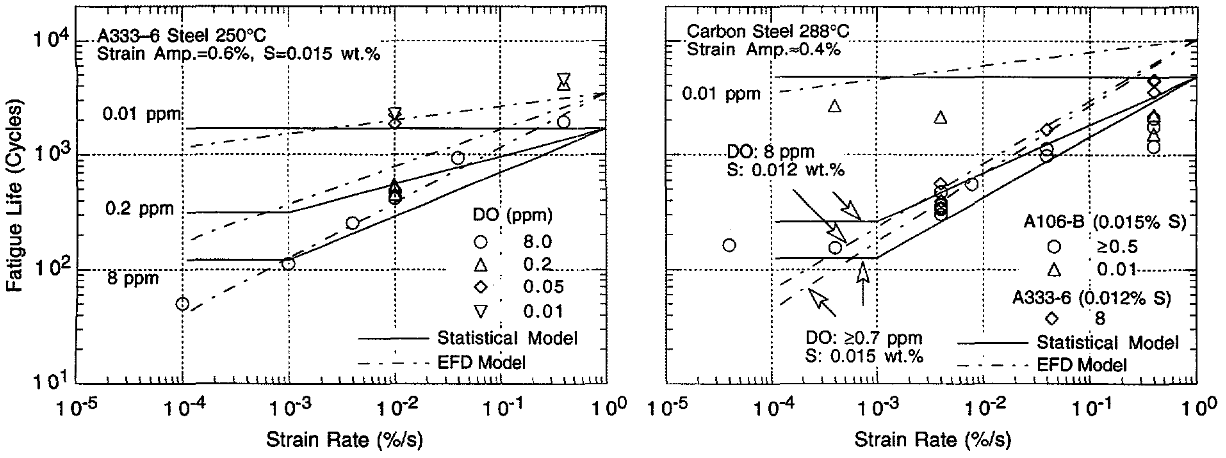

Figure 17. Dependence on strain rate of fatigue life of carbon steels observed experimentally and that estimated from the statistical and EFD models

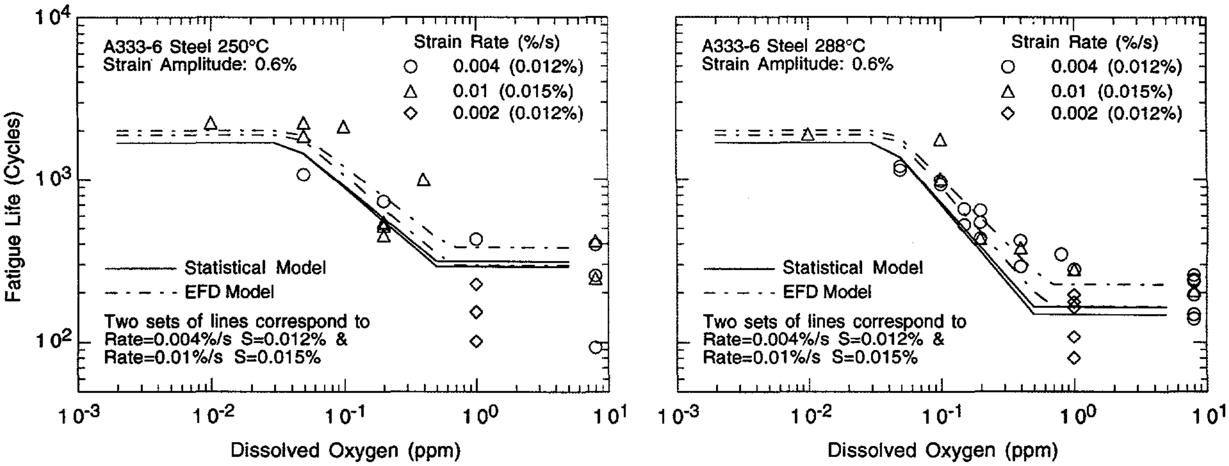

Figure 18. Dependence on dissolved oxygen of fatigue life of carbon steels observed experimentally and that estimated from the statistical and EFD models

(c) A threshold temperature of 150°C below which environmental effects on fatigue life are modest is considered in the statistical model but not in the EFD model.

(d) The EFD model includes the effect of tensile strength on fatigue life of CSs in LWR environments.

A fatigue life correction factor F_{en} can also be obtained from the statistical model, where

$$\ln(F_{en}) = \ln(N_{air}) - \ln(N_{water}). \tag{7}$$

From Eqs. 1a and 2a, the fatigue life correction factor for CSs is given by

$$\ln(F_{en}) = 0.585 - 0.00124T - 0.101S^*T^*O^*\dot{\varepsilon}^* \tag{8a}$$

and from Eqs. 1b and 2b, the fatigue life correction factor for LASs is given by

$$\ln(F_{en}) = 0.929 - 0.00124T - 0.101S^*T^*O^*\dot{\varepsilon}^*, \qquad (8b)$$

where the threshold and saturation values for S^*, T^*, O^*, and $\dot{\varepsilon}^*$ are defined in Eqs. 3a–3d. A value of 25°C is used for T in Eqs. 8a and 8b if the fatigue life correction factor is defined relative to room temperature air. Otherwise, both T and T^* represent the service temperature. A fatigue life correction factor F_{en} based on the statistical model has been proposed for ASME Section III fatigue evaluations.[57,58]

2.1.5 Design Fatigue Curves

The current ASME Section III Code design fatigue curves were based on experimental data on small polished test specimens. The best–fit curve to the experimental data, expressed in terms of stress amplitude S_a (MPa) and fatigue cycles N, for CSs is given by

$$S_a = 59{,}736/\sqrt{N} + 149.24 \qquad (9a)$$

and for LASs by

$$S_a = 49{,}222/\sqrt{N} + 265.45. \qquad (9b)$$

The stress amplitude S_a is the product of strain amplitude ε_a and elastic modulus E; the room temperature value of 206.8 GPa (30,000 ksi) for the elastic modulus for CSs and LASs was used in converting the experimental strain–versus–life data to stress–versus–life curves. The mean curve, expressed in terms of strain amplitude ε_a (%), for CSs is given by

$$\ln[N] = 6.726 - 2.0 \ln(\varepsilon_a - 0.0722) \qquad (10a)$$

and for LASs by

$$\ln[N] = 6.339 - 2.0 \ln(\varepsilon_a - 0.1283). \qquad (10b)$$

The best–fit curves were adjusted for the effect of mean stress by using the modified Goodman relation

$$S'_a = S_a\left(\frac{\sigma_u - \sigma_y}{\sigma_u - S_a}\right) \quad \text{for } S_a < \sigma_y, \qquad (11a)$$

and

$$S'_a = S_a \qquad \text{for } S_a > \sigma_y, \qquad (11b)$$

where S'_a is the adjusted value of stress amplitude, and σ_y and σ_u are the yield and ultimate strengths of the material, respectively. The Goodman relation assumes the maximum possible mean stress and typically gives a conservative adjustment for mean stress, at least when environmental effects are not significant. The design fatigue curves were then obtained by lowering the adjusted best–fit curve by a factor of 2 on stress or 20 on cycles, whichever was more conservative, at each point on the curve. The factor of 20 on cycles was intended to

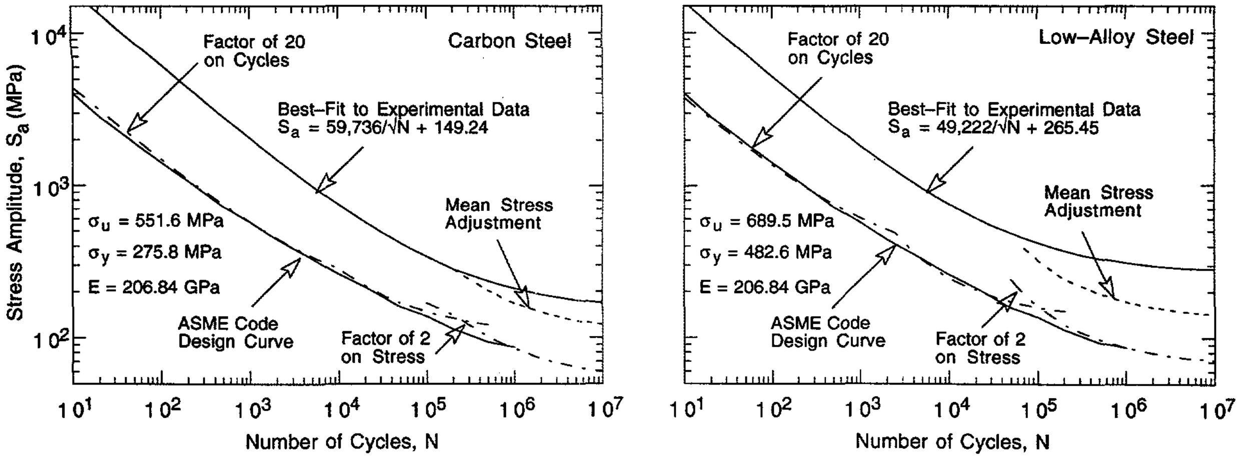

Figure 19. Adjustment for mean stress effects and factors of 2 and 20 applied to best-fit S-N curves for carbon and low-alloy steels to obtain the ASME Code design fatigue curve

account for the uncertainties in fatigue life associated with material and loading conditions, and the factor of 2 on strain was intended to account for uncertainties in threshold strain caused by material variability. This procedure is illustrated for CSs and LASs in Fig. 19.

The fatigue design curves for LWR environments are obtained by the same procedure that has been used for developing the current ASME Code fatigue design curves. For a specific set of environmental conditions, the best-fit curve is first adjusted for the effect of mean stress using the Goodman relation (Eq. 11) and then the curve is lowered by factors of 2 on stress and 20 on cycles to account for the differences and uncertainties in fatigue life associated with material and loading conditions. The stress-versus-life design curves were obtained from the strain-versus-life curves by using room-temperature values of the elastic modulus. The design fatigue curves based on the statistical model for CSs and LASs in air at room temperature and 288°C are shown in Fig. 20. The results indicate that for both steels the current ASME Code curve is conservative relative to the curves obtained from the statistical model. For LASs, the difference between the two curves is insignificant, whereas for CSs the fatigue lives predicted by the current Code curve at stress levels of 100–200 MPa (14.5–29 ksi) are more than a factor of 3 lower than those predicted by the curve from the statistical model.

Figure 21 shows the design curves for LWR environments under service conditions where any one of the following critical threshold conditions is true:

Temperature: <150°C
Dissolved Oxygen: <0.05 ppm
Strain Rate: ≥1%/s

A threshold value of sulfur content in the steel is not defined because limited data suggest that in high-DO water, the fatigue life of CSs may be independent of sulfur content in the range of 0.002–0.015 wt.%.

Figure 22 shows the design curves under service conditions where temperature and DO level are above the threshold value and strain rate is <1%/s. The design fatigue curves in water at 200, 250, and 288°C, corresponding to strain rates of 0.1, 0.01, and a saturation

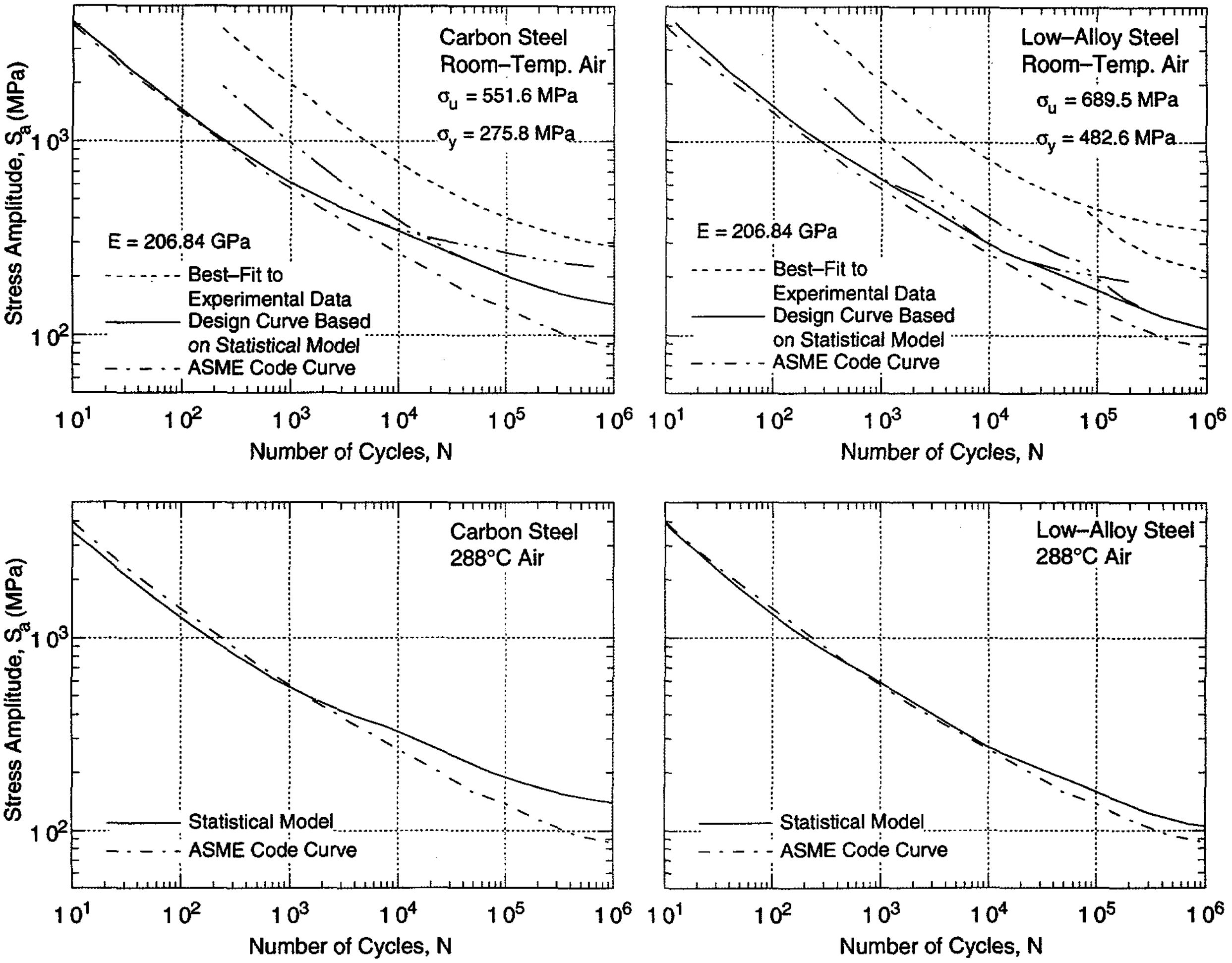

Figure 20. Fatigue design curves developed from the statistical model for carbon and low–alloy steels in air at room temperature and 288°C

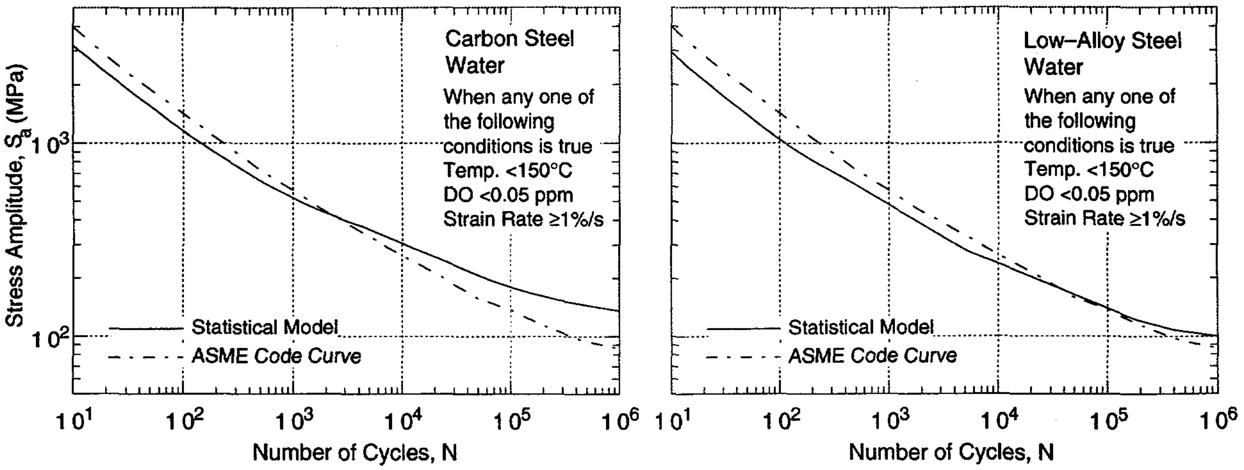

Figure 21. Fatigue design curves developed from statistical model for carbon and low–alloy steels under service conditions where one or more threshold values are not satisfied

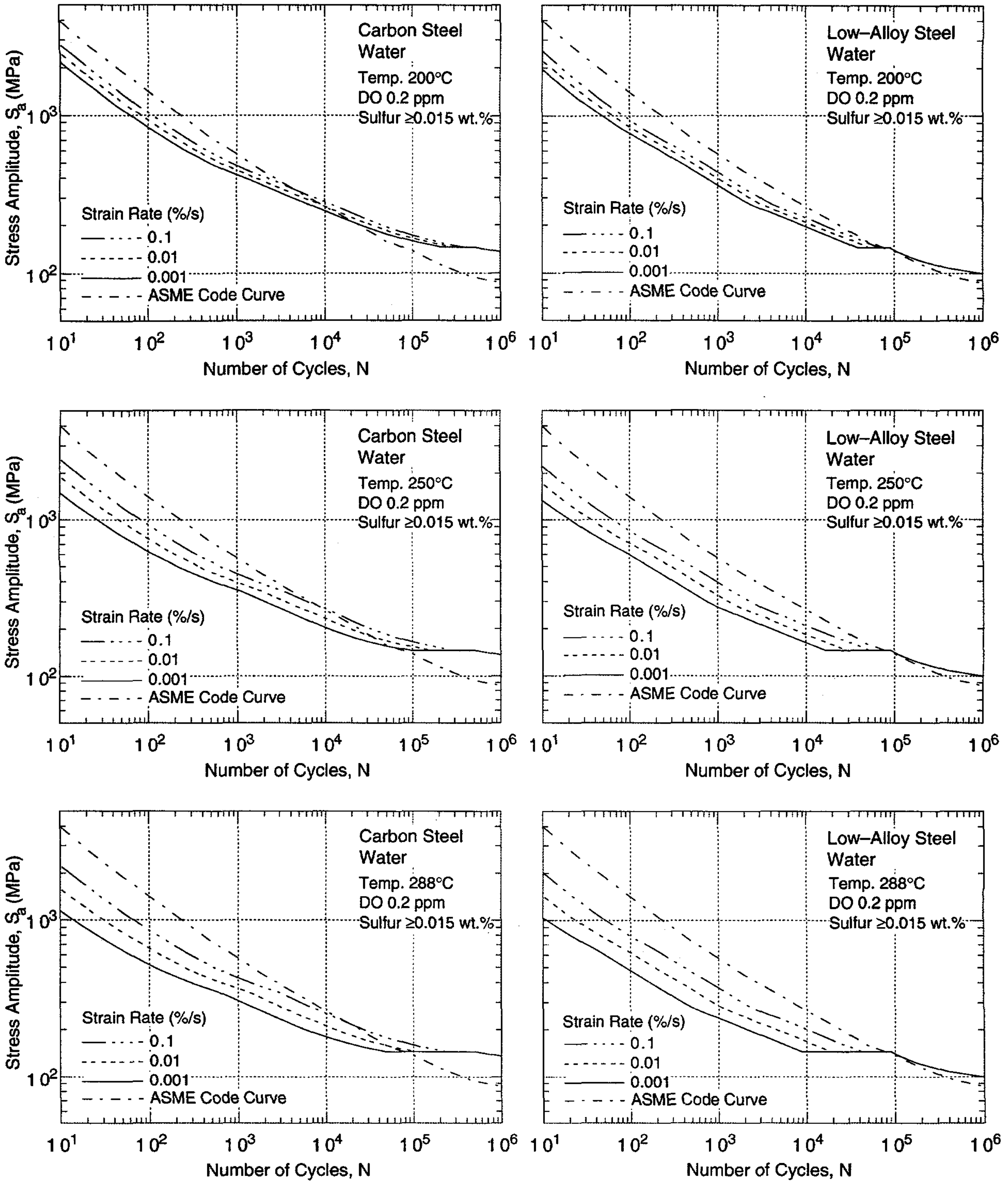

Figure 22. Fatigue design curves developed from statistical model for carbon and low–alloy steels under service conditions where all critical threshold values are satisfied

value of 0.001%/s, are shown in the figure. A DO level of 0.2 ppm in water and a high sulfur content (0.015 wt.% or higher) in the steels are assumed. Also, a minimum threshold strain amplitude is defined below which environmental effects are modest and are represented by the curves shown in Fig. 21. As discussed in Section 2.1.1, the threshold strain appears to be

≈20% higher than the fatigue limit of the steel. This translates to strain amplitudes of 0.140 and 0.185%, respectively, for CSs and LASs. These values have to be adjusted for mean stress effects and variability due to material and experimental scatter. To account for the effects of mean stress, the threshold strain amplitudes are decreased by ≈15% for CSs and by ≈40% for LASs; this results in a threshold strain amplitude of ≈0.12% for both steels. A factor of 1.7 on strain provides a 90% confidence for the variations in fatigue life associated with material variability and experimental scatter. Thus, a threshold strain amplitude of 0.07% (or a stress amplitude of 145 MPa) was selected for both steels.

The design fatigue curves in Figs. 21 and 22 can be used for ASME Section III fatigue evaluations in LWR applications. Note that these curves not only account for environmental effects but they also include minor differences that exist between the current ASME mean air curves and the present mean air curves that have been developed from a more extensive data base. Figure 20 shows that the differences are insignificant for LASs and may result in lower values of fatigue usage for CSs.

2.1.6 Conservatism in Design Fatigue Curves

The PVRC has been compiling and evaluating fatigue S–N data related to the effects of LWR coolant environments on the fatigue life of pressure boundary materials.[26] One of the tasks in the PVRC activity consisted of defining a set of values for material, loading, and environmental variables that result in moderate or acceptable effects of environment on fatigue life. A factor of 4 on the ASME mean life was chosen as a working definition of "moderate" or "acceptable" effects of environment, i.e., a decrease in fatigue life up to a factor of 4 due to environment is considered acceptable and does not require further fatigue evaluation. The bases for this criterion are that a factor of 4 on life constitutes normal data scatter and/or there is at least that much conservatism in the design fatigue curves.

The conservatism in ASME Code fatigue evaluation procedures have been demonstrated in fatigue tests on piping welds and components.[59] In air, the margins on the number of cycles to failure for elbows and tees were 118–2500 and 123–1700, respectively, for carbon steels. The margins for girth butt welds were significantly lower at 14–128. However, in these tests on welds and components, the fatigue life was expressed as the number of cycles for the crack to penetrate through the wall, which ranged from 6–18 mm (0.237–0.719 in.). The fatigue design curves represent the number of cycles to form a 3-mm-deep crack. Consequently, depending on the wall thickness, the actual margins to failure may be lower by more than a factor of 2. The main sources of conservatism are in the procedure for fatigue evaluation.

In addition, fatigue tests conducted on vessels at the Southwest Research Institute, San Antonio, TX, for the PVRC[60] show that ≈5-mm-deep cracks can form in CSs and LASs when the number of cycles is very near that predicted by the ASME Code design curve (Fig. 23). The tests were performed on 0.914-m (36 in.)-diameter vessels with 19 mm (0.75 in.) wall thickness in room-temperature water. These results demonstrate clearly that the Code design fatigue curves do not necessarily guarantee a margin of safety.

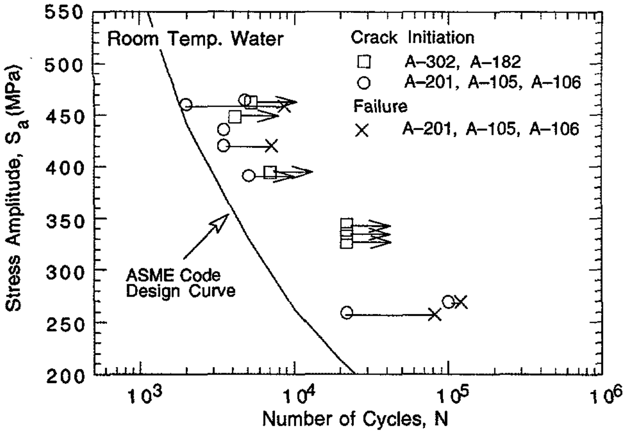

Figure 23.
Fatigue data for carbon and low–alloy steel vessels tested in room–temperature water

Structural Integrity Associates, Inc., under a contract to Sandia National Laboratories for the U.S. Department of Energy and in cooperation with the Electric Power Research Institute,[61] has documented the types and extent of conservatisms present in the ASME Section III fatigue evaluations and the effects of LWR environments on fatigue margins. A review of numerous stress reports indicated substantial conservatism in many component fatigue evaluations. The sources of conservatism include design transients considerably more severe than those experienced in service, grouping of transients, simplified elastic–plastic analysis, and Code rules prior to 1979. Environmental effects on two components, namely, a BWR feedwater nozzle/safe end and a PWR steam generator feedwater nozzle/safe end, which are known to be affected by severe thermal transients, were also investigated in the study. They concluded that the reductions in fatigue life due to environmental effects (factors of up to 40 and 22 for PWR and BWR nozzles, respectively) are more than offset by the margins in fatigue life (≈60 and 90, respectively, for PWR and BWR nozzles) found in typical ASME Code fatigue evaluations. The margins of ≈60 and 90 on fatigue life were determined from the ratio of CUFs based on the mean experimental S–N curve and the Code design fatigue curve. In other words, the factors of 2 on stress and 20 on cycles are considered safety margins in these evaluations. The margins of ≈60 and 90 would be true only if it was demonstrated that the fatigue S–N curve for these specific components was comparable to or better than the mean experimental curve, and that the effects of mean stress, loading sequence, or component size and geometry are insignificant.

The results of a rigorous statistical analysis have been used to estimate the probability of initiating fatigue cracks in CS and LAS components.[24,25] The results indicate that in room–temperature air, the current ASME Code design fatigue curve represents <5% probability of fatigue cracking in LAS components and <1% probability in CS components. Data available in the literature have been reviewed to evaluate the effects of various material, loading, and environmental variables on the fatigue life of structural materials in air and LWR environments.[24,25] The subfactors that may be used to account for the effects of these variables on fatigue life are summarized in Table 1. The factors on strain primarily account for the variation in threshold strain (i.e., fatigue limit of the material) caused by material variability, component size and surface finish, and load history. The effects of these parameters on threshold strain are judged not to be cumulative but rather are controlled by the parameter that has the largest effect. Thus, a factor of at least 1.5 on strain and 10 on cycles is needed to account for the differences and uncertainties in relating the fatigue lives of laboratory test specimens to those of large components. In high–temperature water, the effect of surface finish may not be significant; CS and LAS surfaces develop a corrosion scale of magnetite (Fe_3O_4). For LWR environments, a subfactor on life to account for surface finish effects may be as low as 1.5 or may be eliminated completely. Therefore, a factor of 3 or perhaps 4 on life appears reasonable for defining moderate or acceptable effects of environment on fatigue life of CSs and LASs.

Table 1. Factors on cycles and on strain to be applied to mean S–N curve

Parameter	Factor on Life	Factor on Strain
Material variability & experimental scatter	2.5	1.4–1.7
Size effect	1.4	1.25
Surface finish	2.0–3.0	1.3
Loading history	1.5–2.5	1.5
Total adjustment:	10.0–26.0	1.5–1.7

2.1.7 Fatigue Evaluations in LWR Environments

The ASME Boiler and Pressure Vessel Code Section III[1] contains rules for the construction of nuclear power plant Class 1 components. It provides the requirements for design against cyclic loadings that occur on a structural component because of changes in the mechanical and thermal loadings as the system goes from one load set (pressure, temperature, moment, and force) to any other load set. The ASME Section III, NB–3600 (piping design) methodology is used exclusively for piping and sometimes for branch nozzles. The ASME Section III, NB–3200 (design by analysis) methodology is generally used for vessels and frequently for nozzles. In both analyses, the various sets of load states are first defined at the most highly stressed locations in the component. The load states are defined in terms of the three principal stresses in NB–3200 analysis, and in terms of internal pressure, moments, average temperature, and temperature gradients in NB–3600 analysis. A peak stress–intensity range and an alternating stress–intensity amplitude S_a is then calculated for each load state. The value of S_a is used to first obtain the allowable number of cycles from the design fatigue curve and then to calculate the fatigue usage associated with that load state. The CUF is the sum of the partial usage factors. The Section III, NB–3200– or NB–3600–type analyses for components for service in LWR environments can be performed using the design fatigue curves presented in Figs. 21 and 22. Note that fatigue evaluations performed with the updated curves not only account for environmental effects but also include minor differences between the current ASME mean air curves and the statistical model air curves. Figure 20 shows that the current Code curves are somewhat conservative for CSs.

An alternative approach for fatigue evaluations in LWR environments has been proposed by EPRI[57,58] and by the EFD committee of TENPES of Japan.* The effects of LWR coolant environments on fatigue S–N curves are expressed in terms of a fatigue life correction factor F_{en}. In the EPRI approach, F_{en} is expressed as the ratio of the life in air to that in water, both at service temperature, whereas in the EFD approach, F_{en} is expressed as the ratio of the life in air at room temperature to that in water at service temperature. The effects of environment are incorporated into the ASME fatigue evaluation by obtaining a fatigue usage for a specific

---

*Presented at the Pressure Vessel Research Council Meeting, April 1996, Orlando, FL.

load pair based on the current Code design curves and multiplying it by the correction factor. Fatigue evaluations performed using F_{en} incorporate the effect of environment alone in the EPRI approach, whereas the EFD approach accounts for both effects of environment as well as temperature, that might exist in air.

Both approaches require additional information on service conditions, e.g., temperature, strain rate, and DO level. The procedure for obtaining these parameters depends on the details of the available information, i.e., whether the elapsed time versus temperature information for the transient is available. The values of temperature and DO may be conservatively taken as the maximum values for the transient. As discussed in Section 2.1.1, an average temperature may be used if the time versus temperature information is available. Because environmental effects on fatigue life are modest below 150°C and the threshold strain, the average temperature should be determined by the average of the maximum temperature and either 150°C or the temperature at threshold strain, whichever is higher. An average strain rate is generally used for each load state; it is obtained from the peak strain and elapsed time for the transient. However, fatigue monitoring data indicate that actual strain rates may vary significantly during the transient. The slowest strain rate can be used for a conservative estimate of life.

An "improved-rate approach" has been proposed for obtaining the fatigue life correction factor F_{en} under conditions of varying temperature, strain rate, and DO level.[11] During each loading cycle, F_{en} is assumed to vary linearly with strain increments. The effective correction factor F'_{en} for varying conditions is expressed as

$$F'_{en} = 1 + \int_{\varepsilon_{th}}^{\varepsilon_{\max}} \frac{F_{en} - 1}{\varepsilon_{\max} - \varepsilon_{th}} d\varepsilon, \tag{12}$$

where $\varepsilon_{\max}$ and ε_{th} are the maximum and threshold values of strain, respectively. For varying service conditions, Eq. 12 may be written in terms of the effective fatigue life in water N'_{water} expressed as

$$\frac{1}{N'_{water}} = \int_{\varepsilon_{th}}^{\varepsilon_{\max}} \frac{1}{N_{water}} \frac{d\varepsilon}{(\varepsilon_{\max} - \varepsilon_{th})} \tag{13}$$

or

$$\frac{1}{N'_{water}} = \int_{T_{th}}^{T_{\max}} \frac{1}{N_{water}} \frac{dT}{(T_{\max} - T_{th})}, \tag{14}$$

where N_{water} is the life under constant temperature and strain rate, and $T_{\max}$ and T_{th} are the maximum and threshold values of temperature, respectively.

Sample fatigue evaluations have been performed for an SA-508 Cl 1 CS feedwater nozzle safe end and SA-333 Gr 6 CS feedwater line piping for a BWR and an SA-508 Cl 2 LAS outlet nozzle for a PWR vessel; the results are given in Tables 2-4. The stress records and the associated service conditions were obtained from Ref. 27. The following three methods were used to calculate the CUF:

(a) For each set of load pair, a partial usage factor was obtained from the appropriate design fatigue curve shown in Figs. 21-22.

Table 2. Fatigue evaluation for SA-508 Cl 1 carbon steel feedwater nozzle safe end for a BWR

S_{alt}	Temp.	Strain Rate	Design Cycles	ASME Code Curve		Curves Based on Statistical Model		Correction Based on Statistical Model		Correction Based on EFD Model	
(MPa)	(°C)	(%/s)	n	N	U_{air}	N	U_{env}	F_{en}	U_{env}	F_{en}	U_{env}
567.2	200	0.028	120	1024	0.1172	417	0.2878	2.18	0.2552	2.52	0.2956
500.6	200	0.026	90	1429	0.0630	617	0.1459	2.20	0.1384	2.57	0.1619
444.1	200	0.026	142	1967	0.0722	1000	0.1420	2.20	0.1586	2.57	0.1856
268.8	200	0.002	555	9272	0.0599	6457	0.0860	3.01	0.1804	4.99	0.2989
201.9	200	0.001	10	23830	0.0004	21878	0.0005	3.28	0.0014	5.97	0.0025
143.8	200	0.001	120	81350	0.0015	229087	0.0005	1.00	0.0015	1.00	0.0015
132.4	200	0.001	98	115630	0.0008	1288250	0.0001	1.00	0.0008	1.00	0.0008
121.1	200	0.001	10	159810	0.0001	2000000	–	1.00	0.0001	1.00	0.0001
120.2	288	0.001	10	163810	0.0001	2000000	–	1.00	0.0001	1.00	0.0001
95.5	288	0.001	222	444850	0.0005	2000000	0.0001	1.00	0.0005	1.00	0.0005
92.6	200	0.001	666	523970	0.0013	2000000	0.0003	1.00	0.0013	1.00	0.0013
91.9	288	0.001	120	560450	0.0002	2000000	–	1.00	0.0002	1.00	0.0002
					0.3171		0.6632		0.7384		0.9489

Table 3. Fatigue evaluation for SA-333 Gr 6 carbon steel feedwater line piping for a BWR

S_{alt}	Temp.	Strain Rate	Design Cycles	ASME Code Curve		Curves Based on Statistical Model		Correction Based on Statistical Model		Correction Based on EFD Model	
(MPa)	(°C)	(%/s)	n	N	U_{air}	N	U_{env}	F_{en}	U_{env}	F_{en}	U_{env}
758.9	200	0.117	5	447	0.0112	229	0.0218	1.82	0.0204	1.74	0.0195
744.4	200	0.114	5	468	0.0107	245	0.0204	1.83	0.0195	1.75	0.0187
734.4	200	0.113	5	490	0.0102	251	0.0199	1.83	0.0186	1.76	0.0179
654.2	200	0.001	8	692	0.0116	363	0.0396	3.25	0.0376	5.97	0.0691
616.4	200	0.095	10	776	0.0129	407	0.0246	1.87	0.0241	1.84	0.0237
608.6	200	0.094	5	832	0.0060	437	0.0114	1.87	0.0112	1.84	0.0111
598.3	200	0.041	126	871	0.1447	479	0.2630	2.07	0.2991	2.29	0.3306
561.4	215	0.086	10	1096	0.0091	603	0.0166	2.03	0.0185	1.97	0.0180
468.4	200	0.001	97	1698	0.0571	603	0.1609	3.25	0.1858	5.97	0.3412
459.9	200	0.001	14	1820	0.0077	676	0.0207	3.25	0.0250	5.97	0.0460
422.6	200	0.001	6	2344	0.0026	955	0.0063	3.25	0.0083	5.97	0.0153
421.7	212	0.001	64	2239	0.0286	955	0.0670	3.92	0.1121	6.59	0.1884
382.7	200	0.001	92	3090	0.0298	1445	0.0637	3.25	0.0968	5.97	0.1779
321.5	215	0.001	88	5623	0.0157	3090	0.0285	4.11	0.0643	6.76	0.1058
295.6	212	0.001	15	7413	0.0020	4467	0.0034	3.92	0.0079	6.59	0.0133
271.9	215	0.001	212	8710	0.0243	6310	0.0336	4.11	0.1000	6.76	0.1646
262.9	224	0.001	69	9772	0.0071	7244	0.0095	4.73	0.0334	7.32	0.0517
253.7	224	0.001	11	11220	0.0010	8511	0.0013	4.73	0.0046	7.32	0.0072
236.6	215	0.001	60	13804	0.0043	11220	0.0053	4.11	0.0179	6.76	0.0294
227.2	200	0.001	203	15849	0.0128	13490	0.0150	3.25	0.0416	5.97	0.0765
224.3	200	0.001	360	16218	0.0222	14125	0.0255	3.25	0.0722	5.97	0.1326
205.3	200	0.025	222	21878	0.0101	26687	0.0083	2.20	0.0223	2.60	0.0264
179.9	212	0.028	30	33884	0.0009	50720	0.0006	2.37	0.0021	2.65	0.0023
179.5	200	0.028	81	33113	0.0024	50720	0.0016	2.17	0.0053	2.52	0.0062
149.2	212	0.001	96	63096	0.0015	141254	0.0007	3.92	0.0060	6.59	0.0100
141.8	200	0.001	40	83176	0.0005	602560	0.0001	1.00	0.0005	1.00	0.0005
97.8	200	0.001	30	389045	0.0001	2137962	0.0000	1.00	0.0001	1.00	0.0001
77.4	200	0.001	11545	2238721	0.0052			1.00	0.0052	1.00	0.0052
					0.4522		0.8693		1.2603		1.9091

Table 4. Fatigue evaluation for SA-508 Cl 2 low-alloy steel outlet nozzle for a PWR

S_{alt}	Temp.	Strain Rate	Design Cycles	ASME Code Curve		Curves Based on Statistical Model		Correction Based on Statistical Model		Correction Based on EFD Model[a]	
(MPa)	(°C)	(%/s)	n	N	U_{air}	N	U_{env}	F_{en}	U_{env}	F_{en}	U_{env}
335.6	–	–	80	4670	0.0171	2573	0.0311	1.77	0.0303	–	–
313.0	–	–	10	5741	0.0017	3091	0.0032	1.77	0.0031	–	–
305.7	–	–	20	6010	0.0033	3388	0.0059	1.77	0.0059	–	–
275.4	–	–	20	8098	0.0025	4670	0.0043	1.77	0.0044	–	–
237.1	–	–	70	13723	0.0051	9508	0.0074	1.77	0.0090	–	–
202.1	–	–	130	23795	0.0055	24912	0.0052	1.77	0.0097	–	–
195.1	–	–	150	26082	0.0058	27939	0.0054	1.77	0.0102	–	–
186.8	–	–	50	29251	0.0017	32061	0.0016	1.77	0.0030	–	–
186.1	–	–	30	28587	0.0010	33566	0.0009	1.77	0.0019	–	–
147.3	–	–	40	68338	0.0006	76641	0.0005	1.77	0.0010	–	–
139.3	–	–	1930	94211	0.0205	94211	0.0205	1.00	0.0205	–	–
139.3	–	–	2000	94211	0.0212	94211	0.0212	1.00	0.0212	–	–
138.8	–	–	9270	94211	0.0984	94211	0.0984	1.00	0.0984	–	–
130.0	–	–	60	115810	0.0005	115810	0.0005	1.00	0.0005	–	–
127.1	–	–	230	132894	0.0017	129881	0.0018	1.00	0.0017	–	–
126.5	–	–	10	135977	0.0001	135977	0.0001	1.00	0.0001	–	–
124.5	–	–	80	142360	0.0006	149041	0.0005	1.00	0.0006	–	–
121.6	–	–	160	149041	0.0011	183210	0.0009	1.00	0.0011	–	–
121.6	–	–	26400	152499	0.1731	167150	0.1579	1.00	0.1731	–	–
117.6	–	–	2000	167150	0.0120	205470	0.0097	1.00	0.0120	–	–
113.0	–	–	400	191809	0.0021	252575	0.0016	1.00	0.0021	–	–
110.2	–	–	13200	215114	0.0614	310479	0.0425	1.00	0.0614	–	–
106.0	–	–	13200	241252	0.0547	364547	0.0362	1.00	0.0547	–	–
102.7	–	–	80	289835	0.0003	617784	0.0001	1.00	0.0003	–	–
102.3	–	–	80	289835	0.0003	603777	0.0001	1.00	0.0003	–	–
101.4	–	–	70	317682	0.0002	777031	0.0001	1.00	0.0002	–	–
					0.4924		0.4576		0.5266		

[a] Not calculated because strain rates were not available in the stress records.

(b) For each set of load pairs, a partial usage factor was first obtained from the current ASME Code design curve. This value was adjusted for environmental effects by multiplying by F_{en}, which is calculated from Eqs. 8a and 8b. F_{en} values were calculated for only those load pairs that satisfy the following three threshold conditions: temperature ≥150°C, strain rate ≤1%/s, and stress amplitude ≥145 MPa (≥21 ksi). The DO level was assumed to be 0.2 ppm. Also, because the sulfur content in the steel is not always available, a conservative value of 0.015 wt.% was assumed.

(c) The same procedure as item (b), except that F_{en} was calculated from the EFD correlations of Eqs. 4a–6d for load pairs with stress amplitudes ≥145 MPa (≥21 ksi). The DO level was assumed to be 0.2 ppm and a sulfur content of 0.015 wt.%. Also, σ_u in Eq. 6b was assumed to be 520 MPa for CSs and 650 MPa for LASs.

The results indicate that the approach using F_{en} yields higher values of CUF than those obtained from the design fatigue curves that have been adjusted for environmental effects. The difference arises because the environmentally adjusted design curves not only account for the environment but also for the difference between the ASME mean air curve and statistical model air curve. Figure 20 shows that for CSs, this difference can be significant at stress amplitudes <180 MPa (<26 ksi). The results also show that for the feedwater nozzle safe end and the feedwater line piping, the BWR environment increases the fatigue usage by a factor of

≈2. For the LAS outlet nozzle of a PWR, the effect environment on fatigue usage is insignificant. The CUF values from the EFD model were not calculated because information regarding the strain rate was not available in the stress records. For stress levels above ≈145 MPa (21 ksi), the EFD approach would yield F_{en} values of 1.25 and 1.95 for strain rates of 0.1 and 0.001%/s, respectively.

2.2 Austenitic Stainless Steels

(O. K. Chopra and J. L. Smith)

Fatigue tests are being conducted on Types 304 and 316NG SS in air and LWR environments to evaluate the effects of material and loading variables such as steel type, strain rate, DO, and strain range, on the fatigue lives of these steels. Compositions of the steels are given in Table 5; details about the test facility and procedure have been described elsewhere.[16] The fatigue test data obtained to date were presented in Ref. 19. During the present reporting period, fatigue tests have been conducted on Type 304 SS to determine the effects of strain rate on fatigue life and to establish the threshold strain range below which environmental effects on fatigue life either do not occur or are insignificant.

Table 5. Composition (in wt.%) of austenitic stainless steels used for fatigue tests

Material	Heat	Source	C	P	S	Si	Cr	Ni	Mn	Mo	Cu	N
Type 316NG[a]	D432804	Vendor	0.011	0.020	0.001	0.52	17.55	13.00	1.76	2.49	0.10	0.108
		ANL	0.013	0.020	0.002	0.49	17.54	13.69	1.69	2.45	0.10	0.105
Type 304 [b]	30956	Vendor	0.060	0.019	0.007	0.48	18.99	8.00	1.54	0.44	–	0.100

[a] ASME SA312 seamless stainless steel pipe (hot finished), 610 mm O.D. and 30.9 mm wall, fabricated by Sumitomo Metal Industries, Ltd. Solution-annealed at 1038–1093°C for 0.5 h and water-quenched.
[b] Solution-annealed at 1050°C for 0.5 h.

The fatigue S–N data for Types 316NG and 304 SS in air and water environments at 288°C are shown in Fig. 24, as is the ASME Code fatigue design curve. The results indicate a significant decrease in fatigue life in water relative to that in air; the reduction in life depends both on strain rate and DO content in water. The fatigue lives of Types 316NG and 304 SS in air, simulated PWR, and high–DO water are plotted as a function of strain rate in Fig. 25. In all environments, the fatigue lives of these steels decrease with decreasing strain rate. The effect of strain rate is the smallest in air and largest in a low–DO PWR environment.

In Fig. 24, the strain range of the tests on Type 304 SS at ≈0.3% strain range was increased from 0.30 to 0.32% after the test in air had accumulated ≈625,860 cycles and that in PWR water ≈89,860 cycles. The specimen in air failed after an additional 331,300 cycles and that in PWR water after 41,240 additional cycles. These results suggest a threshold strain range of ≈0.3% for the heat of Type 304 SS used in the present study, i.e., below 0.3% strain range, environmental effects on fatigue life are either insignificant or do not occur. Additional tests will be conducted to confirm these results and establish the threshold strain in high–DO water.

The results also indicate that environmental effects on the fatigue life of austenitic SSs are more pronounced in low–DO than in high–DO water. At slow strain rates, e.g., ≈0.004%/s, the reduction in fatigue life in a simulated PWR environment (<10 ppb DO) is greater by a factor of ≈2 than in high–DO water (≥200 ppb DO). Such a dependence of fatigue life on DO content is quite different than that for ferritic steels. As discussed in Section 2.1, environmental effects on fatigue life of CSs and LASs increase with increasing DO content above a minimum threshold value of 0.05 ppm. Also, for CSs and LASs, environmental effects on the fatigue life are modest at DO levels below 0.05 ppm, i.e., fatigue life is lower by a factor of < 2 than that in air. The results also indicate that in a PWR environment, the effect of strain rate on life does not saturate even at a strain rate of 0.0004%/s. Fatigue tests are in progress at lower strain rates to establish the saturation strain rate in LWR environments.

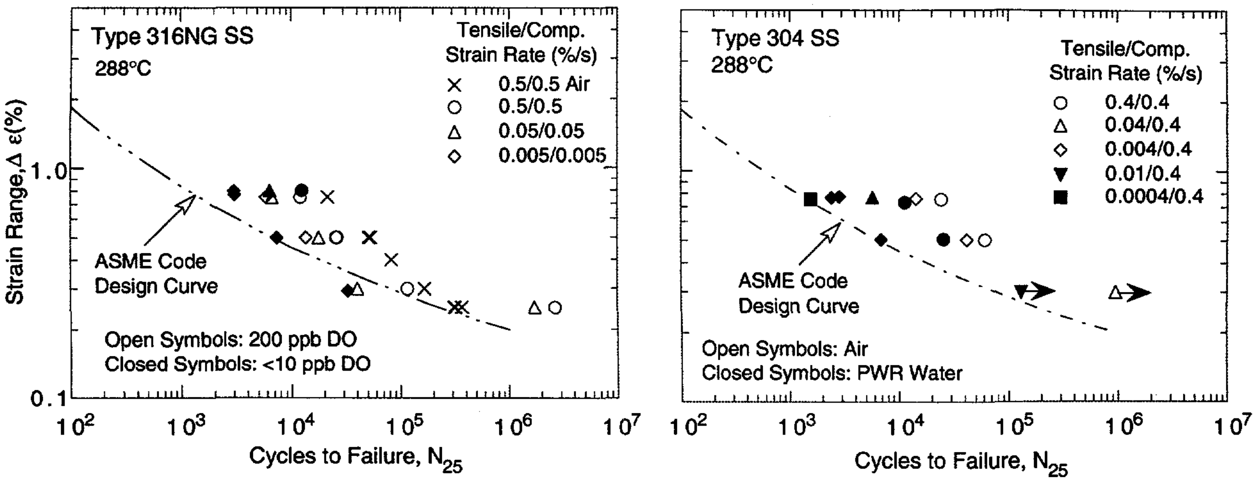

Figure 24. Total strain range versus fatigue–life data for Types 316NG and 304 SS in air and water

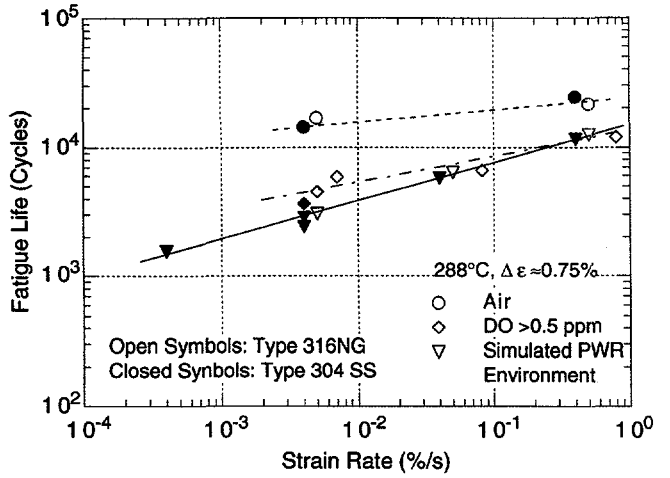

Figure 25.
Effect of strain rate on fatigue lives of austenitic SSs in air, and simulated PWR and high–DO water environments

3 Irradiation-Assisted Stress Corrosion Cracking of Austenitic SS

In recent years, failures of reactor–core internal components in both BWRs and PWRs have increased after accumulation of relatively high fluence (>5 x 10^{20} n·cm^{-2}, E >1 MeV). The general pattern of the observed failures indicates that as nuclear plants age and neutron fluence increases, various apparently nonsensitized austenitic SSs become susceptible to intergranular failure. Some components are known to have cracked under minimal applied stress. Although most failed components can be replaced, some safety–significant structural components (e.g., BWR top guide, shroud, and core plate) would be very difficult or impractical to replace. Therefore, the structural integrity of these components after accumulation of high fluence has been a subject of concern and extensive research to provide an understanding of this type of degradation, which is commonly known as IASCC.

Primary effects of irradiation include alteration of microchemistry, microstructure, and mechanical properties of the structural material, usually fabricated from ASTM Type 304, 304L, 316, or 348 SSs. Irradiation produces defects and defect clusters in grain matrices, and alters the dislocation network, dislocation loop, and dislocation channel structures, leading to radiation-induced hardening. Irradiation also leads to changes in the stability of second-phase precipitates and the local alloy chemistry near grain boundaries, precipitates, and defect clusters. Grain-boundary microchemistry that differs significantly from that of the bulk composition can be produced in association with not only radiation-induced segregation (RIS) but also thermally driven equilibrium and nonequilibrium segregation of alloying and impurity elements. Neutron irradiation also alters the water chemistry, in particular, near the grain-boundary surfaces in a crack-tip region.

Irradiation-induced grain-boundary depletion of chromium has been considered for many years to be the primary metallurgical process that causes IASCC. One of the most important factors that has been considered by many investigators to support the chromium-depletion mechanism is that the dependence on water chemistry (i.e., oxidizing potential) of IGSCC of nonirradiated thermally sensitized material and of IASCC of BWR-irradiated solution-annealed material is similar. Recent attention also has focused on the effects of fabrication-related variables, i.e., grain-boundary segregation and depletion of alloying and impurity elements by thermal processes, the effect of final thermomechanical treatment, cold work, and contamination by minor impurities during welding of field components such as BWR core shrouds.

Although BWR core shrouds are subject to relatively low neutron fluence, many vertical and horizontal welds crack by the time they accumulate relatively low fluences of $\approx 2 \times 10^{19}$ to $\approx 5 \times 10^{20}$ n·cm^{-2}. At these low fluences, nonwelded base-metal components fabricated from Types 304 and 304L SS would not be considered susceptible to IASCC, which typically occurs after a threshold fluence of $\approx 5 \times 10^{20}$ n·cm^{-2}. Partly because of this, most cases of core shroud cracking have been attributed to classical IGSCC of thermally sensitized SS, in which significant thermal sensitization by grain-boundary carbide precipitation has been assumed to occur in the heat-affected zone (HAZ) of a core shroud during welding. However, an increasing number of cracking incidents is observed in core shrouds fabricated from Type 304L SS, and it is difficult to explain this on the basis of classical IGSCC because thermal sensitization by grain-boundary carbide precipitation would not be expected in low-carbon Type 304L SSs.

In the present reporting period, our effort has focused on SSRT testing of model SS alloys irradiated in the Halden reactor, microchemical and microstructural characterization of simulated core internal welds, and analysis of cracked BWR core shrouds aimed at understanding the cracking mechanism.

3.1 Slow-Strain-Rate-Tensile Tests of Model Austenitic Stainless Steels Irradiated in the Halden Reactor
(H. M. Chung, W. E. Ruther, R. V. Strain, and T. M. Karlsen*)

Slow–strain–rate–tensile (SSRT) tests and fractographic analysis by scanning electron microscopy (SEM) have been completed for the model SS alloys that were irradiated to a fluence of ≈0.45 x 10^{21} n·cm^{-2} (E >1 MeV) at ≈288°C in a helium environment in the Halden reactor. In addition to 14 irradiated alloy specimens, nonirradiated control specimens were tested at 288°C in simulated BWR water that contained ≈8 ppm DO. Strain rate was kept constant at 1.65 x 10^{-7} s^{-1}. Electrochemical potential (ECP) was measured at the effluent side at regular intervals.

Test results are summarized in Table 6. Also shown in the table are results of SEM fractographic analysis of the failure behavior of the specimens. In Tables 7 and 8, the results of SSRT (uniform and total plastic strains and yield and maximum stresses) and SEM fractographic analysis (percent IGSCC, percent TGSCC, and combined percent IGSCC plus TGSCC) are correlated with compositional characteristics of the alloys.

Surprisingly, a few heats exhibited significant susceptibility to TGSCC or low ductility even in the nonirradiated state (Table 7). Heats L7 (Type 304 SS, high in oxygen), L2 (Type 304SS, high in sulfur), and L24 (high-purity Type 348 SS) exhibited unusually low uniform elongation in water even in the nonirradiated state, i.e., only 5-10% versus 12-50% for other steels listed in the table. Heat L7, which contains ≈274 wppm oxygen in contrast to a normal oxygen level of <100 wppm, exhibited high uniform elongation (42.3%) when tested in air, whereas uniform elongation was only ≈5.7% when tested in water. This indicates a significant effect of oxygen dissolved in the material on SSRT properties in oxygenated water. Sulfur and nitrogen contents were high (≈340 wppm and ≈0.102 wt.%, respectively) in Type 304 SS Heat L2, which also exhibited unusually low uniform elongation of ≈6.6%. The fracture morphology of specimens from Heats L7 and L2 exhibited ≈20% and ≈57% TGSCC, respectively, even in the nonirradiated state.

Total elongation obtained from the nonirradiated control and low-fluence-irradiated specimens is plotted for each alloy in Figs. 26 and 27, respectively. Total elongation correlates well with the combined concentrations of nitrogen and silicon contents of the alloy (Fig. 28). Consistent with this, a careful examination of Table 7 and Fig. 27 reveal a clear trend that all alloys that contain low levels of nitrogen (<0.01 wt.%) and silicon (<0.5 wt.%) exhibit unusually low ductility despite whether the carbon content is low or high. This trend was also valid in terms of susceptibility to TGSCC (Fig. 29). That is, alloys that contain low levels of nitrogen (<0.01 wt.%) and silicon (<0.5 wt.%) exhibit unusually high susceptibility to TGSCC.

However, an alloy (L13) that contains relatively high silicon (≈1.18 wt.%) exhibited low susceptibility to TGSCC and high ductility despite the fact that it has a very low nitrogen content (0.001 wt.%). When nitrogen content was > 0.01 wt.%, neither low ductility nor high susceptibility to TGSCC was observed regardless of silicon content (Fig. 30 and Table 7). As fluence increases, high susceptibility to IGSCC is observed in an alloy that exhibits high

---

*OECD Halden Reactor Project, Halden N-1751, Norway.

Table 6. Results of SSRT[a] test and SEM fractography for model austenitic stainless steel alloys irradiated in helium at 289°C in the Halden reactor to a fluence of ≈0.45×10^{21} $n \cdot cm^{-2}$ (E > 1 MeV)

Alloy Ident. No.	Fast–Neutron Fluence ($n \cdot cm^{-2}$)	SSRT No.	Feedwater Chemistry: Oxygen Conc. (ppm)	Feedwater Chemistry: Average ECP (mV SHE)	Feedwater Chemistry: Cond. at 25°C ($\mu S \cdot cm^{-1}$)	Feedwater Chemistry: pH at 25°C	SSRT Parameters: Max. Stress (MPa)	SSRT Parameters: Uniform Elong. (%)	SSRT Parameters: Total Elong. (%)	Fracture Behavior: TGSCC (%)	Fracture Behavior: IGSCC (%)	Fracture Behavior: TGSCC+ IGSCC (%)
L23	0	CHR-1	8.6	+228	0.07	6.65	480	15.6	17.0	-	-	-
L7	0	CHR-2	8.0	+217	0.07	7.37	370	5.7	7.2	20[b]	0	20
L7	0	CHR-7		Test in air			572	42.3	43.9	0	0	0
L14	0	CHR-3	8.6	+208	0.07	7.37	474	41.8	44.2	0	0	0
L17	0	CHR-4	7.5	+262	0.06	7.09	412	11.6	13.3	60	0	60
L6	0	CHR-5	7.9	+256	0.08	6.85	545	43.0	44.5	0	0	0
L27	0	CHR-6	9.3	+247	0.08	6.96	483	20.6	22.9	0	0	0
L26	0	CHR-8	9.4	+223	0.07	6.65	596	38.2	40.2	0	0	0
L2	0	CHR-9	8.6	+292	0.06	6.55	348	6.6	7.8	57	0	57
L25	0	CHR-10	8.2	+239	0.06	6.42	458	25.5	27.0	0	0	0
L15	0	CHR-11	8.2	+195	0.06	6.32	512	36.7	37.9	0	0	0
L24	0	CHR-12	8.4	+200	0.07	6.20	461	10.4	12.3	-	-	-
C1	0	CHR-13	8.1	+187	0.07	6.33	498	49.4	51.7	0	0	0
C19	0	CHR-14	8.8	+179	0.08	6.29	501	47.4	49.2	0	0	0
C9	0	CHR-15	8.5	+166	0.07	6.83	408	17.4	19.4	-	-	-
C1	0.45×10^{21}	HR-1	8.3	+184	0.07	7.03	680	13.4	16.6	4	0	4
L5	0.45×10^{21}	HR-2	9.7	+208	0.07	6.89	539	29.5	32.7	2	2	4
L22	0.45×10^{21}	HR-3	8.0	+236	0.07	6.80	596	6.6	9.4	50	15	65
C3	0.45×10^{21}	HR-4	8.7	+161	0.07	6.68	491	27.7	31.6	5	0	5
C16	0.45×10^{21}	HR-5	8.3	+204	0.08	6.74	527	17.6	20.6	2	0	2
L4	0.45×10^{21}	HR-6	9.0	+202	0.08	6.70	542	19.7	22.3	38	0	38
L18	0.45×10^{21}	HR-7	9.0	+203	0.08	6.33	572	6.3	8.8	54	0	54
C10	0.45×10^{21}	HR-8	8.2	+174	0.07	6.35	640	17.4	18.9	6	0	6
C21	0.45×10^{21}	HR-9	8.1	+149	0.08	6.49	620	15.9	19.4	4	0	4
L11	0.45×10^{21}	HR-10	9.0	+157	0.08	6.17	599	2.3	3.8	62	0	62
L13	0.45×10^{21}	HR-11	8.7	+164	0.08	6.17	461	22.1	24.8	8	0	8
L20	0.45×10^{21}	HR-12	8.4	+174	0.07	6.20	552	2.9	5.1	32	2	34
C19	0.45×10^{21}	HR-13	9.5	+132	0.12	6.36	682	10.5	14.7	7	0	7
C9	0.45×10^{21}	HR-14	8.0	+192	0.11	6.30	607	13.4	14.6	24	0	24

[a] Tested at a strain rate of 1.65×10^{-7} s^{-1} in simulated BWR water that contains ≈8 ppm DO at 288°C.

Table 7. *Correlation of SSRT test results and SEM fractography of nonirradiated control specimens of model stainless steel alloys with composition (in wt.%)*

Alloy ID	Ni	Si	P	S	Mn	C	N	Cr	Mo/Nb	O (wppm)	Remark	YS (MPa)	UTS (MPa)	UE (%)	TE (%)	TGSCC (%)	IGSCC (%)	TG+IGSCC (%)
L23	12.04	0.68	0.030	0.047	0.96	0.043	0.092	17.30	Nb 1.06	93	CP 348	332	480	15.6	17.0	15	0	15
L7	10.60	0.18	0.040	0.038	1.02	0.007	0.111	15.40	-	274	High O; Low Si, C	195	370	5.7	7.2	20	0	20
L14	7.93	1.49	0.080	0.002	1.76	0.107	0.028	15.00	-	45	High Si, P, C; Low S, N	240	474	41.8	44.2	0	0	0
L17	8.00	0.66	0.090	0.009	0.48	0.061	0.078	15.30	-	90	High P; Low S	189	412	11.6	13.3	60	0	60
L6	10.00	1.90	0.020	0.005	1.13	0.096	0.087	17.10	-	58	High Si, C, Cr; Low S	227	545	43.0	44.5	0	0	0
L27	10.30	0.96	0.040	0.002	0.97	0.057	0.019	15.30	Mo 2.01	-	CP 316 ; B = 0.030	298	483	20.6	22.9	0	0	0
L26	8.09	0.79	0.004	0.002	0.91	0.070	0.089	17.20	-	80	Low P, S	184	596	38.2	40.2	0	0	0
L2	10.50	0.82	0.080	0.034	1.58	0.074	0.102	17.02	-	66	High P, S, Mn, N	193	348	6.6	7.8	57	0	57
L25	8.93	0.92	0.020	0.008	1.54	0.019	0.095	17.20	-	85	B ≈ 0.010	184	458	25.5	27.0	0	0	0
L15	8.00	1.82	0.010	0.013	1.07	0.020	0.085	17.80	-	110	High N; Low C	218	512	36.7	37.9	0	0	0
L24	12.30	0.03	0.007	0.005	0.48	0.031	0.002	16.90	Nb 1.72	-	HP 348	352	461	10.4	12.3	10	0	10
C1	8.12	0.50	0.038	0.002	1.00	0.060	0.060	18.11	-	-	Low S, CP 304	179	498	49.4	51.7	0	0	0
C19	8.08	0.45	0.031	0.003	0.99	0.060	0.070	18.21	-	-	Low S, CP 304	178	501	47.4	49.2	0	0	0
C9	8.75	0.39	0.013	0.013	1.72	0.062	0.065	18.48	-	-	Low Si, High Mn	178	408	17.4	19.4	32	0	32

[a] CP = commercial purity, HP = high purity.

Table 8. *Correlation of SSRT test results and SEM fractography of model stainless steel alloys, irradiated to a fluence of ≈0.45×10^{-21}n cm^{-2} in helium in the Halden reactor, with alloy composition (in wt.%)*

Alloy ID	Ni	Si	P	S	Mn	C	N	Cr	Mo/Nb	O (wppm)	Remark	YS (MPa)	UTS (MPa)	UE (%)	TE (%)	TGSCC (%)	IGSCC (%)	TG+IGSCC (%)
C1	8.12	0.50	0.038	0.002	1.00	0.060	0.060	18.11	-	-	Low S, CP 304	490	680	13.4	16.6	4	0	4
L5	9.66	0.90	0.113	0.028	0.47	0.006	0.033	21.00	-	-	High P, Cr; Low Si, C	513	539	29.5	32.7	2	2	4
L22	13.30	0.24	0.015	0.004	0.40	0.003	0.001	16.10	Mo 2.04	-	HP 316L	360	596	6.6	9.4	50	15	65
C3	8.91	0.46	0.019	0.004	1.81	0.016	0.083	18.55	-	-	CP 304L	338	491	27.7	31.6	5	0	5
C16	12.90	0.38	0.014	0.002	1.66	0.020	0.011	16.92	-	-	High Ni; Low S, N	370	527	17.6	20.6	2	0	2
L4	10.20	0.94	0.031	0.010	1.75	0.110	0.002	15.80	-	-	High Ni, Mn, C; Low N	367	542	19.7	22.3	38	0	38
L18	8.13	0.14	0.016	0.033	1.13	0.080	0.001	18.00	-	-	Low Si, N	503	572	6.3	8.8	54	0	54
C10	8.13	0.55	0.033	0.002	1.00	0.060	0.086	18.19	-	-	Low S, CP 304	523	640	17.4	18.9	6	0	6
C21	10.24	0.51	0.034	0.001	1.19	0.060	0.020	16.28	Mo 2.08	-	CP 316	480	620	15.9	19.4	4	0	4
L11	8.15	0.47	0.097	0.009	1.02	0.014	0.004	17.40	-	-	High P; Low C, S, N, Si	487	599	2.3	3.8	62	0	62
L13	8.18	1.18	0.027	0.022	0.36	0.026	0.001	17.40	-	-	High Si; Low Mn, C, N	248	461	22.1	24.8	8	0	8
L20	8.91	0.17	0.010	0.004	0.41	0.002	0.002	18.10	-	-	HP 304L	454	552	2.9	5.1	32	2	34
C19	8.08	0.45	0.031	0.003	0.99	0.060	0.070	18.21	-	-	Low S, CP 304	554	682	10.5	14.7	7	0	7
C9	8.75	0.39	0.013	0.013	1.72	0.062	0.065	18.48	-	-	Low Si; High Mn	522	607	13.4	14.6	24	0	24

[a] CP = commercial purity, HP = high purity.

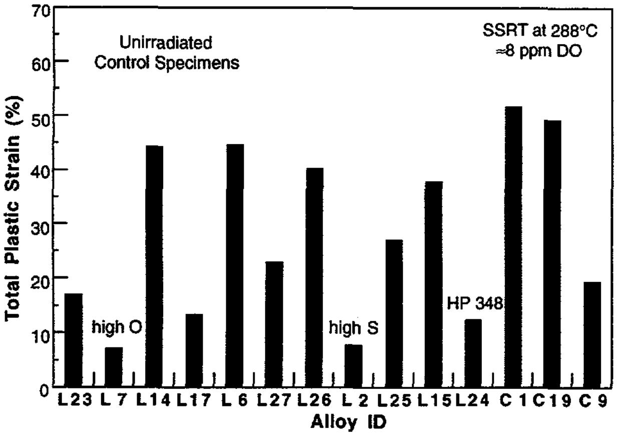

Figure 26.
Total elongation of nonirradiated control specimens of model stainless steel alloys tested at 288°C in simulated BWR water containing ≈8 ppm DO

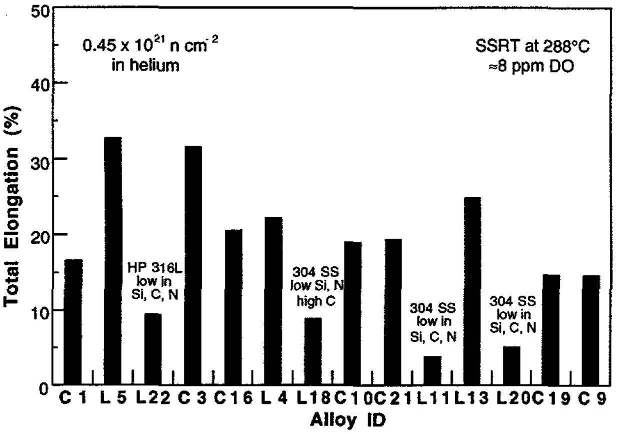

Figure 27.
Total elongation of model stainless steel alloys irradiated in helium in Halden reactor to a fluence of ≈0.45 x 10^{21} n·cm^{-2} (E >1 MeV) and tested at 288°C in simulated BWR water containing ≈8 ppm DO

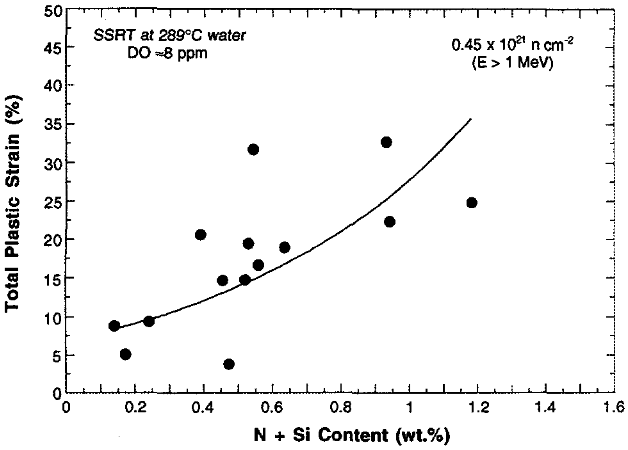

Figure 28.
Total elongation versus combined nitrogen and silicon contents of model stainless steel alloys irradiated in helium in Halden reactor to a fluence of ≈0.45 x 10^{21} n·cm^{-2} (E >1 MeV) and tested at 288°C in simulated BWR water containing ≈8 ppm DO

susceptibility to TGSCC at low fluence. Therefore, it is desirable to avoid an alloy that contains <0.01 wt.% nitrogen and <0.5 wt.% silicon. Higher silicon content appears to be conducive to less irradiation-induced hardening (Fig. 31), lower density of Frank loops, lower stacking fault energy, and lower susceptibility to TGSCC and IGSCC under irradiation.

Probably because of the relatively low fluence level of ≈0.45 x 10^{21} n·cm^{-2} (E >1 MeV), only Heat L22 (high-purity Type 316L) exhibited significant susceptibility to IGSCC (Fig. 32). Specimens irradiated to a higher fluence of ≈1.2 x 10^{21} n·cm^{-2} (E >1 MeV), obtained recently from the Halden reactor, are currently being prepared for SSRT and crack growth rate (CGR)

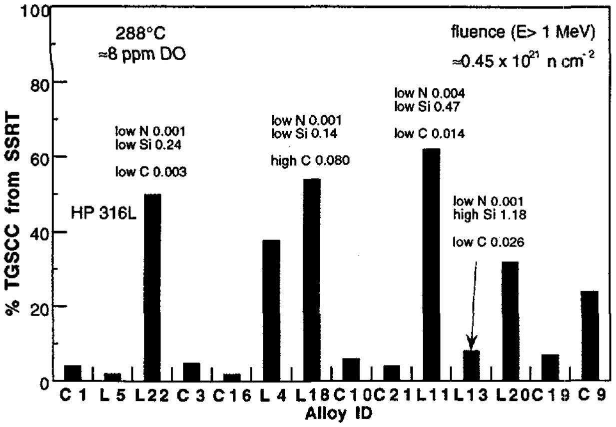

Figure 29.
Percent TGSCC of model stainless steel alloys irradiated in helium in Halden reactor to a fluence of ≈0.45 x 10^{21} n·cm^{-2} (E >1 MeV) and tested at 288°C in simulated BWR water containing ≈8 ppm DO

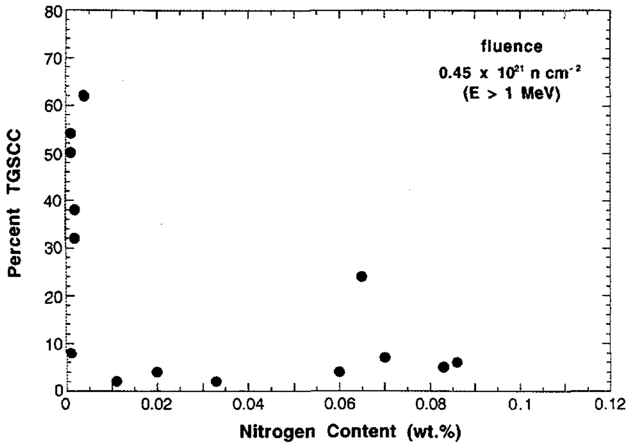

Figure 30.
Percent TGSCC versus nitrogen content of model stainless steel alloys irradiated in helium in Halden reactor to a fluence of ≈0.45 x 10^{21} n·cm^{-2} (E >1 MeV) and tested at 288°C in simulated BWR water containing ≈8 ppm DO

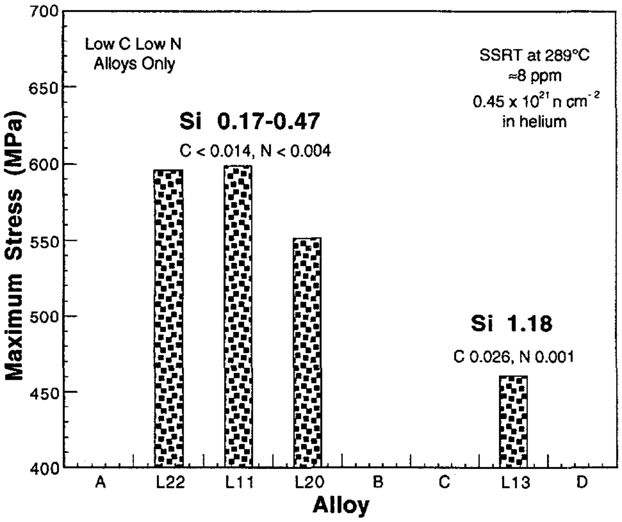

Figure 31.
Effect of silicon on maximum stress of model stainless steel alloys that contain low carbon (< 0.03 wt.%) and low nitrogen (<0.004 wt.%) and were irradiated in helium in Halden reactor to a fluence of ≈0.45 x 10^{21} n·cm^{-2} (E >1 MeV). Higher silicon content is conducive to lower strength and lower susceptibility to IASCC in simulated BWR water containing ≈8 ppm DO.

tests. We expect most of the heats to exhibit significant susceptibility to IGSCC at this fluence level. In general, high-purity heats of Type 304, 316, or 348 SS exhibit lower ductility in water and higher susceptibility to IGSCC or TGSCC. Therefore, it is desirable to avoid core internal components fabricated from high-purity heats as well as alloys that contain high oxygen (>150 wppm) or high sulfur (>300 wppm).

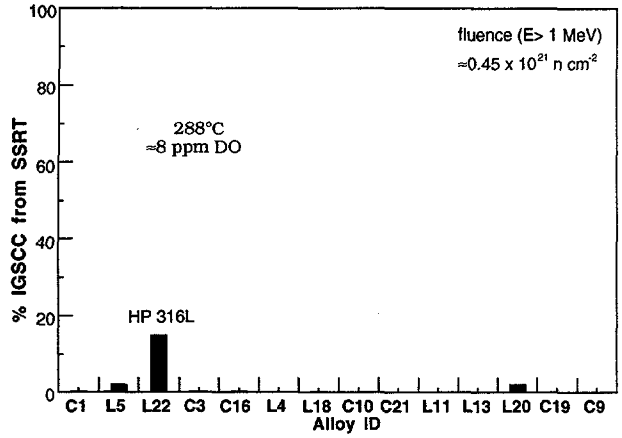

Figure 32.
Percent IGSCC of model stainless steel alloys irradiated in helium in Halden reactor to a fluence of ≈0.45 x 10^{21} n·cm^{-2} (E >1 MeV) and tested at 288°C in simulated BWR water containing ≈8 ppm DO

3.2 Structure and Properties of Core Shroud Welds
(H. M. Chung, J.-H. Park, J. E. Sanecki, and N. J. Zaluzec)

Failure of welded core internal components fabricated from Type 304 SSs has increased significantly in BWRs. In recent years, incidents of cracking in core shrouds fabricated from low-carbon Type 304L SS have also increased. Although BWR core shrouds are subject to relatively low neutron fluence, many vertical and horizontal welds crack by the time they accumulate relatively low fluences of ≈2 x 10^{19} to ≈5 x 10^{20} n·cm^{-2}. The HAZs of some core shroud welds are known to have cracked even at very low fluences, and some cracks were observed even in base metal. At these low fluences, nonwelded base-metal components fabricated from Type 304 and 304L SSs would not be considered susceptible to IASCC, which occurs after a threshold fluence of ≈5 x 10^{20} n·cm^{-2}. Partly because of this, most cases of core shroud cracking have been attributed to classical IGSCC of thermally sensitized SS. As in sensitized base metals, a sufficient degree of thermal sensitization has been assumed to occur in the HAZ of a core shroud during the welding. However, the extensive cracking observed in the core shroud HAZs fabricated from Type 304L SS and the cracks in base metal are difficult to understand on the basis of classical IGSCC because thermal sensitization by grain-boundary carbide precipitation would not be expected to occur in these materials.

Most large core-internal components, such as BWR core shrouds are welded by shielded-metal-arc (SMA) or submerged-arc (SA) welds, in which Type 308 SS filler and fluoride-containing flux compound are used in the presence of air to join thick plates by arc-melting. To better understand core shroud cracking, microstructural characteristics of Type 304 and 304L SS core shrouds, irradiated and cracked in three BWRs, as well as nonirradiated simulated SMA and gas-tungsten-arc (GTA) welds of Type 304, 304L, and 316 SSs were investigated by chemical analysis, scanning electron microscopy (SEM), Auger electron spectroscopy (AES), secondary-ion mass spectroscopy (SIMS), and field-emission-gun advanced analytical electron microscopy (FEG-AAEM).

3.2.1 Studies on Simulated Core Shroud Welds

The SMA welding procedure makes use of welding electrode rods that are coated with a welding flux (e.g., ASME Section II SFA 5.4 E-308-16 welding electrode). The procedure is shown schematically in Fig. 33. In SA welding, a similar flux is used in powder form to cover

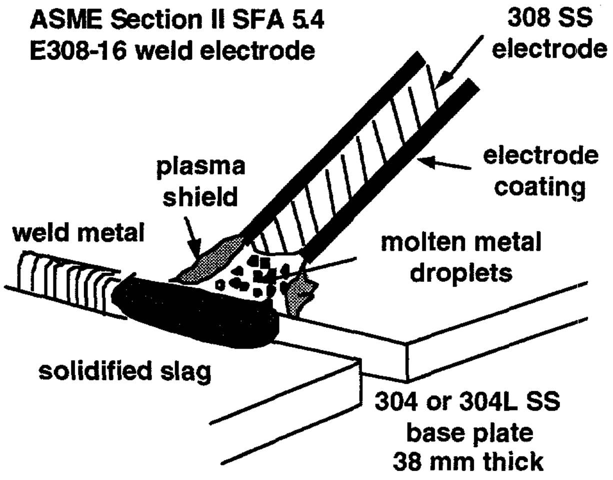

Figure 33.
Schematic illustration of shielded-metal-arc welding procedure

the base metal plate to be welded. Consequently, similar contamination by impurities can occur in the weld and heat-affected zones (WZ and HAZ) in both types of welds, and the microchemistry and microstructure of these regions can differ significantly from the base metal; factors that can influence SCC behavior. For BWR core shrouds, the vertical welds are usually welded by an SA procedure, whereas most of the horizontal welds are welded by an SMA procedure.

In a continuation of the previous investigation,[62,63] the structure and properties of laboratory-produced core-shroud-type welds were investigated further in this reporting period. Weldments of five commercial heats of Types 304, 304L, and 316 were investigated (Table 9). The composition of the welding electrode used in the SMA procedure is given in Table 10.

3.2.1.1 Impurity Contamination Characterized by Secondary Ion Mass Spectroscopy

Oxygen, fluorine, and other impurity distributions were analyzed by SIMS on the SMA and gas-tungsten-arc (GTA) welds of a Type 304 SS, Heat C1 and the SMA weld of the Type 304L SS, Heat C3. Results of mapping in color of the secondary ions of oxygen, fluorine, calcium, carbon, and nitrogen from the weld zone (WZ) and HAZ were obtained. Black, red, orange, and white in the map correspond, respectively, to regions of proportionately higher ion population; black corresponds to no or negligible ions detected. Because of difficulty in reproducing color maps in this report, the results are shown in black and white in Fig. 34. However, the true distributions of the impurities are not as straightforward from black and white maps as from color maps. The results of the SIMS analyses can be summarized as follows:

(a) Oxygen and fluorine contamination was significant in all SMA welds. Oxygen contamination was significantly more pronounced in the WZ than in the HAZ.

(b) In contrast to SMA welds, fluorine contamination was negligible and oxygen contamination was less significant in GTA welds.

Table 9. *Composition (in wt.%) of commercial heats of Type 304, 304L, and 316 SSs selected to investigate weld properties*

ANL Heat ID	Steel Type	Thickness (mm)	Weld Type Investigated	Ni	Si	P	S	Mn	C	N	Cr	Mo
C1	304	12.7	SMA, GTA	8.12	0.50	0.038	0.002	1.00	0.060	0.060	18.11	–
C3	304L	12.7	SMA, GTA	8.91	0.46	0.019	0.004	1.81	0.016	0.083	18.55	–
C21	316	12.7	SMA, GTA	10.24	0.51	0.034	0.001	1.19	0.060	0.020	16.28	2.08
19611	304	38	SMA	8.36	0.48	0.024	0.018	1.69	0.060	0.086	18.35	0.14
M9284	304	38	SMA, GTA	8.12	0.45	0.021	0.011	1.47	0.050	0.055	18.49	0.28

Table 10. *Composition (in wt.%) of E-308-16 welding electrode for SMA welding*

Fe	Cr	Ni	Mn	Si	Mo	C	Cu	Nb	V	$CaCO_3$	CaF_2	SiO_2	TiO_2	Al_2O_3	Silicate
67.5	20.5	9.7	1.17	0.52	0.39	0.052	0.1	0.02	0.07	2-8	1-10	1-8	1-12	0-3	<5

(c) Sparsely populated oxide inclusions were present in the base metal of Type 304 SS Heat C1. These oxides were rich in fluorine, showing that the base metal of this heat of Type 304 SS contained fluorine in spherical oxide inclusions that formed during the ingot-melting process.

(d) Nitrogen and carbon contamination was insignificant in the SMA as well as in GTA welds.

(e) Significant carbide precipitation occurred in the HAZ of the GTA weld. In contrast to oxides, fluorine atoms were not enriched in the carbides, which is consistent with the results of AES analyses of BWR neutron-absorber tubes reported previously.[63]

(f) Carbide precipitation was negligible in the HAZ of the SMA weld of Type 304 SS Heat C1 (≈0.060 wt.% C) as well as in Type 304L SS Heat C3 (≈0.016 wt.% C). That is, in contrast to GTA welding, thermal sensitization did not occur during SMA welding, even in high-carbon Heat C1.

(g) Calcium-rich precipitates were present in SMA welds in the WZ and in the HAZ up to ≈0.6 mm away from the fusion line. Most of the precipitates are also rich in oxygen and fluorine. No calcium-rich precipitates were present in GTA welds.

Because calcium-rich precipitates were absent in GTA welds, they are not likely to be (Ca,Mn)S-type sulfides, which are observed in some steels;[64] they are more likely to have been produced in association with the SMA welding procedures. To confirm this, chemical composition of the calcium-rich precipitates was determined in an SEM by X-ray energy dispersive spectroscopy (XEDS). The result is shown in Fig. 35. The calcium-rich precipitates were high in oxygen, fluorine, and silicon, the same elements that are also high in the flux compound in the weld electrode coating (Table 10). The composition of the surface weld slag was similar but contained more silicon, potassium, and titanium (Fig. 35). Therefore, it is obvious that the calcium-oxyfluoride-type precipitates form by contamination during the SMA welding. After each weld pass, the weld slag pockets were removed mechanically from weld cusps by a grinding wheel, and this process may have assisted the formation of the calcium-rich precipitates by impregnating small particles of broken weld scale (see Fig. 36). The calcium-rich inclusions dissolved readily when in contact with water during either SSRT testing at 288°C or polishing at room temperature. When the specimen surface was polished in an oxalic solution, however, the inclusions did not dissolve. These observations indicate that the calcium-oxyfluoride-type inclusions are soluble in reactor coolants and hence could accelerate release of fluorine ions into the crack tip.

3.2.1.2 Thermal Sensitization Characterized by Transmission Electron Microscopy

The absence of carbide precipitates in SIMS maps of the HAZ of an SMA weld of high-carbon Type 304 SS, Heat C1 (≈0.060 wt.% C) was a major surprise, because in contrast to a GTA weld, the SMA weld of Type 304 SS would not exhibit thermal sensitization via grain-boundary carbide precipitation. Therefore, extensive characterization of grain-boundary carbide precipitation was conducted by TEM to investigate more directly the relative behavior of thermal sensitization in the GTA and SMA welds of the Type 304 SSs listed in Table 9.

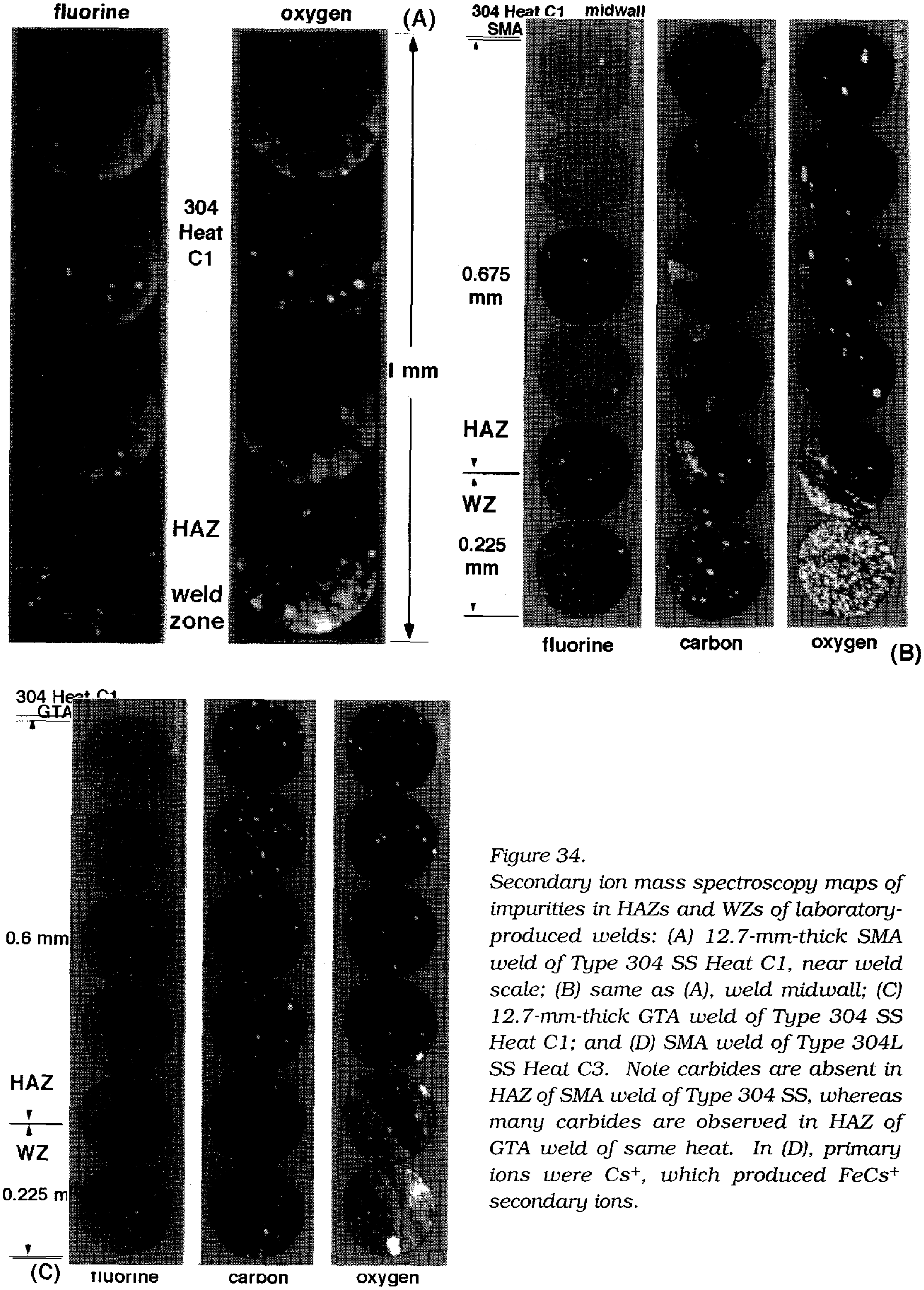

Figure 34.

Secondary ion mass spectroscopy maps of impurities in HAZs and WZs of laboratory-produced welds: (A) 12.7-mm-thick SMA weld of Type 304 SS Heat C1, near weld scale; (B) same as (A), weld midwall; (C) 12.7-mm-thick GTA weld of Type 304 SS Heat C1; and (D) SMA weld of Type 304L SS Heat C3. Note carbides are absent in HAZ of SMA weld of Type 304 SS, whereas many carbides are observed in HAZ of GTA weld of same heat. In (D), primary ions were Cs^+, which produced $FeCs^+$ secondary ions.

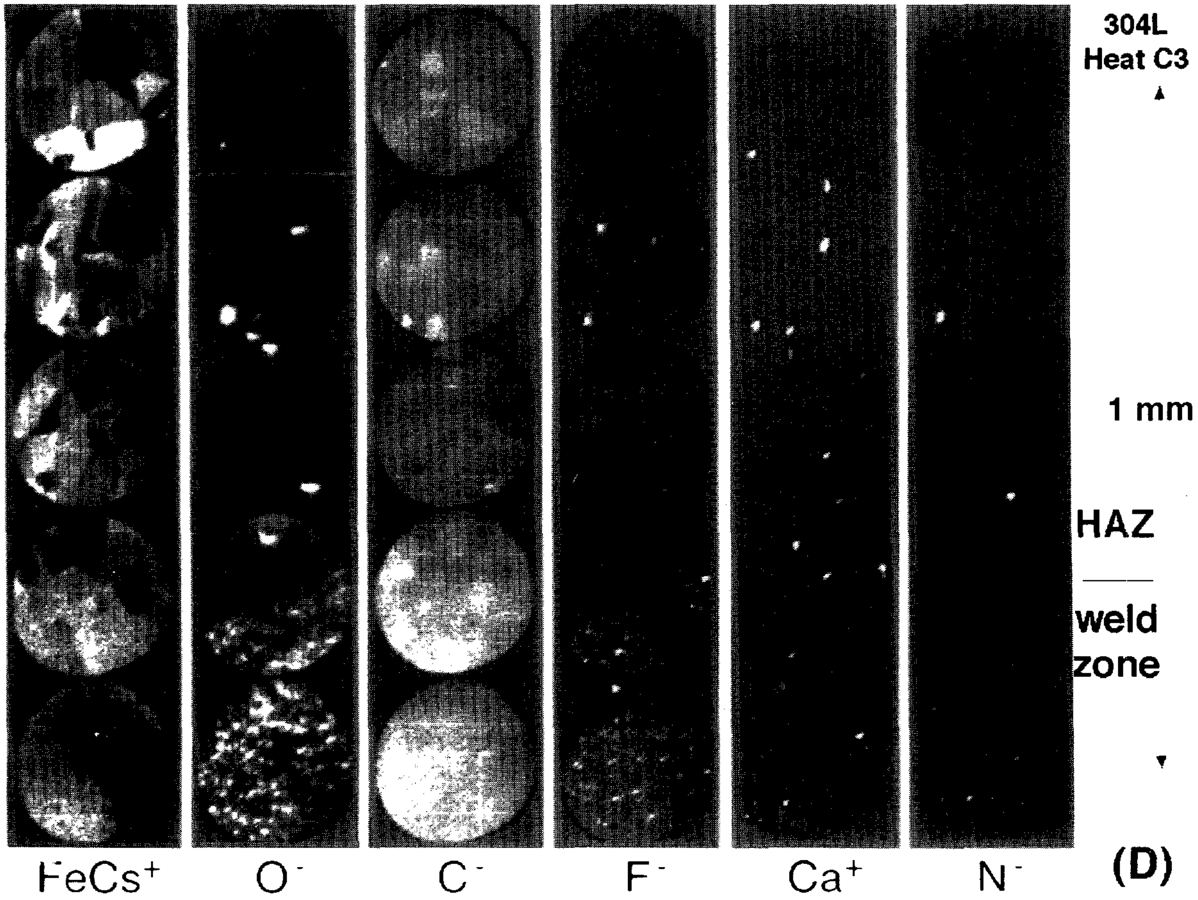

Figure 34. (Cont'd)

Disks for TEM analysis were punched from the HAZ and base metal, as illustrated in Fig. 36.

Grain-boundary carbides were characterized by the usual combination of bright-field imaging, tilting, selected-area-diffraction (SAD) analysis, and dark-field imaging. As expected, many $M_{23}C_6$ carbides, 70-150 mm in size, were observed on the grain boundaries of HAZ of the GTA welds. This is shown in Fig. 37, which contains dark-field images of grain-boundary carbides and a characteristic diffraction pattern with reflections from the matrix and the $M_{23}C_6$ carbides.

In contrast, carbides were absent on grain boundaries of the HAZ of the SMA weld, regardless of the location of the thin-foil TEM specimens relative to the free surface or weld fusion line. A typical example of grain boundaries in the HAZ of the SMA weld of high-carbon (≈0.06 wt.%) Type 304 SS, Heat C1, is shown in Fig. 38. Carbides were also absent on grain boundaries of the HAZs of the SMA welds of the Type 316 SS, Heat C21 (≈0.060 wt.%C) and the low-carbon (≈0.016 wt.%) Type 304L SS, Heat C3. This shows that for our heats (CP Type 304 SS, Heat C1 and Type 316 SS, Heat C21) and plate thickness (12.7 mm), susceptibility of the HAZ to thermal sensitization is negligible in SMA welds, which is in major contrast to the behavior of GTA welds.

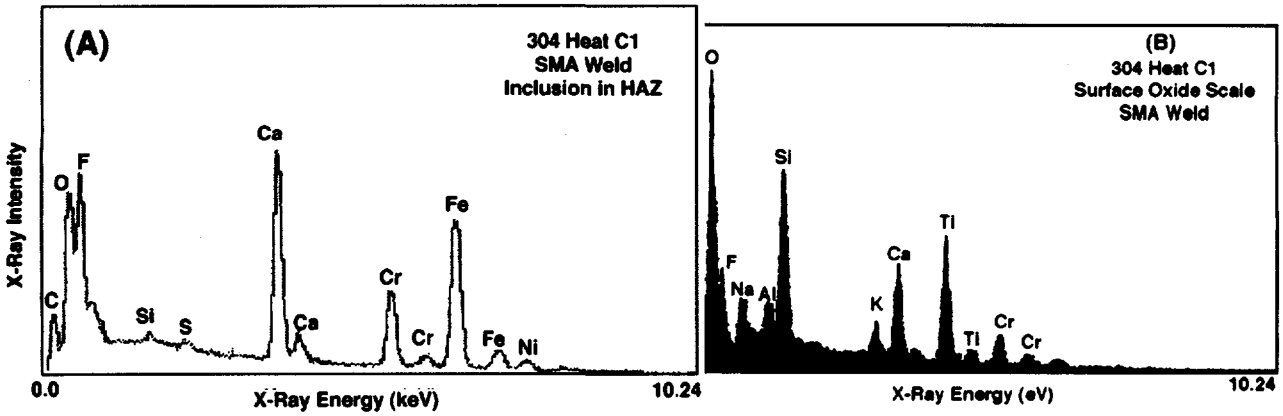

Figure 35. Composition of (A) calcium-rich precipitates in HAZ and (B) surface weld scale of nonirradiated SMA weld of Type 304 SS Heat C1 determined by X-ray energy-dispersive spectroscopy in SEM

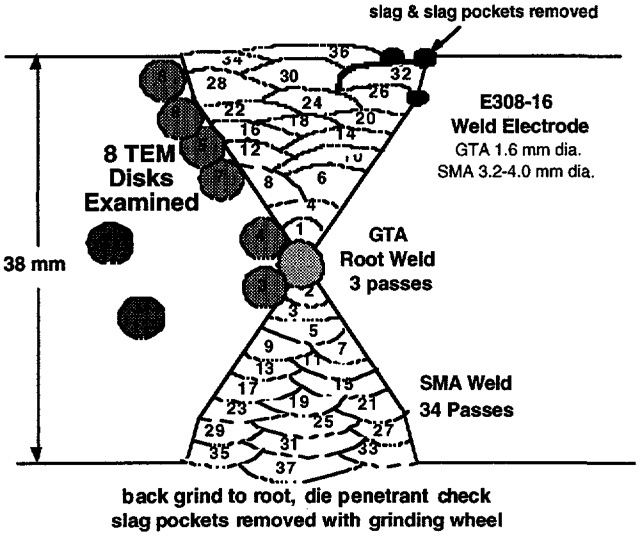

*Figure 36.
Schematic diagram of weld passes and TEM disk locations of a 38-mm-thick plate of Type 304 SS, Heat 19611. Weld slag and slag pockets were removed after each pass.*

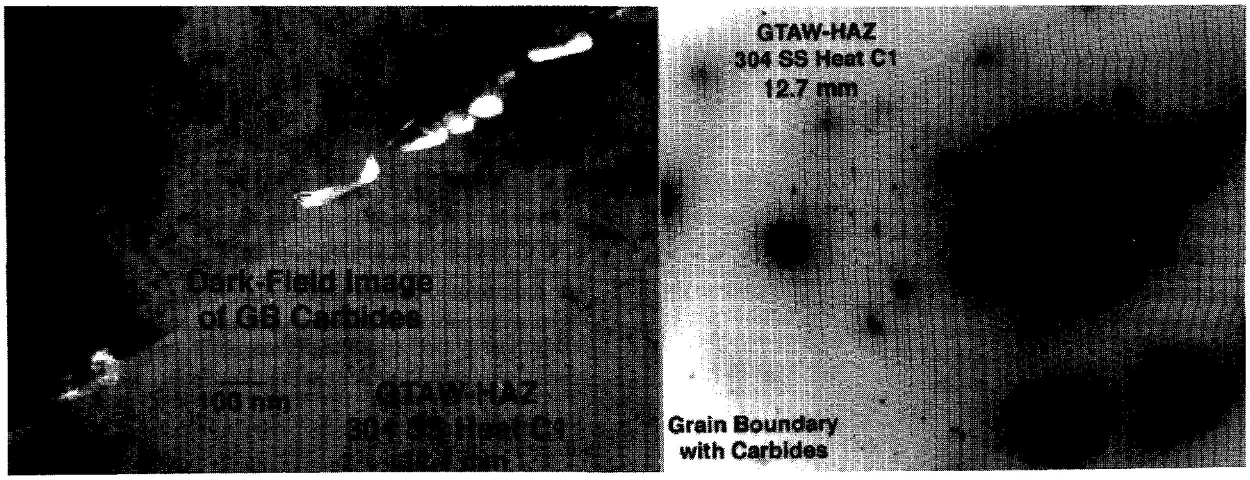

Figure 37. Dark-field image (left) and characteristic selected-area diffraction pattern (right) of $M_{23}C_6$ carbides from a grain boundary of heat-affected zone of nonirradiated GTA weld of Type 304 SS, Heat C1, showing significant thermal sensitization

Thermal sensitization should be influenced by many factors. Besides the smaller number of weld passes (8 SMA passes for the 12.7-mm-thick plates), we believe the higher molybdenum and oxygen contents in the HAZ of the SMA weld are conducive to less grain-boundary carbide precipitation. An actual core shroud weld, e.g., a 38-mm-thick horizontal weld H4, typically receives 18 or more weld passes, hence the total time at temperatures in the sensitization range will be significantly greater than for our SMA weld. Therefore, grain-boundary carbide precipitation could be more significant. In the meantime, more weld passes mean more exposure to weld fumes and hence more contamination by oxygen and fluorine.

To investigate the effects of number of weld passes and plate thickness, SMA welds were prepared from 38-mm-thick plates of two additional heats of Type 304 SS (Heat 19611, ≈0.06 wt.% C and Heat M9284, ≈0.050 wt.% C). As shown in Fig. 36, the SMA welds were prepared from modified double-V joints. Three GTA weld passes were needed to establish a good root weld. Flaws in the root weld, revealed by die-penetration checks, were ground out, and 37 SMA weld passes were applied subsequently to complete the job. Between each SMA weld pass, the weld scale was broken loose by a small hammer and slag particles were removed by a wire brush. Slag pockets left at weld pass cusps were ground out with a grinding wheel. These procedures are typical of a core shroud weld prepared by SMA.

Consistent with the observation made on the 12.7-mm-thick SMA welds, no grain-boundary carbides were detected in any of the TEM disks (see Fig. 36) from the HAZs of the 38-mm-thick SMA welds of the Type 304 SS, Heat 19611 or Heat M9284. An example of "clean" (i.e., carbide-free) grain boundaries typical of the HAZ of the SMA weld of Heat 19611 is shown in Fig. 38. Neither bright-field images nor diffraction spots from $M_{23}C_6$ precipitates, characteristic of a sensitized GTA weld HAZ, were present on more than 25 grain boundaries examined, and hence, no dark-field images could be obtained. This shows that grain-boundary carbide precipitation was absent in the SMA weld of this heat. Dark-field imaging accompanied by SAD indexing constitutes conclusive evidence of grain-boundary carbide precipitation. In contrast to the SMA weld of Type 304 SS, Heat M9284, grain-boundary carbides were conclusively identified in the HAZ of the 38-mm-thick GTA weld of the same heat. This is consistent with the observations made on the 12.7-mm-thick GTA welds of Type 304 SS, Heat C1 and Type 316 SS, Heat C21.

Results of the TEM characterization of thermal sensitization via grain-boundary carbide precipitation in the nonirradiated SMA and GTA welds are summarized in Table 11. For Type 304 and 316 SS heats listed in the table, grain-boundary carbides were observed in the HAZs of all GTA welds, whereas grain-boundary carbides were not observed in the HAZs of any of the SMA welds. In particular, the absence of thermal sensitization in the HAZ of the 38-mm-thick SMA welds of Type 304 SS is surprising. It is possible that high oxygen contamination associated with SMA welding suppresses grain-boundary carbide precipitation because the affinity of chromium to oxygen atoms is stronger than the affinity of chromium to carbon atoms.

3.2.2 Studies on Type 304 and 304L SS BWR Core Shrouds

In addition to the nonirradiated laboratory-produced welds described above, boat samples obtained from two core shrouds were examined; one of Type 304L SS and another of Type 304 SS, from BWR-C and BWR-D, respectively. Composition and accumulated fast neutron (E >1 MeV) fluence of the core shrouds are given in Table 12.

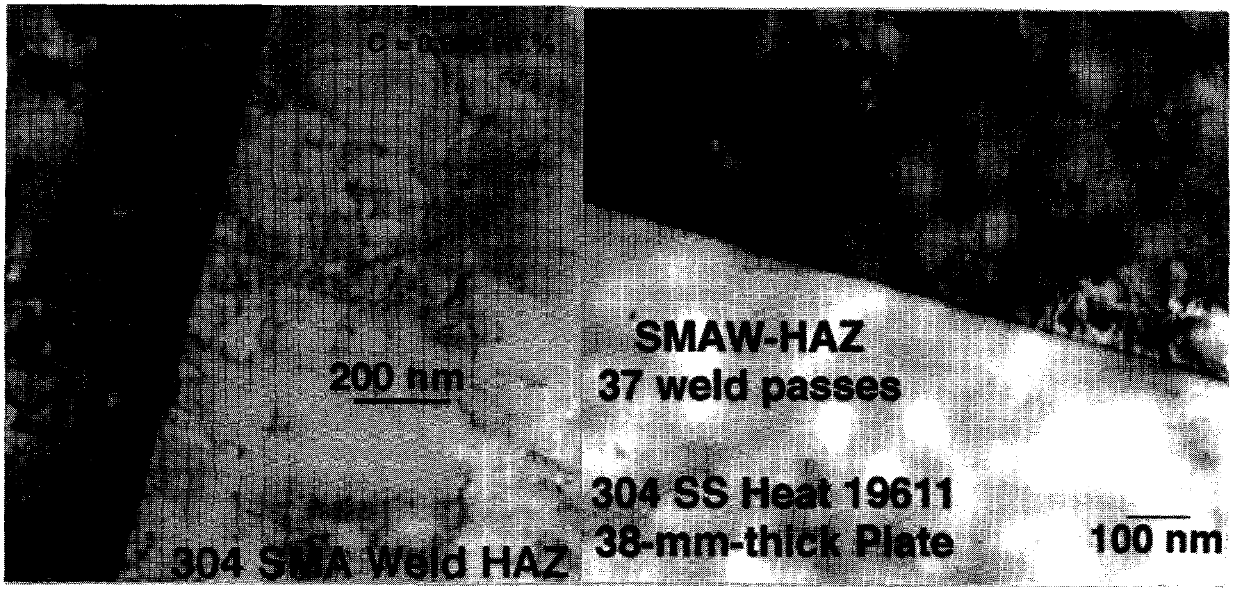

Figure 38. Bright-field images of grain boundaries of HAZs of nonirradiated SMA welds of Type 304 SS, Heat C1 (left, 12.7-mm-thick plate, ≈0.060 wt.% C) and Heat 19611 (right, 38-mm-thick plate, ≈0.060 wt.% C). Note absence of carbide precipitates.

Table 11. Summary of TEM characterization of thermal sensitization in HAZs of SMA and GTA welds of Type 304 and 316 SS plates

Steel Type	ANL Heat ID	Fluence ($n \cdot cm^{-2}$)	Base Metal Carbon (wt.%)	Plate Thickness (mm)	Weld Type	GB Carbides Detected by TEM	Carbides Detected by SIMS
304	C1	0	0.060	12.7	SMA	none	none
304	C1	0	0.060	12.7	GTA	many	many
304L	C3	0	0.016	12.7	SMA	none	none
304L	C3	0	0.016	12.7	GTA	none	–
316	C21	0	0.060	12.7	SMA	none	–
316	C21	0	0.060	12.7	GTA	some	–
304	19611	0	0.060	38	SMA	none	–
304	M9284	0	0.050	38	SMA	none	–
304	M9284	0	0.050	38	GTA	many	–
304L core shroud	BWR-C	4.6×10^{19}	0.027	38	–	none	–
304 core shroud	BWR-D	10×10^{19}	0.063	50.8	–	none	–

Table 12. Composition and fast-neutron fluence of Type 304L and 304 SS core shroud weld boat samples

ANL	Steel	Composition (wt.%)									Source	Fluence
Specimen ID	Type	Cr	Ni	Mn	C	Nb	Mo	Si	P	S	BWR	(10^{19} $n \cdot cm^{-2}$)
507-B[a]	304L	18.90	9.36	1.82	0.027	0.064	0.568	0.483	0.024	0.0018	BWR-C	4.6
D3-H5-324	304	-	-	-	0.063[b]	-	-	-	-	-	BWR-D	10

[a] Composition determined for irradiated boat sample by electron probe microanalysis.
[b] Carbon content of nonirradiated plate.

3.2.2.1 Microstructural Analyses of Type 304L SS Core Shroud

Microstructures of two boat samples from the field-cracked BWR-C core shroud weld, irradiated to a fluence of 4.6×10^{19} $n \cdot cm^{-2}$ (E >1 MeV), were characterized by SEM, FEG-AAEM, and AES. Fracture occurred in the HAZ of the Type 304L SS weld during service. A document on the welding type was not available. The fracture surface of the field crack was badly corroded because of exposure to the reactor coolant. However, regions of clean fracture surface morphology could be found near the tight crack tip. The fracture surface morphology, shown in Fig. 39, is not a typical IG fracture but appears to contain a significant fraction of ductile tearing in addition to IG separation.

Carbides, chromium depletion, or a martensite thin film were not detected on grain boundaries of HAZ specimens that were characterized by a Vacuum Generator Co. Model HB603 FEG-AAEM (see Figs. 40 and 41). Therefore, in terms of classical IGSCC, the Type 304L SS weld HAZ was not thermally sensitized, and grain-boundary chromium depletion (by either a thermal or irradiation-induced process) was negligible. However, dense line dislocations were present in the HAZ, apparently produced during welding. A similar microstructure that contains dense dislocations is also visible in the HAZ of the nonirradiated SMA weld (Fig. 38). Such dense line dislocations were absent in the base metal of the core shroud and the laboratory-produced SMA weld specimens.

Notched AES specimens prepared from the core shroud weld HAZ were fractured at ≈23°C in the ultrahigh vacuum environment of the scanning Auger microscope. A typical example of the clean in-situ fracture surface morphology is shown in Fig. 42. The figure shows IG fracture surface and many fine particles, ≈0.1-2 mm in size, on the grain boundaries. The particles were found to be essentially chromium oxides (see the AES spectrum shown in the left inset, Fig. 43). The area AES signal, acquired from a square region (≈10 x 10 mm) of an IG fracture surface, showed an unusually high oxygen peak, as well as weak signals of sulfur, molybdenum, and fluorine at 625 eV.

A selected region on the grain-boundary surface was then sputtered with argon ions to conduct depth-profiling analysis. When the area was sputtered with argon ions, the height of the oxygen peak did not decrease appreciably up to ≈100 nm from the IG fracture surface. This behavior is in sharp contrast to the sputter characteristics of oxygen on the IG or ductile fracture surfaces of BWR neutron-absorber tube or control-blade sheath specimens. In the latter materials, the typical signal of the oxygen layer that is chemisorbed as a result of contamination from the vacuum environment of the Auger microscope, reaches a lower asymptotic level after sputtering to only ≈4 nm. This asymptotic level corresponds to the oxygen content of the base metal. These observations show that oxygen contamination in the BWR-C core shroud HAZ was very significant. A significant decrease in the intensity of fluorine-625 eV signal[65] was observed as function of sputter distance (Fig. 44), which indicates that fluorine had segregated to the grain boundary. A similar observation of grain-boundary segregation of fluorine has been reported previously for CP and HP Type 304 SS neuron-absorber tubes.[63,65]

3.2.2.2 Microstructural Analyses of Type 304 SS Core Shroud

A Type 304 SS core shroud sample that accumulated a fluence of $\approx 1 \times 10^{20}$ $n \cdot cm^{-2}$ (E >1 MeV) and had cracked during service in BWR-D has been obtained for microstructural

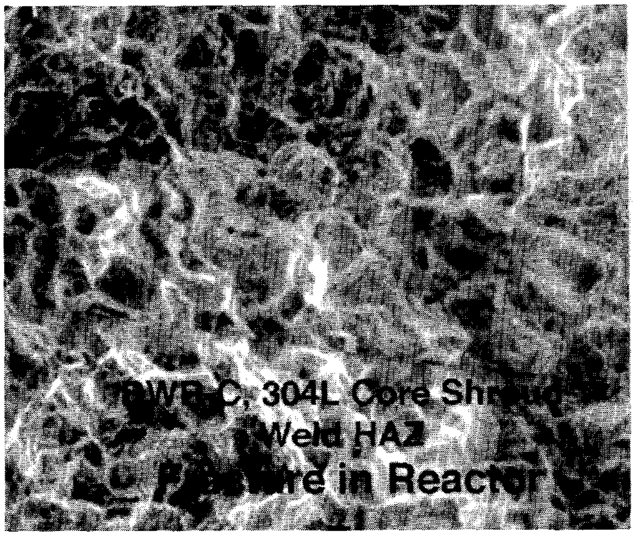

Figure 39.
SEM fracture surface morphology of Type 304L BWR-C core shroud weld. Fracture occurred in HAZ during service, fluence 0.45 x 10^{21} n·cm^{-2} (E >1 MeV).

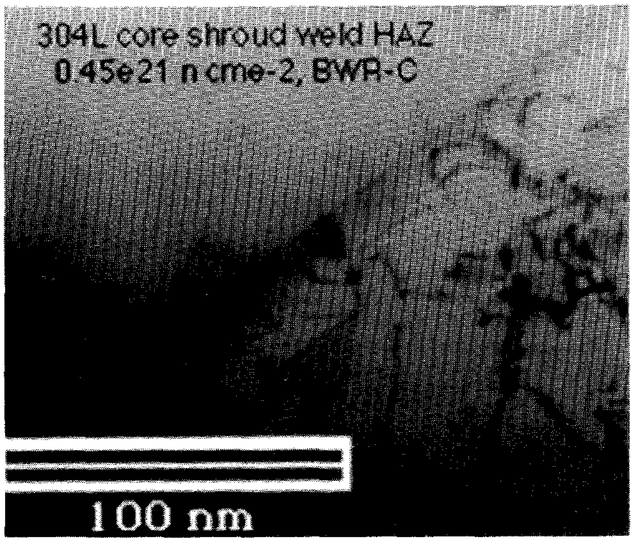

Figure 40.
Typical grain-boundary structure of HAZ of Type 304L BWR-C core shroud weld. Carbides and thin films are absent from the boundary.

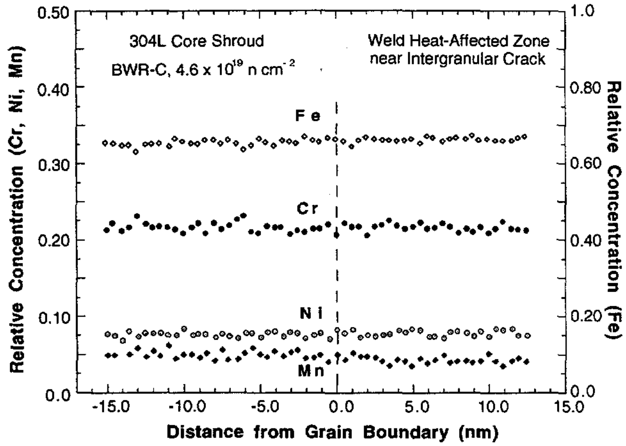

Figure 41.
Profiles of Fe, Cr, Ni, and Mn near grain boundary of HAZ of Type 304L BWR-C core shroud weld shown in Fig. 40. Grain-boundary Cr depletion is negligible.

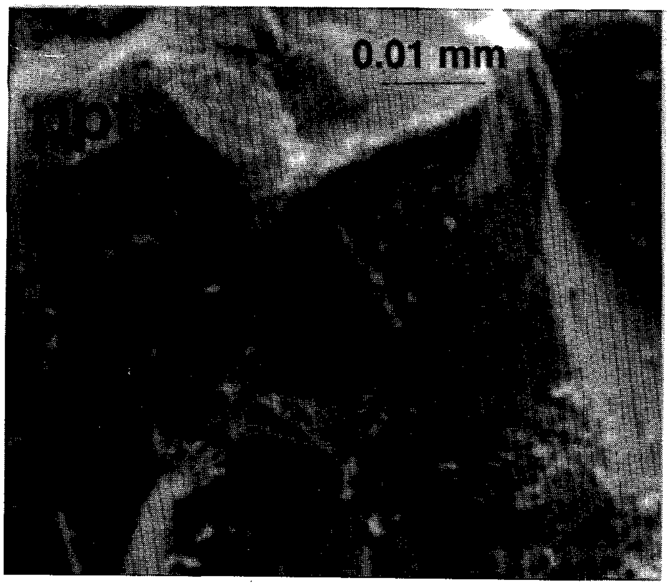

Figure 42.
AES fracture surface morphology in HAZ of Type 304L BWR-C core shroud weld, in which fracture was produced at ≈23°C in ultrahigh vacuum of scanning Auger electron microscope. Many fine oxide particles are present on the fracture surface.

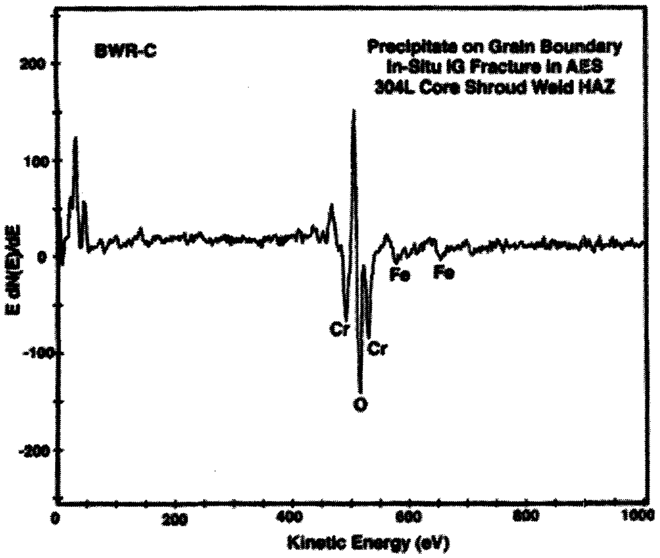

Figure 43.
AES signals from particle denoted "ppt" in Fig. 42, showing chromium oxide

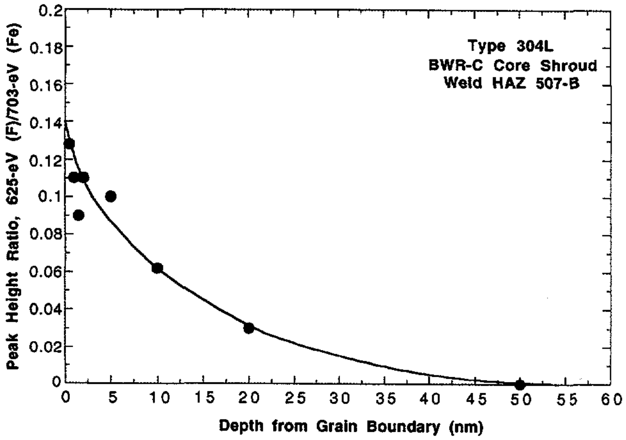

Figure 44.
Fluorine AES signal intensity as function of sputter distance from grain boundary surface in HAZ of Type 304L BWR-C core shroud weld

analysis by TEM and AES. The boat sample was sectioned from the cracked core plate support ring. Cracks in the Type 304 SS (≈0.063 wt.%C) ring were detected near the horizontal H5 weld along the entire circumference (see Fig. 45). In many later-design BWRs, the H5 weld is referred to as the H6A weld. The low-magnification optical photomicrograph in Fig. 46 shows three cracks in the boat sample; a high-magnification photomicrograph is shown in Fig. 47. Cold-worked grains are visible in the HAZ near the #1 crack, which nucleated ≈3.5 mm away from the fusion line. The other two cracks are located ≈9 and ≈14 mm away from the fusion line, apparently in the base metal.

Characterization by TEM of grain-boundary carbide precipitation and thermal sensitization was conducted on the boat sample. A total of 16 TEM disks were prepared (Fig. 46) near the cracks located in the HAZ and base metal. Of the 16 disks, 8 were jet-polished and examined by TEM. No grain-boundary carbide was observed in any of the 8 disks that were examined. A typical example of grain boundaries is shown in Fig. 48. Some disks exhibited a light-contrasted feature which is an indication of localized thinning during the jet-polishing procedure in association with significant inhomogeneity of local chemical composition. Because of the absence of grain-boundary carbide precipitation in the HAZ near the cracks, it is difficult to explain the cracking in the Type 304 SS weld on the basis of classical thermal sensitization.

3.2.2.3 Model of BWR Core Shroud Cracking

Microstructural characteristics of the Type 304L and 304 SS core shrouds weld HAZ can be summarized by (a) absence of carbides on or near grain boundaries, (b) absence of martensite thin film on grain boundaries, (c) no grain-boundary chromium depletion, (d) dense dislocations, (e) significant oxygen contamination, (f) significant fluorine contamination, and (g) fluorine segregation to grain boundaries. Results obtained from the microstructural and microchemical analyses of the simulated nonirradiated SMA welds and irradiated core shrouds were essentially similar. Considering these observations, it is difficult to explain the core shroud weld cracking on the basis of either classical IGSCC in which thermal sensitization by grain-boundary carbide precipitation plays the key role or the grain-boundary Cr-depletion model of IASCC.

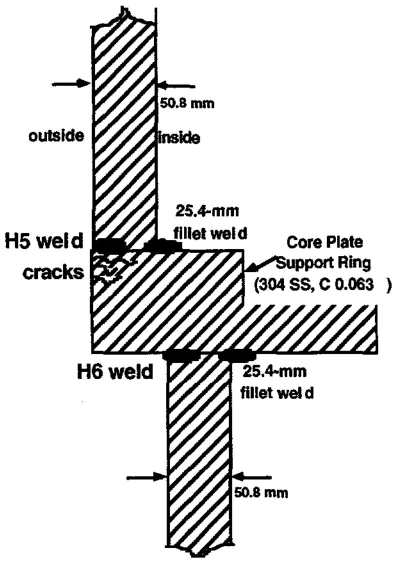

Figure 45.
Schematic diagram of H5 and H6 welds and cracked core plate support ring of BWR-D

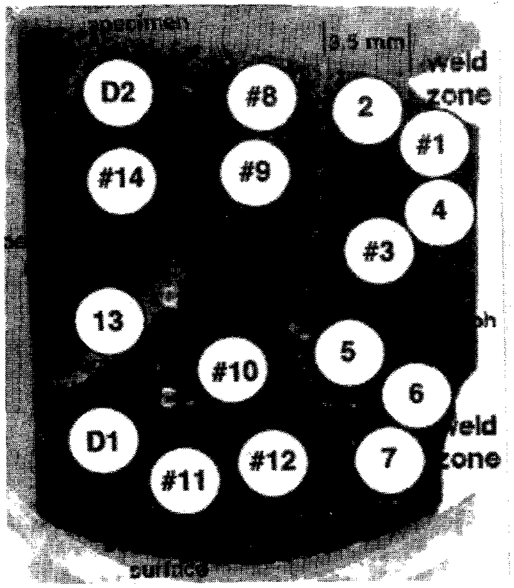

Figure 46.
Location of cracks and TEM disks in boat sample from a Type 304 SS core shroud weld from BWR-D irradiated to a fluence of ≈1 x 10^{20} *n·cm*$^{-2}$ *(E >1 MeV). Disks 1, 3, 8, 9, 10, 11, 12, and 14 were examined. No grain-boundary carbides were observed in any of the disks.*

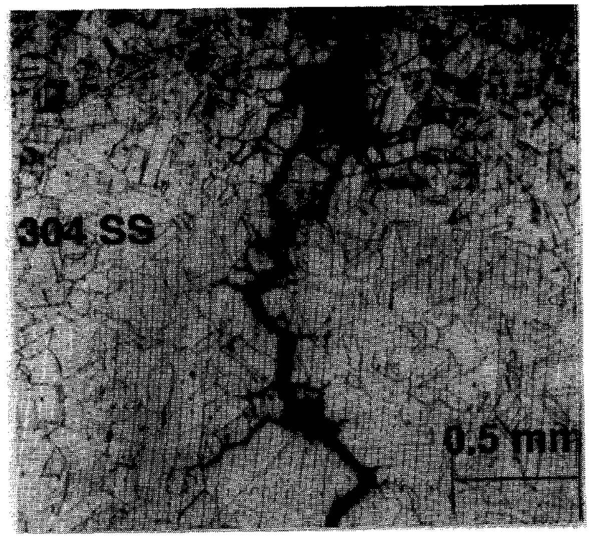

Figure 47.
Morphology of crack ≈3.5 mm from the fusion line in HAZ of Type 304 SS core shroud weld irradiated to a fluence of ≈1 x 10^{20} *n·cm*$^{-2}$ *(E >1 MeV) in BWR-D*

Figure 48.
Typical example of grain boundaries in HAZ of Type 304 SS cracked core shroud weld irradiated to a fluence of ≈1 x 10^{20} *n·cm*$^{-2}$ *(E >1 MeV) in BWR-D. Note absence of carbides on grain boundaries.*

The oxygen and fluorine contamination characteristics observed for the simulated SMA weld, BWR neutron absorber tubes,[65] control blade sheath,[65] and core shroud weld were essentially consistent. Fluorine-assisted SCC has been reported by many investigators.[66-75] The present investigation shows that significant fluorine contamination of core shroud welds occurs in association with oxygen contamination. This behavior explains well the previous reports by several investigators that weld fume contamination or the presence of weld slag strongly exacerbates the susceptibility of flux-welded steels to IGSCC.[66,69,70] The results from the previous SSRT experiments on the neutron absorber tubes[65] are also consistent with the results of the bend-beam experiments of these investigators, that is, grain-boundary chromium depletion (by either a thermal sensitization or irradiation-induced process) and high levels of oxygen and fluorine in the material are important factors that exacerbate susceptibility to IG stress corrosion cracking. In consideration of the direct association of oxygen and fluorine contamination, this type of IGSCC accelerated by material contamination by oxygen and fluorine would be appropriately termed "oxyfluorine-assisted" SCC.

One possible explanation of Type 304 and 304L SS core-shroud-weld cracking is "oxyfluorine-assisted" SCC. A model is proposed below, based on a synergism among oxygen, chromium, and fluorine. Halide ions, in particular chloride and fluoride, are well known to play catalytic roles in accelerating aqueous corrosion of iron and steels. The catalytic role has been known to be strongly influenced by the concentration of chromium ions in water.[71] The corrosion acceleration has been attributed to the orders–of–magnitude faster rate of formation of a ligand complex between Fe–halide and H_2O molecules than the rate of formation of a similar ligand complex between halide–free Fe atom and H_2O molecules. A similar effect can be postulated for relative reaction rates in forming fluorine–containing (fast reaction) and fluorine–free (slow reaction) ligand complexes of $FeF(H_2O)_5$ and $Fe(H_2O)_6$, respectively. A free fluoride ion is then released from the labile complex $FeF(H_2O)_5$ in water when H_2O replaces the fluorine atom in the complex. Then, the fluoride ion again drives the fast reaction to form another $FeF(H_2O)_5$ complex. This cycle repeats itself, leading to a classical catalytic role by fluorine. However, this reaction chain is broken when the concentration of chromium ions in crack tip water is high, because nonlabile $CrF(H_2O)_5$ is formed rapidly but remains inert in water. Therefore, fluorine remains trapped in nonlabile $CrF(H_2O)_5$ in water, preventing a catalytic role of fluorine.

When oxygen concentration is high in grain matrices and on grain boundaries, chromium and oxygen are bound chemically on the crack tip surfaces exposed to water. This prevents chromium from participating in the fast reaction

$$\text{Cr-F (F adsorbed)} + 5H_2O = [CrF(H_2O)_5]^+ + e^-. \quad (15)$$

This is in effect equivalent to grain-boundary chromium depletion, because the concentration of chromium ions dissolved in crack tip water will be low. Then, fluoride ion concentration in crack tip water will be higher and, as depicted in Fig. 49, the catalytic role of fluorine will be in full force. According to this model, a material would be more susceptible to IG cracking if (a) it was significantly contaminated by fluorine and oxygen, (b) its grain boundaries were depleted of chromium by either thermal sensitization or irradiation-induced processes, or (c) its grain matrices were hardened significantly by either irradiation or cold work. Susceptibility of core shroud welds prepared by SMA or SA procedures to "oxyfluorine-assisted" SCC will be influenced strongly by high oxygen concentration in particular, because higher oxygen is conducive to higher fluorine contamination and more chromium bonded to oxygen on the grain boundaries, and hence, higher fluoride ion and lower chromium ion concentrations in the crack tip water.

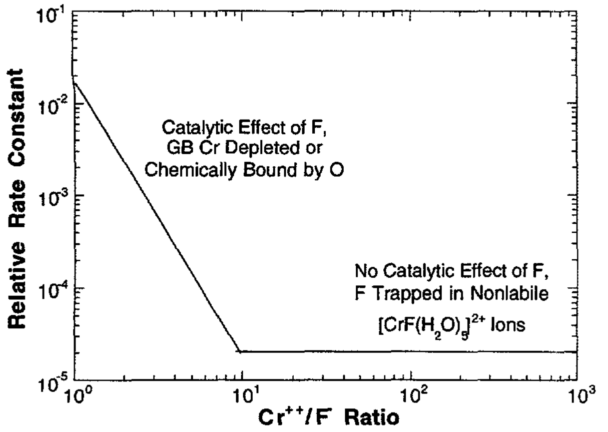

Figure 49.
Schematic illustration of effects of oxygen and fluoride on grain boundaries and chromium ion in crack-tip water on oxyfluorine-assisted SCC

3.3 Fracture Toughness J-R Test of Austenitic Stainless Steels Irradiated in Halden Reactor (E. E. Gruber and O. K. Chopra)

The facility for fracture toughness J-R testing of irradiated compact tension (CT) specimens in a hot cell has been designed, fabricated, and assembled. J–R curve tests are being conducted according to ASTM Specification E 1737 (Standard Test Method for J–Integral Characterization of Fracture Toughness) at room temperature and 288°C on nonirradiated specimens to validate the test procedure. The method involves pin loading of fatigue precracked specimens and determination of J as a function of crack growth. Load versus loadline (LL) displacement is recorded to calculate the J–integral. The calculated J–integral is plotted against estimated or physical crack lengths Δa, within specified limits of crack growth. The crack length and crack growth are being determined from both elastic compliance measurements and direct current (DC) potential drop technique.

During the current reporting period, fatigue crack growth and fracture toughness J–R curve tests have been conducted at room temperature and 288°C on two heats of thermally aged CF–8M cast SS (ANL Heat 75 with 28% ferrite and Framatome Heat 4331 with 23% ferrite) to validate the test procedure. Physical crack lengths were measured optically after the tests. The results from these tests have been used to develop correlations for estimating crack lengths from the DC potential drop and elastic unloading compliance methods.

3.3.1 J–R Curve Test Procedure

A detailed description of the facility has been presented in Ref. 76. Figure 50 shows the configuration of the CT specimens irradiated in the Halden reactor. Although the Halden specimens are rectangular, their dimensions are comparable to those of disk–shaped compact tension DC(T) specimens. Consequently, calculations for crack length and J–integral were performed using the correlations recommended for DC(T) specimens in ASTM Specification E 1737.

Specimen extension is monitored and controlled outside of the high-temperature zone. The displacement of load points (center of the loading pins) is determined by subtracting the machine compliance from the measured extension. The curves for machine compliance, expressed in terms of load versus displacement (of the loading points), at room temperature and 288°C are shown in Fig. 51. However, during unloading, the load versus displacement curves varied with the maximum applied load. Figure 52 shows examples of unloading

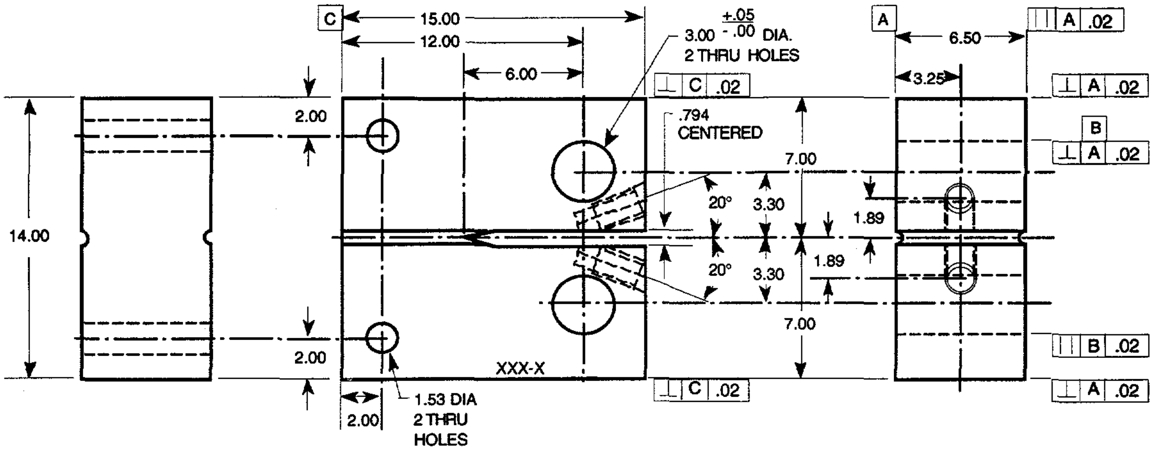

Figure 50. Configuration of compact-tension specimen for this study

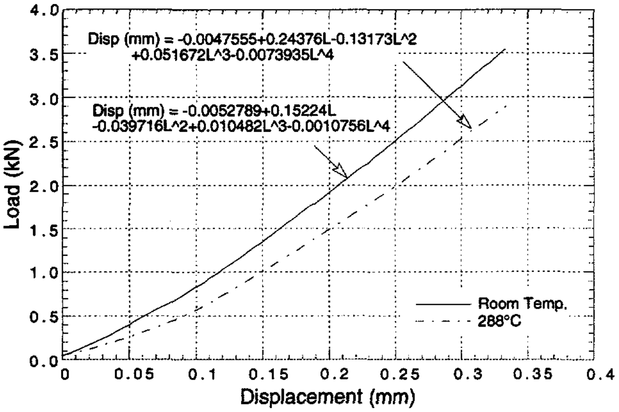

Figure 51.
Machine compliance expressed in terms of load versus displacement of loading points at room temperature and 288°C

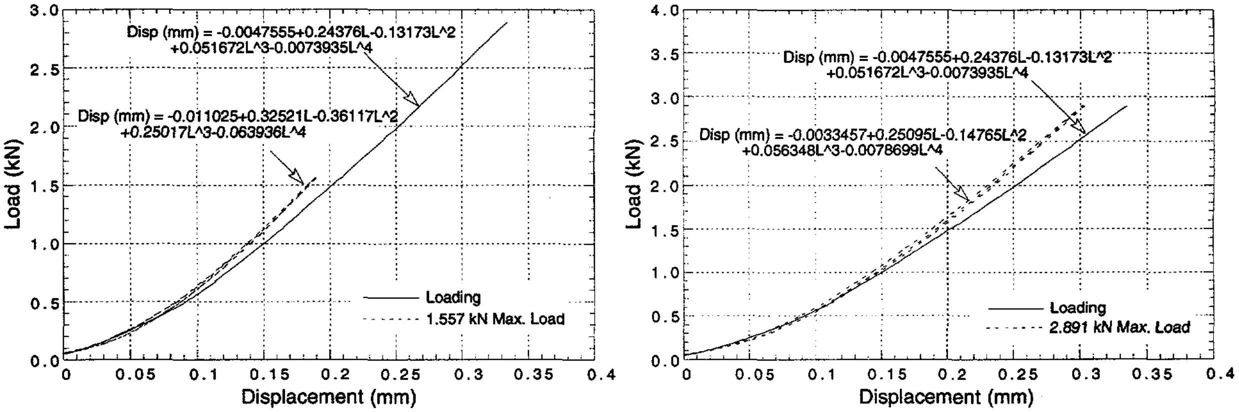

Figure 52. Unloading machine compliance at 288°C for maximum loads of 1557 and 2891 N

compliance curves at 288°C and maximum loads of 667 and 2891 N (150 and 650 lb.). For the J–R curve tests at room temperature, the actual displacement of load points was measured optically and compared with the estimated loadline displacement. The measured and estimated values of loadline displacement were in very good agreement; examples are shown in Fig. 53. For loadline displacements up to 2 mm, the error in the estimated values is <0.02 mm.

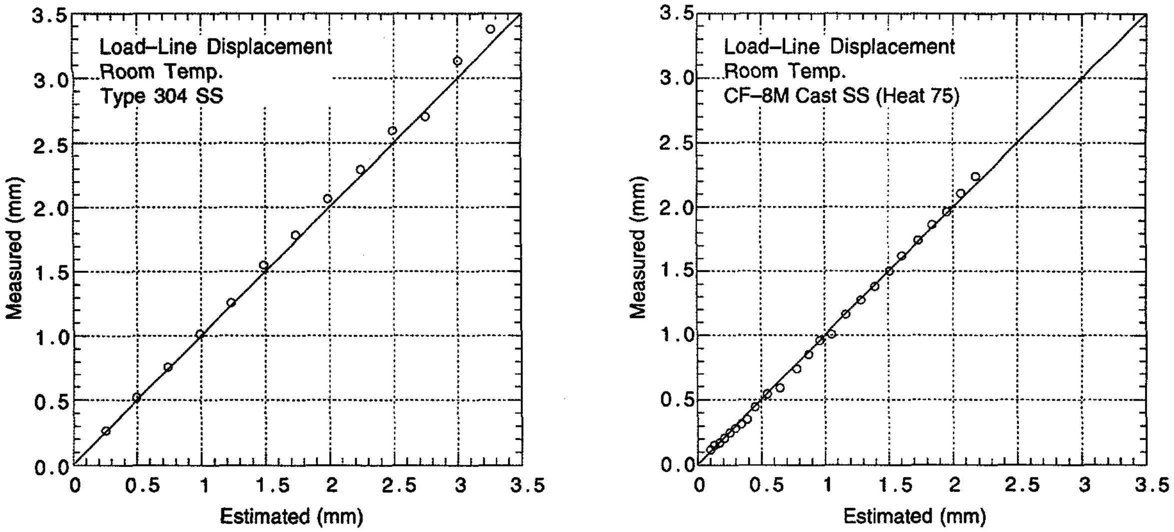

Figure 53. Measured and estimated values of loadline displacement for Type 304 SS and CF-8M cast SS tested at room temperature

Prior to testing, the specimens were fatigue-precracked at room temperature and at loads based on the maximum allowable load P_m given by the relation

$$P_m = (0.4\ \sigma_f\ B_N\ b^2)/(2W + a), \tag{16}$$

where W is specimen width, a is crack length, B_N is net specimen thickness (distance between roots of the side grooves), b is noncracked ligament (distance from the crack front to the back edge of the specimen, i.e., W – a), and σ_f is flow stress expressed as the mean of the yield and ultimate stress. The final fatigue precrack extension was carried out at loads $\leq P_m$ or a load such that the ratio of the maximum stress intensity applied during fatigue precracking to the elastic modulus (K_{max}/E) was $\leq 1.6 \times 10^{-4}\ m^{1/2}$ ($\leq 0.001\ in.^{1/2}$).

The fatigue precracked specimens were loaded at a constant extension rate and the tests were interrupted periodically to determine the crack length. The specimen was held at constant extension to measure crack length by both the DC potential drop and elastic unloading compliance techniques. The maximum range of unload/reload for crack extension measurements was the smaller of $0.5P_m$ or 50% of the current load. For most steels, load relaxation occurs during the hold period or unloading, which causes a time-dependent nonlinearity in the unloading curve. Consequently, prior to unloading, the specimen was held for ≈1 min to allow for load relaxation. Furthermore, because specimen extension is monitored and controlled away from the specimen in the present method, the specimen is actually being strained during the hold period due to load relaxation. Typically, for a load relaxation of ≈0.1 kN (≈22 lb.), the specimen will extend by ≈0.01 mm.

For each test, the final crack size was marked by heat tinting and/or by fatigue cycling at room temperature. The specimens were then fractured and the initial (i.e., fatigue precrack) and final (test) crack lengths were measured optically for both halves of the fractured specimen. The crack lengths were determined by the 9/8 averaging technique, i.e., the two-near-surface measurements were averaged and the resultant value was averaged with the remaining seven measurements.

3.3.2 *Calculations of Crack Length*

Elastic Unloading Compliance Method:

For a single-specimen method using the elastic compliance technique on DC(T) specimens with crack opening displacements measured at the loadline, the crack length a_i from ASTM E 1737 is given by

$$a_i/W = 0.998193 - 3.88087u_x + 0.187106u_x^2 + 20.3714u_x^3 \\ -45.2125u_x^4 + 44.527u_x^5, \quad (17)$$

where

$$u_x = \frac{1}{\left[(B_{ef}E_{ef}C_{ci})^{1/2} + 1\right]}, \quad (18)$$

$$B_{ef} = B - (B - B_N)^2 / B, \quad (19a)$$

$$E_{ef} = E / (1 - \upsilon^2). \quad (19b)$$

W is the specimen width, B is the specimen thickness, B_N is the net specimen thickness, E is the elastic modulus, υ is Poisson's ratio, and C_{ci} is the corrected specimen elastic compliance. The measured compliance is corrected for rotation of the crack centerline according to the expression

$$C_{ci} = \frac{C_i}{\left[\frac{H^*}{R}\sin\theta - \cos\theta\right]\left[\frac{D}{R}\sin\theta - \cos\theta\right]} \quad (20)$$

where

$$\theta = \sin^{-1}\left[\frac{\left(\frac{d_m}{2} + D\right)}{\left(D^2 + R^2\right)^{1/2}}\right] - \tan^{-1}\left(\frac{D}{R}\right). \quad (21)$$

C_i is the measured specimen elastic compliance at the loadline, H^* is the initial half-span of the load points (i.e., center of the pin holes), R is the radius of rotation of the crack centerline (Fig. 54) and is given by $(W+a_i)/2$, D is one-half of the initial distance between the displacement measuring points, d_m is the total measured loadline displacement, and θ is the angle of rotation of a rigid body element about the unbroken midsection line.

Experimental values of normalized crack length and u_x from several fatigue–precrack and fracture toughness J–R tests are plotted in Fig. 55. The results indicate that the ASTM E 1737 correlations yield good estimates of the depth of fatigue precracks over the entire range of 6–10 mm (i.e., a/W values of 0.5–0.8). However, for J–R curve tests, estimates of the final crack lengths are somewhat lower than the measured values. Best fit of experimental values of u_x and crack length yield the following expression:

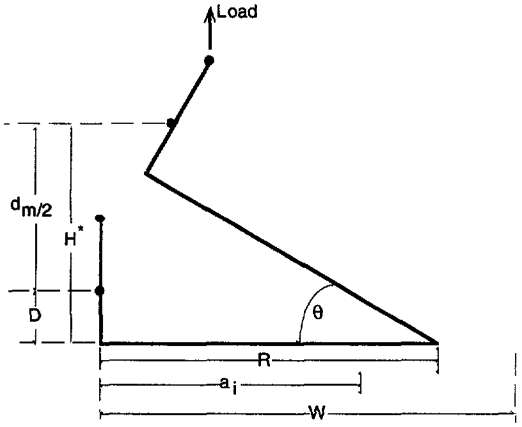

Figure 54.
Elastic compliance correction for specimen rotation

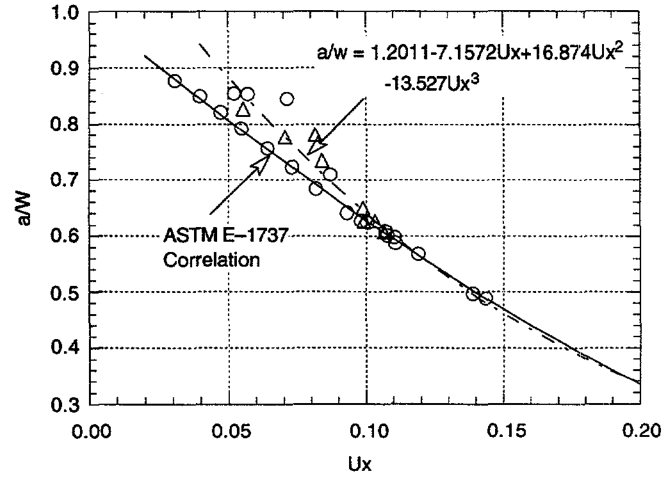

Figure 55.
Normalized crack length versus normalized potential drop data for solution annealed and cast stainless steels tested at room temperature and 288°C

$$a_i/W = 1.2011 - 7.1572u_x + 16.874{u_x}^2 - 13.527{u_x}^3. \tag{22}$$

In the present study, crack extensions are determined from Eq. 22 for fracture toughness J–R tests and from Eq. 17 for fatigue crack growth studies. Furthermore, because the J values depend strongly on the a_o used to calculate the Δa_i quantities, measured values of a_o were adjusted by the following procedure.

(a) Identify all J_i and a_i pairs for which the load at the start of unloading exceeds P_m and a_i is $\leq a_{min} + 2.5$ mm, where a_{min} is the smallest estimated crack length that meets the P_m requirement. Use this data to calculate a revised a_o (Fig. 56) from

$$a = a_o + \frac{J}{4\sigma_f} + a_2J^2 + a_3J^3. \tag{23}$$

(b) If there are <8 data points or the correlation coefficient of fit is <0.96, the data set is inadequate to evaluate any toughness measures by this method.

(c) If the optically measured crack length a_o differs from the adjusted a_o value by more than 0.01W, the data set is inadequate according to this method.

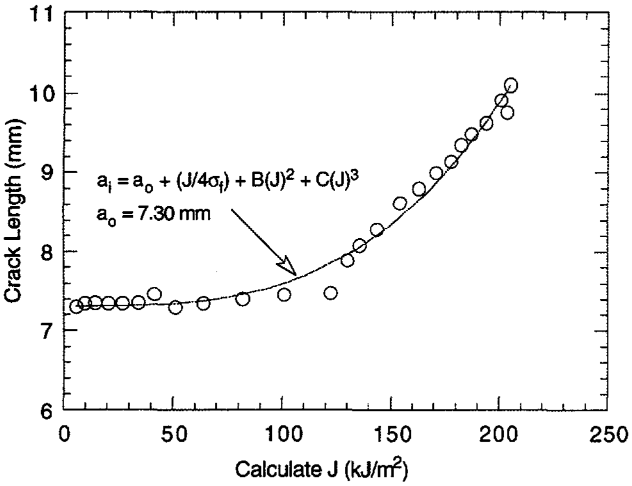

Figure 56.
Calculated J versus crack length for specimen 75–01T tested at room temperature

(d) With the corrected specimen elastic compliance C_{ci}, corresponding to the a_o value in Eq. 23, determine an effective elastic modulus E_{ef} in Eq. 17, that is required to give the measured initial precrack length a_o in Eqs. 16 or 22.

(e) The adjusted value of E_{ef} is used in Eq. 17 to determine crack length from elastic unloading compliance.

DC Potential Method:

Experimental values of normalized crack length and normalized DC potential from several fatigue–precrack and fracture toughness J–R tests are plotted in Fig. 57. A best–fit of experimental data yields the following expression

$$\frac{a_i}{W} = \left[0.28887\left(\frac{U}{U_o} - 0.5\right)\right]^{0.34775}, \qquad (24)$$

where W is the specimen width, and U and U_o are the current and initial potentials. Equation 9 is comparable to the ASTM E 1737 correlation for a CT specimen with current inputs at the W/4 position and DC potential lead connections at the W/3 position. Figure 57 shows that only four data points (three at room temperature and one at 288°C) do not follow this trend and were excluded from the analysis. These points represent the final crack length for J–R tests, and correspond to loadline displacements of ≈3 mm or more.

The DC potential data were corrected for the effects of plasticity on the measured potential, i.e., large crack–tip plasticity can increase measured potentials due to resistivity increases without crack extension. As per ASTM E1737, the change in potential prior to the attainment of crack initiation was ignored and the remainder of the potential change was used to establish the J–R curve. A plot of normalized potential versus loadline displacement (Fig. 58) generally remains linear until the onset of crack extension (point B in Fig. 58). For all data prior to point B, crack extension was expressed as $a_o + \Delta a_B$, where a_o is the initial crack length and Δa_B is calculated from the blunting line relationship $\Delta a = J/(4\sigma_f)$. Note that for cast SSs, a slope of four times the flow stress ($4\sigma_f$) for the blunting line expresses the fracture toughness data better than a slope of $2\sigma_f$ defined in ASTM E 1737.

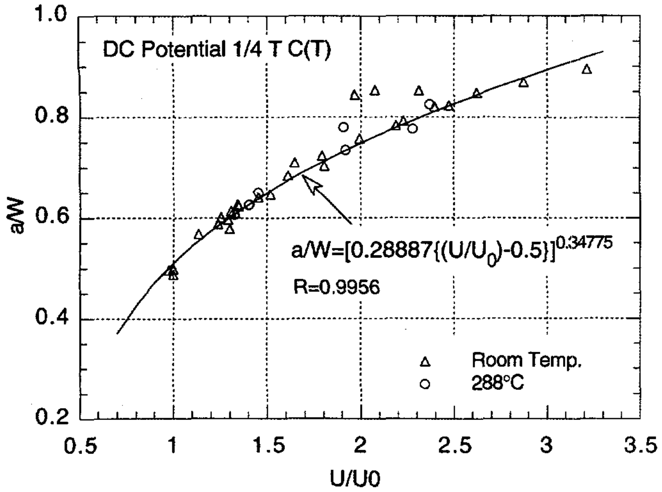

Figure 57.
Normalized crack length versus normalized DC potential data for solution-annealed and cast stainless steels tested at room temperature and 288°C

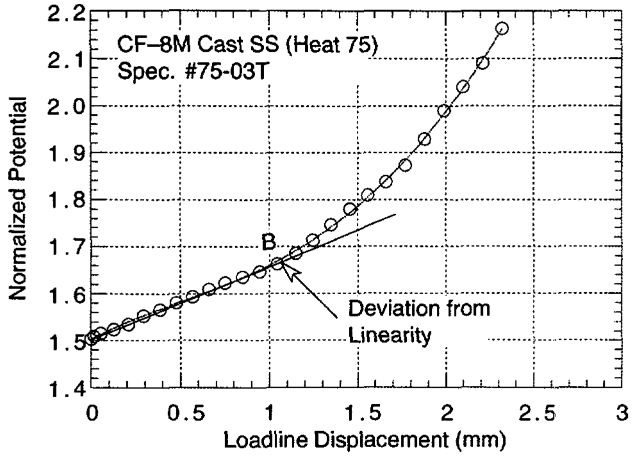

Figure 58.
Normalized potential versus loadline displacement for specimen 75–03T tested at 288°C

The measured potentials from the test data were corrected by using the two-point pinning method. The corrected normalized potentials $\overline{NP}$ are expressed in terms of the measured normalized potentials NP (or U/U_0 in Eq. 24) by the relation

$$\overline{NP} = \frac{NP - P_1}{P_2 - P_1}. \tag{25}$$

The variables P_1 and P_2 are solutions of the expressions

$$\overline{NP}_i = \frac{NP_i - P_1}{P_2 - P_1} \tag{26}$$

and $$\overline{NP}_f = \frac{NP_f - P_1}{P_2 - P_1}, \tag{27}$$

where $\overline{NP}_i$ and $\overline{NP}_f$ are normalized potentials that correspond to initial and final crack lengths determined from Eq. 24, and NP_i and NP_f are the measured values.

3.3.3 Calculations of J–Integral

The J–integral is calculated from the load and loadline displacement curves. The total J is the sum of the elastic and plastic components, J_{el} and J_{pl}, respectively,

$$J = J_{el} + J_{pl}. \tag{28}$$

The total area and plastic component of the area $A_{pl(i)}$ at each recorded deflection are computed during the test by summing the increase in areas for each increment in deflection; the elastic component of deflection is calculated from specimen loadline elastic compliance at each step and subtracted from the total deflection to obtain plastic deflection. The elastic component of J, at a point corresponding to a_i, V_i, P_i on the specimen load versus loadline displacement record, is given by

$$J_{el(i)} = \frac{(K_{(i)})^2(1-\upsilon^2)}{E_{ef}}, \tag{29}$$

where the stress intensity $K_{(i)}$ is expressed as

$$K_{(i)} = \left[\frac{P_i}{(BB_NW)^{1/2}}\right] f\left(\frac{a_i}{W}\right), \tag{30}$$

$$f\left(\frac{a_i}{W}\right) = \left[\frac{\left(2+\frac{a_i}{W}\right)}{\left(1-\frac{a_i}{W}\right)^{3/2}}\right]\left\{0.76 + 4.8\left(\frac{a_i}{W}\right) - 11.58\left(\frac{a_i}{W}\right)^2 + 11.43\left(\frac{a_i}{W}\right)^3 - 4.08\left(\frac{a_i}{W}\right)^4\right\}, \tag{31}$$

and P_i is the load. The plastic component of J is given by

$$J_{pl(i)} = \left[J_{pl(i-1)} + \left(\frac{\eta_{(i-1)}}{b_{(i-1)}}\right)\frac{A_{pl(i)} - A_{pl(i-1)}}{B_N}\right]\left[1 - \gamma_{(i-1)}\frac{a_{(i)} - a_{(i-1)}}{b_{(i-1)}}\right], \tag{32}$$

where the factors that account for limited crack growth $\gamma_{(i)}$ and for the tensile component of the load $\eta_{(i)}$ are expressed as

$$\eta_{(i-1)} = 2.0 + 0.552\frac{b_{(i-1)}}{W}, \tag{33}$$

$$\gamma_{(i-1)} = 1.0 + 0.76\frac{b_{(i-1)}}{W}, \tag{34}$$

and $B_{(i-1)}$ is the remaining ligament (distance from the physical crack front to the back edge of the specimen) at a point i-1.

The quantity $A_{pl(i)} - A_{pl(i-1)}$ is the increment of plastic area under the load versus loadline displacement record between lines of constant displacement at points i-1 and i. The quantity

$J_{pl(i)}$ represents the total crack-growth-corrected plastic J at point i and is obtained by first incrementing the existing $J_{pl(i-1)}$ and then by modifying the total accumulated result to account for the crack growth increment. Accurate evaluations of $J_{pl(i)}$ require small uniform crack-growth increments. The plastic area under the load versus loadline displacement record is given by

$$A_{pl(i)} = A_{pl(i-1)} + \frac{[P_i + P_{i-1}][V_{pl(i)} - V_{pl(i-1)}]}{2}, \tag{35}$$

where the total and plastic component of loadline displacement, $V_{(i)}$ and $V_{pl(i)}$, respectively, are expressed as

$$V_{pl(i)} = V_{(i)} - P_i C_{ci}. \tag{36}$$

3.3.4 Fracture Toughness J–R Tests

Figures 59-64 show the load versus loadline displacement curves and fracture toughness J–R curves for thermally aged CF–8M cast SS (ANL Heat 75 with 28% ferrite and Framatome Heat 4331 with 23% ferrite) at room temperature and 288°C. The ANL heat was aged for 10,000 h at 400°C and the Framatome heat for 700 h at 400°C. The J–R curves obtained from the elastic unloading compliance method show good agreement with those obtained from the DC potential method. In the present study, the J–R curves from DC potential method are corrected for both the initial and final crack lengths, whereas the curves from the elastic compliance method are corrected only for the initial precrack length. Consequently, there are some differences between the two curves for the tests that underestimate the final crack length.

The fracture toughness J–R curves obtained from 1/4T–CT specimens of Heats 75 and 4331 using the DC potential method are compared with those obtained from 1T–CT specimens of the same heats[77] in Figs. 65 and 66, respectively. The curves for 1/4T–CT specimens are somewhat lower than those for the 1T–CT specimens. However, the J_{ic} values for the two specimens are comparable.

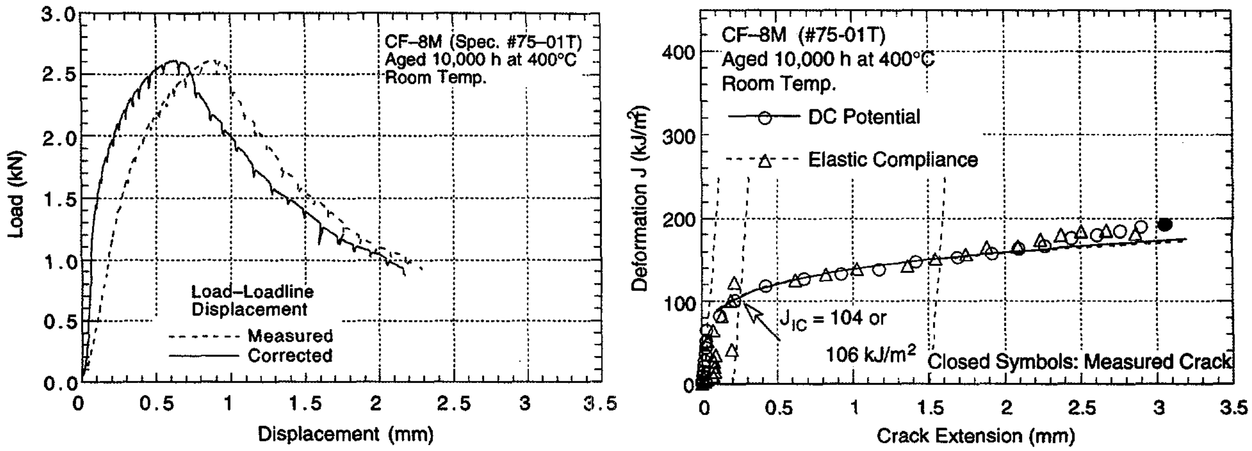

Figure 59. Load versus loadline displacement and fracture toughness J–R curves for specimen 75–01T tested at room temperature

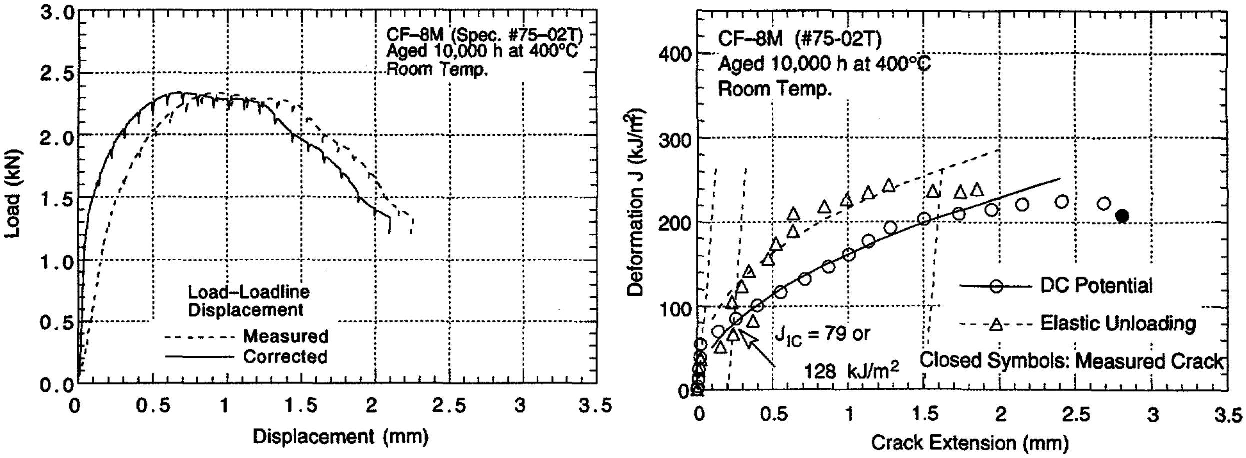

Figure 60. Load versus loadline displacement and fracture toughness J–R curves for specimen 75–02T tested at room temperature

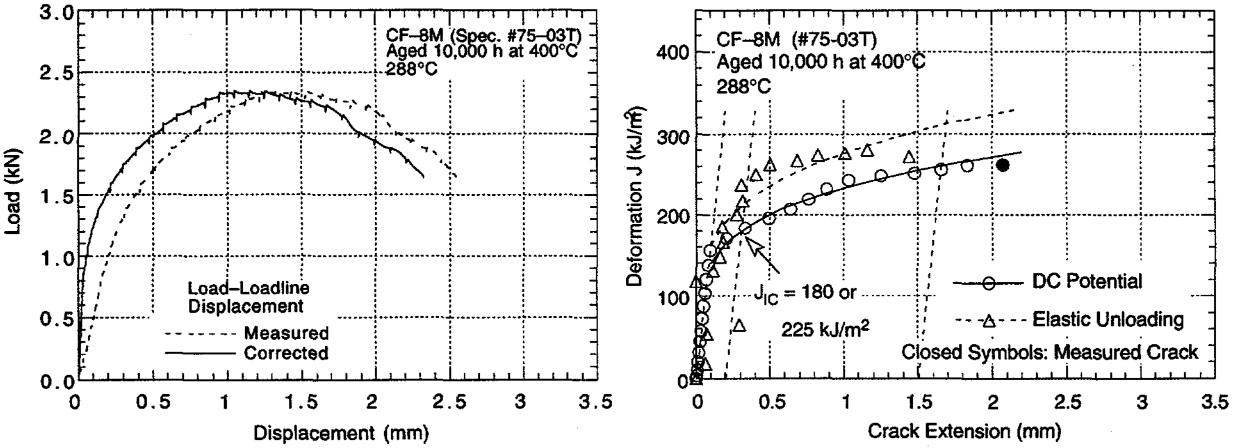

Figure 61. Load versus loadline displacement and fracture toughness J–R curves for specimen 75–03T tested at 288°C

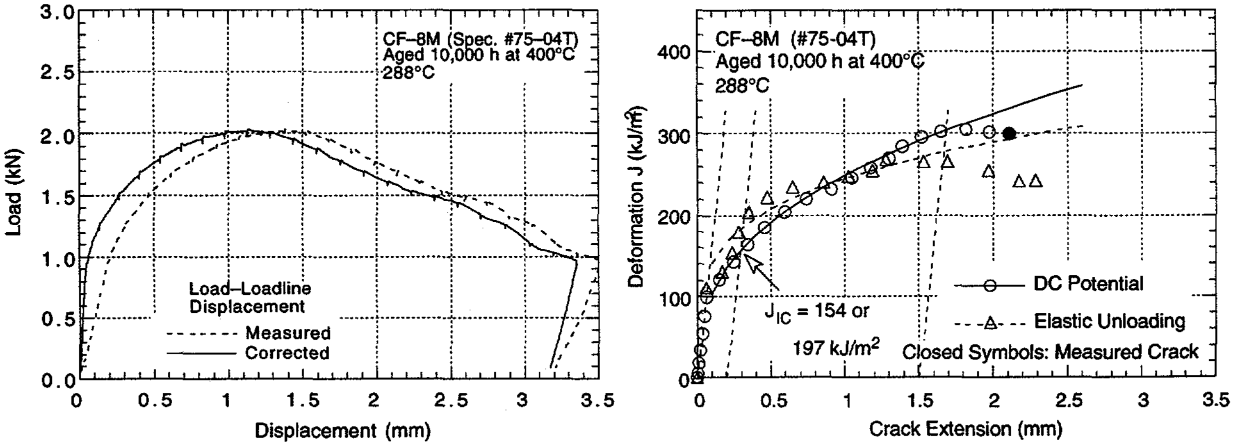

Figure 62. Load versus loadline displacement and fracture toughness J–R curves for specimen 75–04T tested at 288°C

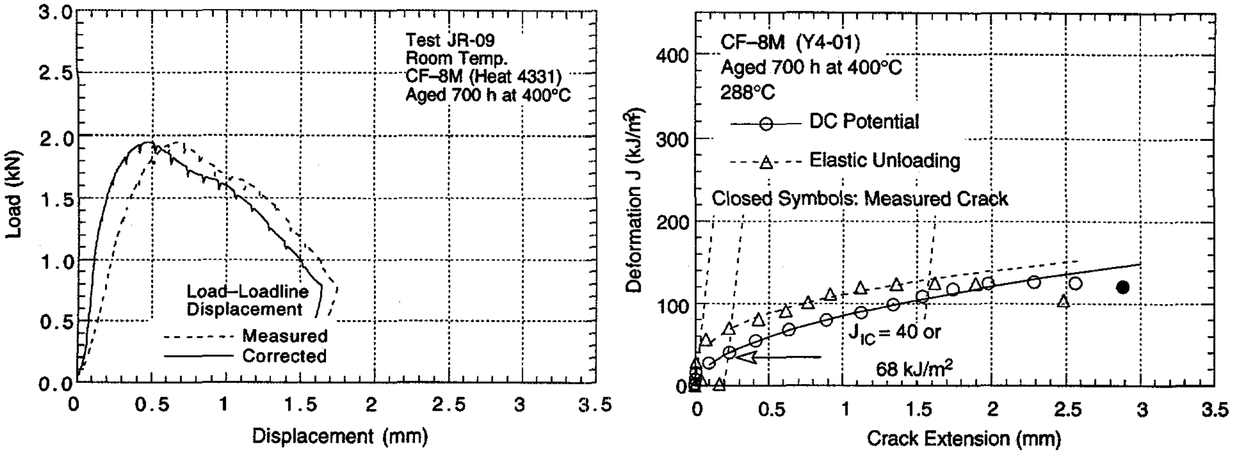

Figure 63. Load versus loadline displacement and fracture toughness J–R curves for specimen Y4–01 tested at room temperature

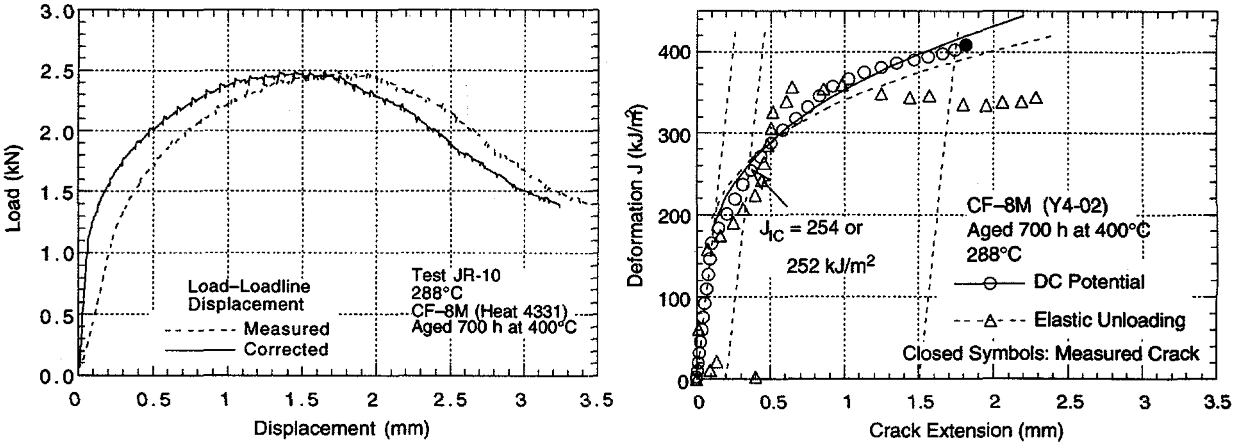

Figure 64. Load versus loadline displacement and fracture toughness J–R curves for specimen Y4–02 tested at 288°C

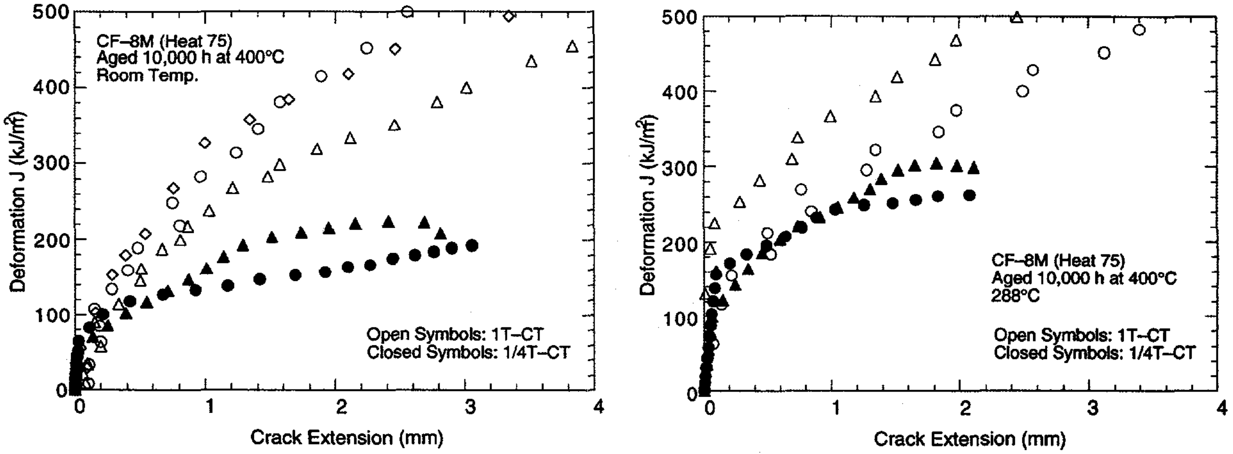

Figure 65. Fracture toughness J–R curves for 1/4T–CT and 1T–CT specimens of aged CF–8M Heat 75 at room temperature and 288°C

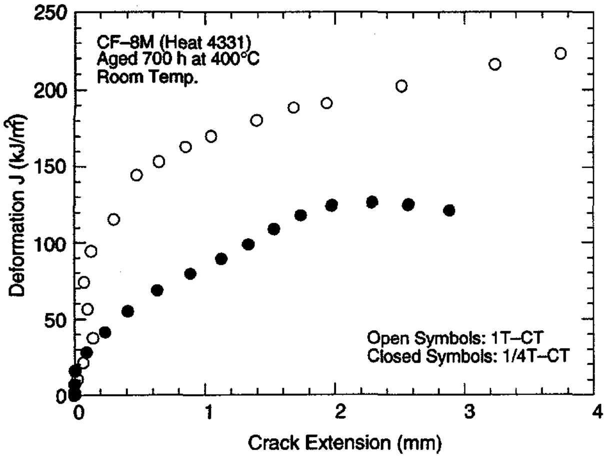

Figure 66.
Fracture toughness J–R curves for 1/4T–CT and 1T–CT specimens of aged CF–8M Heat 4331 at room temperature

4 Environmentally Assisted Cracking of Alloys 600 and 690 in Simulated LWR Water (W. E. Ruther, W. K. Soppet, and T. F. Kassner)

The objective of this work is to evaluate the resistance of Alloys 600 and 690 to EAC in simulated LWR coolant environments. High–nickel alloys have experienced general corrosion (tube wall thinning), localized intergranular attack (IGA), and SCC in LWRs. Secondary–side IGA[*] and axial and circumferential SCC[**] have occurred in Alloy 600 tubes at tube support plates in many steam generators. Primary–water SCC of Alloy 600 steam generator tubes in PWRs at roll transitions and U–bends and in tube plugs[***] is a widespread problem that has been studied intensively. Cracking has also occurred in Alloy 600 and other high–nickel alloys (e.g., Inconel–82 and –182 and Alloy X750) that are used in applications such as instrument nozzles and heater thermal sleeves in the pressurizer[†] and the penetrations for control–rod drive mechanisms in reactor vessel closure heads in the primary system of PWRs;[††] in dissimilar–metal welds between SS piping and low-alloy steel nozzles, in jet pump hold–down beams,[†††] and in shroud–support–access–hole covers[§] in BWRs. In general, thermomechanical processing of Alloy 600 for these applications differs from those used for steam generator tubes. Because environmental degradation of the alloys in many cases is very sensitive to processing, further evaluation of SCC is needed. In addition, experience strongly

---

[*] USNRC Information Notice No. 91–67, "Problems with the Reliable Detection of Intergranular Attack (IGA) of Steam Generator Tubing," Oct. 1991.

[**] USNRC Information Notice No. 90–49, "Stress Corrosion Cracking in PWR Steam Generator Tubes," Aug. 1990; Notice No. 91–43, "Recent Incidents Involving Rapid Increases in Primary–to–Secondary Leak Rate," July 1991; Notice No. 92–80, "Operation with Steam Generator Tubes Seriously Degraded," Dec. 1992; Notice No. 94–05, "Potential Failure of Steam Generator Tubes with Kinetically Welded Sleeves," Jan. 1994.

[***] USNRC Information Notice No. 89–33, "Potential Failure of Westinghouse Steam Generator Tube Mechanical Plugs," March 1989; Notice No. 89–65, "Potential for Stress Corrosion Cracking in Steam Generator Tube Plugs Supplied by Babcock and Wilcox," Sept. 1989; Notice No. 94–87, "Unanticipated Crack in a Particular Heat of Alloy 600 Used for Westinghouse Mechanical Plugs for Steam Generator Tubes," Dec. 1994.

[†] USNRC Information Notice No. 90–10, "Primary Water Stress Corrosion Cracking (PWSCC) of Inconel 600," Feb. 1990.

[††] USNRC Generic Letter 97-01: "Degradation of Control Rod Drive Mechanism and Other Vessel Closure Head Penetrations," Apr. 1, 1997; USNRC Information Notice No. 96–11, "Ingress of Demineralizer Resins Increases Potential for Stress Corrosion Cracking of Control Rod Drive Mechanism Penetrations," Feb. 1996; INPO Document SER 20–93 "Intergranular Stress Corrosion Cracking of Control Rod Drive Mechanism Penetrations," Sept. 1993.

[†††] USNRC Information Notice No. 93–101, "Jet Pump Hold–Down Beam Failure," Dec. 1993.

[§] USNRC Information Notice No. 92–57, "Radial Cracking of Shroud Support Access Hole Cover Welds," Aug. 1992.

suggests that materials that are susceptible to SCC are also susceptible to environmental degradation of fatigue life and fatigue–crack growth properties. In this investigation, we have obtained information on the effect of temperature, load ratio R, and stress intensity (K) on EAC of Alloys 600 and 690 in simulated BWR and PWR water.

4.1 Experimental Methods for Measuring CGR in Alloys 600 and 690

The experimental procedures relevant to our mechanical loading systems are similar to those in ASTM E647. The tests are performed under controlled loading conditions with closed–loop servo–controlled machines (MTS™ systems). The contribution to the load that arises from the pressure difference between the inside and the outside of the autoclave is taken into consideration. Additional mechanical contributions that arise from friction between the pull rod in the load train and the autoclave pressure seal are typically <0.4% of the mechanical loading force under autoclave operating pressure and temperature.

The tests in air are performed in a system that is also used for tests in simulated reactor coolant environments. Air is circulated at a slow rate through the autoclave at atmospheric pressure to help maintain a uniform temperature within the autoclave. For tests in air, there is no mechanical contribution from pressure differences between the inside and the outside of the autoclave or from friction in the load train, because there is no seal between the pull rod and the autoclave.

A DC potential–drop measurement system is used for both the tests in air and those in an HP water environment. The specimens in the load train are electrically insulated from the autoclave and each other by using oxidized Zircaloy 705 pins (oxidized by heating at 550°C for 4-8 h) to attach the specimens to the load train. The resistance across the crack is measured by the potential drop for each specimen as a computer automatically controls a programmable DC power supply to direct the electrical current first in one direction and then in the reverse direction. The DC and drops in potential are measured by high-accuracy, stable, scanning multimeters that are controlled by the computer over an IEEE-488 interface. Hundreds of measurements are averaged for one reading, which is transformed to a crack length by a software algorithm that is integral to the control computer. Corrosion-fatigue specimens are held at operating conditions without mechanical loading until the resistance of the specimens stabilizes, typically one week, before the initial fatigue loading at $R = 0.4$ is applied. Resolution of the crack length varies somewhat from one specimen to another and depends on the alloy composition and uniform crack length; a typical value is ±0.05 mm (0.002 in.) for Alloy 600 or 690.

When tests are conducted in a simulated PWR environment (boric acid, lithium hydroxide and a hydrogen overpressure), the DC potential-drop system, which indicates negative CGRs, fails shortly after the cracks begin to grow. Our best explanation at present is that hydrogen enters the metal matrix and changes the intrinsic resistance of the specimen. For CGR tests in simulated PWR water, a compliance technique that was used previously was upgraded to perform measurements without interrupting the corrosion-fatigue test.

The compliance measurement system is composed of MTS™ Model 632.10 hermetically sealed crack-opening-displacement (COD) gauges interfaced to a computer data acquisition system along with a conditioned load cell signal. Prior to each test, the COD gauges are calibrated with a micrometer fixture to an accuracy of ±1% at the desired test temperature.

The micrometer fixture is calibrated with gauge blocks that are traceable to the National Institute of Standards and Technology. The resulting typical COD gauge output transfer function is 0.075 mm/V. Experience with compliance measurements with MTS™ clip gauges indicates that the resolution is ±0.025 mm (0.001 in.). The computer data acquisition system accepts the multiplexed load and COD voltage signals with a resolution of ±0.05% of the applied voltage range. Compliance data from the load cell and COD gauges are acquired during the unloading phase of the ramp waveform. Initially, the load-versus-COD data are graphically analyzed to select the region of the waveform with the steepest linear slope to optimize the data acquisition period. The compliance value for a test cycle is computed by a least-squares linear-regression analysis of 250 data samples. The computer software monitors the fit of the linear regression curve for a minimum correlation coefficient of 0.999. During a corrosion-fatigue test, ten successive load-line compliance values are recorded at 1-h time intervals, averaged, and applied to a subroutine that calculates crack length by means of a polynomial elastic compliance expression derived for CT and wedge-opening-load specimens.[78] However, for conditions of accelerated crack growth, the measurement time interval can be reduced to 10 min.

Both the initial crack length and the crack length and shape at the end of the test are determined from the fracture surface for comparison with measurements inferred from COD or DC potential–drop measurements. The specimen is cut into two pieces along the midplane of the thickness, and the crack in one piece is extended by fracturing at a cryogenic temperature. One of these segments is used to examine the fracture surface by SEM. Excess metal in the noncracked region of the other piece is removed with a cutoff wheel, and a transverse section is prepared and polished for metallographic evaluation of the region that contains the corrosion–fatigue crack to confirm the nature of the crack path and determine whether crack branching had occurred.

Water for the CGR test systems is obtained from a reverse-osmosis purification system and is passed through a demineralizer with mixed–bed ion–exchange resins; the conductivity is <0.1 $\mu S \cdot cm^{-1}$. To avoid contamination by nonionic organic contaminants, the water flows though a final water purification system (e.g., a Millipore Super–Q Ultrapure Water System™ coupled with an Ultra Dynamics UV Purifier™) that contains a bed of activated charcoal, an Organex bed, a resin bed, and a 0.2-µm filter. The purified water is stored in 135-L SS feedwater tanks that are refilled weekly. The feedwater tanks are connected to the autoclave systems with SS tubing. Whenever the conductivity of the stored feedwater solution increases to ≥0.1 $\mu S \cdot cm^{-1}$ during the storage period, the tanks are spray-sterilized/passivated with a 10% hydrogen peroxide solution and thoroughly rinsed with deionized water prior to refilling. The DO level is adjusted by vacuum sparging of the filled tanks; nitrogen or hydrogen is used for low-DO tests and oxygen-nitrogen gas mixtures are used to establish predetermined DO levels. Final adjustment of the effluent DO in the latter tests is achieved by slightly varying the storage tank pressure and/or the flow rate of water in the autoclave. The DO concentration in the effluent stream from the autoclaves is monitored by Chemetrics™ ampoules and/or by an Orbisphere™ DO monitor. The electrochemical potential of platinum and SS electrodes is measured versus a room-temperature 0.1N KCl/Ag/AgCl reference electrode located in the high–temperature effluent stream (289°C) from the autoclave. The platinum potential, in particular, responds rapidly to changes in DO concentrations in simulated LWR coolant water.

4.2 Tensile Properties of Solution–Annealed and Thermally Treated Alloys 600 and 690

The composition, microstructure, and tensile properties of heats of Alloys 600 and 690 that have been used in the fatigue–crack–growth investigation were reported previously.[79,80] Alloy 600 and 690 material, for which crack growth data were obtained during this reporting period, was provided by the Electric Power Research Institute, Palo Alto, CA. The heat of Alloy 600 (NX9244G) with a low-carbon content (0.03 wt.%) was produced by INCO Alloys International, Huntington, WV, for the Kobe Material Testing Laboratory Co. Ltd., Hyogo, Japan. The plates were heat treated at the Kobe Material Testing Laboratory and cut into small blocks (≈32 x 65 x 140 mm) for distribution to various laboratories that are participating in the International Crack Growth-EAC investigation of Alloy 600 in simulated BWR and PWR environments. The composition of the materials is given in Table 13. Compact-tension specimens of the low-carbon content material (Heat NX9244G) were fabricated so that the orientation of the crack plane in the specimens corresponds to the identification code T-L for plates in ASTM Specification E399. In our previous CGR experiments on other heats of Alloys 600 and 690, including Heats NX8844J-26 and NX8244HK-1B of Alloys 600 and 690, respectively, the CT specimens were in the L-T orientation.

Tensile specimens were also obtained from the blocks and from several of the CT specimens of the low-carbon heat of Alloy 600 after the CGR tests were completed. The tensile properties of this material at 25, 290, and 320°C in four heat-treatment conditions, hardness at room temperature, and grain size are given in Table 14, together with results for heats of Alloy 600 and 690 for which CGR data were obtained in simulated PWR water during this reporting period. Two blocks of low-carbon heat of Alloy 600 material were solution-annealed at 1025 and 1115°C for 2 h, and two blocks that had been subjected to these solution heat treatments were thermally treated at 600°C for 24 h. Solution heat treatments at 1025 and 1115°C produced ASTM grain sizes of ≈1.0-1.5 and 0.2-0.4, respectively, corresponding to average grain diameters of ≈250-210 and 340-310 µm (Fig. 67). The ultimate tensile strengths at 290°C for materials that were solution-annealed at 1025 and 1115°C are ≈550 and 513 MPa, respectively. The yield strength was 156 MPa for three heat-treatment conditions and was slightly higher (173 MPa) for material that was solution-annealed at 1025°C and thermally treated. Because of the low carbon content and relatively high solution-annealing temperatures, intergranular carbides were not observed in the specimens by optical microscopy and SEM. The Alloy 600 and 690 heats with normal carbon contents of ≈0.06 and 0.02 wt.% C, respectively, were in the solution-annealed condition (1038 and 1093°C for 1 h, respectively). Heat NX8844J-26 of Alloy 600 contained semicontinuous intergranular and intragranular carbides, and Heat NX8844HK-1B of Alloy 690 had continuous intergranular but few intragranular carbides.[79,80] These heats were also used in corrosion-fatigue experiments in air and HP water that were reported previously.[81,82]

Figure 68 shows the dependence of yield stress on grain size for Heat NX9244G (≈0.03 wt.% C) in the solution-annealed and solution-annealed and thermally treated conditions and Heat NX8844 (≈0.06 wt.% C) in the solution-annealed condition. Heat treatment of the low-carbon material (Heat NX9244G) at 600°C for 24 h has virtually no effect on tensile properties when compared with material that was solution-annealed at the two temperatures. The data follow a Petch relationship, i.e., $\sigma_y = \sigma_i + k \cdot d^{-1/2}$, where σ_y is the yield stress; d is the grain diameter; k, an empirical constant; and σ_i, the "friction" stress, which is a measure of intrinsic resistance of the material for dislocation motion. The dependence in

Table 13. Composition of Alloys 600 and 690 used for corrosion fatigue tests

Material	Heat		Composition (wt.%)															
	No.	Analysis	Cr	Mo	Ni	Fe	Mn	Si	C	N	P	S	B	Cu	Ti	Al	Co	Nb+Ta
Alloy 600	NX8844	Vendor	14.97	0.15	75.21	8.26	0.26	0.24	0.069	0.01	0.009	<0.001	0.004	0.22	0.29	0.27	0.04	–
	NX8844J-26	ANL	15.00	0.16	74.94	8.14	0.23	0.32	0.060	0.0155	0.014	0.002	0.004	0.22	0.24	0.24	0.03	0.03
Alloy 600	NX9244G	Vendor	15.51	–	75.32	7.90	0.23	0.25	0.032	0.01	0.007	<0.001	0.001	0.09	0.39	0.20	–	0.02
	NX9244G-J31	ANL	15.47	0.13	75.40	7.73	0.23	0.37	0.040	0.0052	0.010	0.001	0.001	0.07	0.40	0.17	0.06	<0.01
	NX9244G-J32	ANL	16.39	0.11	75.50	7.44	0.22	0.35	0.030	0.0067	0.011	0.001	0.001	0.08	0.40	0.17	0.06	0.01
Alloy 690	NX8244HK	Vendor	30.03	–	59.85	9.20	0.20	0.14	0.018	0.01	0.004	<0.001	0.002	<0.01	0.20	0.36	0.003	–
	NX8244HK-1B	ANL	30.64	<0.01	59.20	9.19	0.21	0.18	0.023	0.011	0.005	0.002	0.002	<0.01	0.19	0.32	<0.01	<0.01

Table 14. Tensile properties of Alloys 600 and 690 in various heat-treatment conditions

Alloy 600 Heat No.	Material Condition	Test No.	Spec. No.	Temp. (°C)	σ_u (MPa)	σ_y (MPa)	ε_t (%)	RA (%)	Hardness[a] (VN)	Hardness (R_b)	ASTM Grain Size
NX8844J-26	Annealed 1038°C/1 h	–[b]	–[b]	25	694.3	298.6	41.0	–	–	86	4
NX8844J-26	Annealed 1038°C/1 h	T21	J26-05[c]	25	653.5	245.5	49.2	61.1	173	87	4
NX8844J-26	Annealed 1038°C/1 h	T23	J26-06[c]	290	637.8	234.0	45.2	53.3	–	–	–
NX8844J-26	Annealed 1038°C/1 h	T44	J26-08[c]	290	626.5	218.0	48.7	57.2	–	–	–
NX8844J-26	Annealed 1038°C/1 h	T25	J26-07[c]	320	639.4	246.8	45.8	48.9	–	–	–
NX9244G	Mill Annealed	–[b]	–[b]	25	657.0	300.0	43.9	60.6	–	83	–
NX9244G-J320	Annealed 1025°C/2 h	T43	J320-04[c]	25	580.6	205.1	62.7	82.0	145	78	1.0
NX9244G-J320	Annealed 1025°C/2 h	T38	J320-02[c]	290	547.9	155.7	68.4	72.2	–	–	–
NX9244G-J320	Annealed 1025°C/2 h	T39	J320-03[c]	320	551.9	154.5	69.9	70.1	–	–	–
NX9244G-J321	Annealed 1025°C/2 h + 600°C/24 h	T32	J321-03[c]	25	582.0	208.4	59.5	66.1	148	79	1.5
NX9244G-J321	Annealed 1025°C/2 h + 600°C/24 h	T35	J321-05[c]	290	552.1	172.5	65.2	59.8	–	–	–
NX9244G-J321	Annealed 1025°C/2 h + 600°C/24 h	T34	J321-04[c]	320	551.6	166.9	67.0	64.4	–	–	–
NX9244G-J310	Annealed 1115°C/2 h	T40	J310-01[c]	25	551.7	188.7	58.7	77.5	144	78	0.4
NX9244G-J310	Annealed 1115°C/2 h	T41	J310-02[c]	290	508.9	155.7	65.5	68.8	–	–	–
NX9244G-J310	Annealed 1115°C/2 h	T42	J310-03[c]	320	507.5	146.1	67.7	69.5	–	–	–
NX9244G-J311	Annealed 1115°C/2 h + 600°C/24 h	T30	J311-03[d]	25	545.7	194.5	57.2	61.5	–	–	–
NX9244G-J311	Annealed 1115°C/2 h + 600°C/24 h	T31	J311-04[c]	25	553.1	196.4	56.8	63.0	142	77	0.2
NX9244G-J311	Annealed 1115°C/2 h + 600°C/24 h	T33	J311-05[c]	290	517.0	155.7	66.7	65.9	–	–	–
NX9244G-J311	Annealed 1115°C/2 h + 600°C/24 h	T36	J311-06[c]	320	514.9	155.7	65.3	60.6	–	–	–
Alloy 690											
NX8244HK-1B	Annealed 1093°C/1 h	–[b]	–[b]	25	602.8	212.3	59.0	–	–	70	–
NX8244HK-1B	Annealed 1093°C/1 h	T22	K1B-05[c]	25	592.2	215.6	70.5	71.6	146	78	2
NX8244HK-1B	Annealed 1093°C/1 h	T24	K1B-06[c]	290	504.9	145.2	70.6	68.1	–	–	–
NX8244HK-1B	Annealed 1093°C/1 h	T26	K1B-07[c]	320	499.4	150.9	67.1	67.3	–	–	–

[a] Vickers hardness at room temperature, 500 gf, 15 s.

[b] Results from vendor (EPRI document or certified material test reports).

[c] Tensile tests conducted in air at a strain rate of $1.0 \times 10^{-4}\ s^{-1}$.

[d] Tensile test conducted in air at a strain rate of $1.0 \times 10^{-5}\ s^{-1}$.

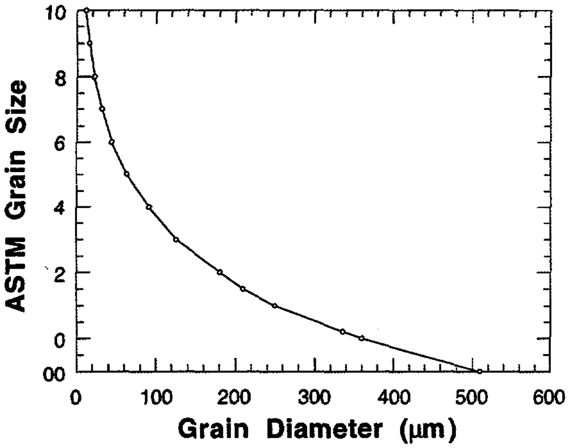

Figure 67.
Relationship between ASTM grain size number and average grain diameter

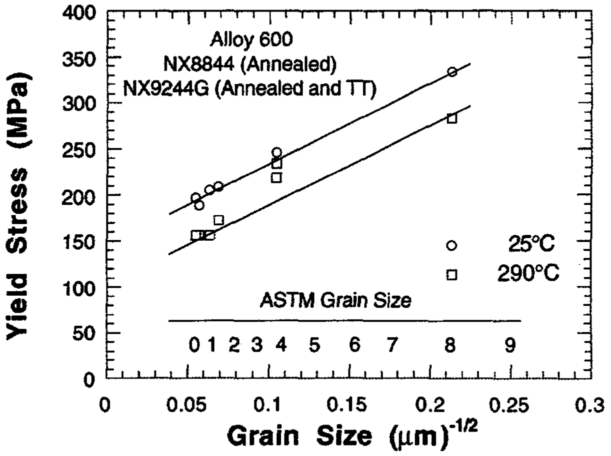

Figure 68.
Dependence of 0.2% yield stress at 25 and 290°C on grain size of solution-annealed and thermally treated Alloy 600 specimens

Fig. 68 may be somewhat fortuitous because the decrease in tensile stress for the material with the large grain size (Heat NX9244G), may be caused in part by the low carbon content of the material.

4.3 Crack Growth Rates of Alloys 600 and 690 in Simulated PWR Water at 289°C

Corrosion fatigue experiments were conducted on Alloys 600 and 690 (Heat Nos. NX8844J–26 and NX8244HK–1B) at 289°C in simulated PWR water that contained 450 ppm boron, 2.25 ppm lithium, <1 ppb DO, and ≈0, 42, and 55 cm^3 H_2·kg^{-1} H_2O at room-temperature pH of ≈7.0. The composition of the materials is given in Table 13. Crack growth was determined by the compliance method with MTS™ clip gages. The compact-tension specimens, in the L-T orientation, were in the solution-annealed condition; 1038° and 1093°C for 1 h, respectively. The yield strengths and ASTM grain sizes for these heat-treatment conditions are 234 and 145 MPa at 289°C, and 4 and 2, respectively. The Alloy 600 specimen (J26-02) has semicontinuous intergranular and intragranular carbides, whereas the Alloy 690 specimen (K1B-02) has continuous intergranular but few intragranular carbides. The experimental conditions and results from 13 CGR tests at stress intensity values and load ratios of ≈30–47 MPa·$m^{1/2}$ and 0.2–0.8, respectively, are given in Table 15. The frequency and rise time T_r of the positive sawtooth waveform were 8×10^{-2} Hz and 12 s, respectively. This

Table 15. *Crack growth results at 289°C in simulated PWR water for Alloy 600 and 690 specimens*[a]

		Water Chemistry									Alloy 600			Alloy 690		
								Electrode Potential			Specimen No. J26-02			Specimen No. K1B-02		
Test No.	Test Time (h)	B Conc. (ppm)	Li Conc. (ppm)	H_2[b] Conc. (cm^3·kg^{-1})	O_2[b] Conc. (ppb)	Cond. at 25°C (µS·c m^{-1})	pH at 25°C	Alloy 600 mV(SHE) @ 289°C	Pt	Load Ratio[c]	K_{max}[d] (MPa·m$^{1/2}$)	ΔK[e]	Rate (10^{-10} m·s^{-1})	K_{max}[d] (MPa·m$^{1/2}$)	ΔK[e]	Rate (10^{-10} m·s^{-1})
1	265–365	450	2.25	–	<1	23.0	7.08	–687	–668	0.54	30.4	13.98	10.4	31.3	14.40	22.9
2	385–432	450	2.25	–	<1	23.0	7.08	–687	–673	0.50	30.9	15.45	18.0	32.5	16.25	35.2
3	437–485	450	2.25	–	<1	23.0	7.08	–688	–675	0.45	31.8	17.49	33.9	33.9	18.65	49.7
4	647–673	450	2.25	–	<1	23.0	7.08	–680	–672	0.40	32.8	19.68	59.5	35.0	21.00	69.4
5	678 696	450	2.25	–	<1	23.0	7.08	–679	–674	0.35	33.8	21.97	92.9	36.0	23.40	93.8
6	703 719	450	2.25	–	<1	23.0	7.08	–663	–669	0.30	35.3	24.71	143.1	37.4	26.18	126.5
7	719 726	450	2.25	–	<1	23.0	7.08	–663	–669	0.25	36.1	27.11	189.9	38.2	28.61	168.0
8	743 750	450	2.25	–	<1	23.0	7.08	–671	–669	0.20	37.2	29.76	255.1	39.1	31.27	225.0
9	819–877	450	2.25	–	<1	23.0	7.08	–681	–669	0.70	37.4	11.22	6.20	39.9	11.97	16.3
10	911–1014	450	2.25	–	<1	24.0	6.86	–687	–675	0.75	37.7	9.43	3.73	40.6	10.15	11.7
11	1015–1321	450	2.25	–	<1	24.0	6.86	–699	–678	0.80	37.7	7.54	<0.05	40.6	8.12	<0.05
12	2230–2255	450	2.25	42.4	<1	22.7	7.09	–799	–793	0.50	41.5	20.75	80.6	46.3	23.15	94.0
13	2332–2340	450	2.25	55.1	<1	22.7	7.09	–802	–797	0.40	42.2	25.32	124.0	47.3	28.38	138.0

[a] Compact tension specimens (1TCT) of Alloys 600 and 690, Heat Nos. NX8844J-26 and NX8244HK-1B, respectively. The specimens (Nos. J26-02 and K1B-02) were tested in the solution-annealed condition (1038°C for 1h and 1093°C for 1h, respectively). Yield stresses of the materials at 289°C for these heat-treatment conditions are 234 and 145 MPa, respectively. Crack growth was determined by the compliance method with MTS ™clip gauges.

[b] Effluent dissolved-hydrogen and DO concentrations were determined with an Orbisphere hydrogen meter and high-sensitivity Chemetrics ampules, respectively.

[c] Frequency and rise time of the positive sawtooth waveform were 8 x 10^{-2} Hz and 12 s, respectively.

[d] Stress intensity, K_{max}, values at the end of the time period.

[e] $\Delta K = K_{max}(1 - R)$, where K_{max} where load ratio $R = K_{min}/K_{max}$.

range of R and K_{max} values produced $\Delta K = K_{max}(1 - R)$ values of ≈9-31 $MPa{\cdot}m^{1/2}$ and CGRs between ≈4 x 10^{-10} and 2.5 x 10^{-8} $m{\cdot}s^{-1}$. The dependence of the CGRs on ΔK from the results in Table 15 is shown in Fig. 69. The dependence on ΔK of the CGR for each specimen is given by a power-law relationship; the coefficient-of-fit indicated on the figure is quite good.

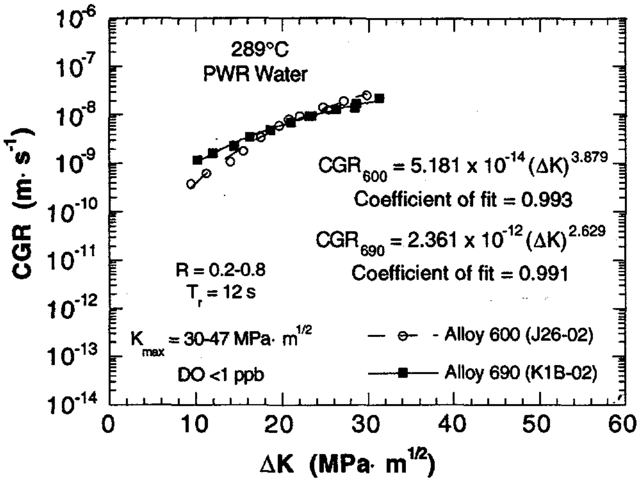

Figure 69.
Dependence of CGRs in simulated PWR water at 289°C on ΔK of Alloy 600 and 690 specimens solution-annealed at 1038 and 1093°C, respectively

4.4 Crack Growth Rates of Low-Carbon Alloy 600 in Simulated PWR Water at 320°C

Corrosion-fatigue experiments were conducted on Alloy 600 specimens in simulated PWR water at 320°C to determine the effects of heat treatment conditions, load ratio, and stress intensity on CGRs. Two specimens from a heat of low-carbon Alloy 600 (NX9244G), both solution-annealed at 1115°C for 2 h and one thermally treated at 600°C for 24 h, were tested in one autoclave system; another autoclave contained two specimens from this heat, both of which were solution-annealed at 1025°C for 2 h and one that was also thermally treated at 600°C for 24 h. The alloy was produced by INCO Alloys International, Huntington, WV, for the Kobe Material Testing Laboratory Co. Ltd., Hyogo, Japan. The plates were heat treated at the Kobe Material Testing Laboratory and cut into small blocks (≈32 x 65 x 140 mm) for distribution to various laboratories that are participating in the International Crack Growth-EAC investigation of Alloy 600 in simulated BWR and PWR environments. The composition of the material is also given in Table 13. Compact-tension specimens were fabricated so that the orientation of the crack plane in the specimens corresponds to the identification code T-L for plates in ASTM Specification E399. In our previous CGR experiments on other heats of Alloys 600 and 690, the CT specimens were in the L-T orientation.

The solution heat treatments at 1025 and 1115°C produced ASTM grain sizes of ≈1.0-1.5 and 0.2-0.4, respectively, which correspond to average grain diameters of ≈250-210 and 340-310 μm. The ultimate tensile and yield strengths at 320°C for materials that were solution annealed at 1025 and 1115°C are ≈552 and 508 MPa and 155 and146 MPa, respectively. The corresponding values for the material that was solution-annealed at the two temperatures and thermally treated at 650°C for 24 h are ≈552 and 515 MPa and 167 and 156 MPa, respectively. Because of the low carbon content and relatively high solution-annealing temperatures, intergranular carbides were not observed in the specimens by optical microscopy and SEM.

The experimental conditions and results from 16 CGR tests on each set of specimens are given in Tables 16 and 17. In these experiments, the water contained 1200 ppm boron, 2.25 ppm lithium, <1 ppb DO, and ≈23-39 cm^3 $H_2 \cdot kg^{-1}$ H_2O at room-temperature pH of ≈6.4. Crack growth was determined by the compliance method with MTS™ clip gauges. The experiments were conducted at load ratios R between 0.2 and 0.95 and maximum stress intensity values K_{max} between ≈24 and 46 $MPa \cdot m^{1/2}$. The frequency and rise time T_r of the positive sawtooth waveform were 8 x 10^{-2} Hz and 12 s, respectively. This range of R and K_{max} values produced $\Delta K = K_{max}$ (1 - R) values of ≈1.6-26 $MPa \cdot m^{1/2}$ and CGRs between ≈2 x 10^{-11} and 8 x 10^{-9} $m \cdot s^{-1}$. The dependence of the CGRs on ΔK from the results in Tables 16 and 17 is shown in Figs. 70 and 71, respectively, in which the dependence on ΔK of the CGR for each specimen is given by a power-law relationship.

Figures 70 and 71 indicate that the CGRs of the solution-annealed specimens are slightly higher than those of the thermally treated specimens. This behavior was also evident in the CGR data in HP water that contained 300 ppb DO at 289°C.[82] The results indicate that under these conditions solution-annealing temperatures (1025 versus 1115°C) and thermal treatment at 600°C for 24 h do not produce large variations in CGRs of this heat of low-carbon, large-grain-size material in either simulated PWR or BWR[82] water at 320 and 289°C, respectively. The combined data from four specimens in two experiments in each environment are shown in Fig. 72. The CGR data in simulated PWR and BWR water at the two temperatures are quite similar, as indicated by the CGR correlations and the coefficients of fit of the data depicted in the figure.

4.5 Comparison of CGRs of Low-Carbon Alloy 600 in Simulated PWR and BWR Water and Air

The CGRs in simulated PWR and BWR water of specimens of Alloy 600 from Heat No. NX9244G with different heat-treatment conditions (Fig. 72) can be compared with CGRs in air from another heat of Alloy 600 (NX8197), which were reported previously (Fig. 73).[81] A similar comparison could be made for Alloy 600 (Heat No. NX8844J-26) and Alloy 690 (Heat No. NX8244HK-1B) in the solution-annealed condition, although CGR data for this set of specimens were not obtained under high-R, low-ΔK conditions (Fig. 69). The most useful comparison would be for rates in water and in air, determined from the same heat of material with the same heat treatment; however, the present results preclude such a comparison. Nevertheless, a ratio of the CGRs for each specimen in water at 320°C or 289°C to those in air at 289°C, or from the combined data from several specimens with differing heat treatments to those in air can be obtained from the "best-fit" correlations for the CGR-versus-ΔK data. Ratios of the CGRs versus ΔK for the low-carbon-content heat of Alloy 600 (NX9244G) in simulated PWR and BWR water at 320 and 289°C, respectively, (Fig. 72) and in air at 289°C (Fig. 73) are shown in Fig. 74.

Intuitively, the results in Fig. 74 are consistent with premise that CGRs of nickel-base alloys and austenitic SS increase with DO concentration in high-temperature water. The results suggest that temperature (320 versus 289°C) plays a lesser role in crack propagation because the CGRs are lower in simulated PWR than in BWR water in these experiments despite the higher temperature of the low-DO PWR environment which also contains 23-39 $cm^3 \cdot kg^{-1}$ H_2, 1200 ppm boron (as H_3BO_3), and 2.25 ppm lithium (as LiOH). Ratios of the CGRs for this heat of Alloy 600 in water and air indicate that the rates are higher in water than in air (ratio >1) at ΔK values <18 and <10 $MPa \cdot m^{1/2}$ in BWR and PWR water, respectively,

Table 16. *Crack growth results at 320°C in simulated PWR water for Alloy 600 specimens[a] annealed at 1115°C*

Test No.	Test Time (h)	Water Chemistry B Conc. (ppm)	Li Conc. (ppm)	H_2[b] Conc. ($cm^3 \cdot kg^{-1}$)	O_2[b] Conc. (ppb)	Cond. at 25°C ($\mu S \cdot cm^{-1}$)	pH at 25°C	Electrode Potential Alloy 600 mV(SHE) @ 289°C	Pt mV(SHE) @ 289°C	Load Ratio[c]	Alloy 600 (Annealed) Specimen No. J310–01 K_{max}[d] ($MPa \cdot m^{1/2}$)	ΔK[e] ($MPa \cdot m^{1/2}$)	Rate (10^{-10} $m \cdot s^{-1}$)	Alloy 600 (TT) Specimen No. J311–01 K_{max}[d] ($MPa \cdot m^{1/2}$)	ΔK[e] ($MPa \cdot m^{1/2}$)	Rate (10^{-10} $m \cdot s^{-1}$)
1	55–197	1200	2.25	31.2	<1	21.5	6.44	-697	-713	0.70	26.3	7.90	7.96	25.1	7.52	2.03
2	197–315	1200	2.25	30.8	1	21.5	6.44	-720	-727	0.60	27.0	10.8	11.8	25.2	10.1	1.83
3	315–482	1200	2.25	26.9	<1	21.1	6.45	-729	-733	0.50	28.5	14.2	16.6	25.4	12.7	3.49
4	482–530	1200	2.25	29.1	<1	21.1	6.45	-738	-735	0.40	29.2	17.5	26.6	25.6	15.4	9.15
5	531–562	1200	2.25	29.1	<1	21.1	6.45	-739	-735	0.30	29.5	20.7	26.8	26.1	18.2	24.0
6	562–819	1200	2.25	23.7	<1	21.7	6.43	-735	-732	0.80	29.5	5.90	0.94	26.2	5.24	1.03
7	820–915	1200	2.25	23.7	<1	21.7	6.43	-733	-739	0.55	30.4	13.68	13.7	26.3	11.84	3.21
8	915–1921	1200	2.25	30.8	<1	21.7	6.43	-739	-741	0.90	30.6	3.06	0.22[f]	26.5	2.65	0.25[f]
9	1925–2018	1200	2.25	30.8	<1	21.7	6.43	-744	-746	0.65	31.2	10.92	11.7	26.6	9.31	1.11
10	2019–2595	1200	2.25	30.6	<1	21.7	6.43	-743	-746	0.85	31.4	4.71	0.44	26.6	3.99	0.04[f]
11	2595–2666	1200	2.25	31.2	<1	21.7	6.42	-747	-749	0.67	31.7	10.45	7.69	26.6	8.78	0.83
12	2667–2697	1200	2.25	31.4	<1	21.7	6.42	-747	-749	0.45	32.2	17.69	27.6	26.7	14.69	12.9
13	2697–2716	1200	2.25	31.4	<1	21.7	6.42	-749	-749	0.35	32.5	21.14	21.7	26.9	17.46	7.07
14	2717–2739	1200	2.25	31.4	<1	21.7	6.42	-749	-750	0.20	33.1	26.46	39.2	27.3	21.86	40.2
15	2740–2764	1200	2.25	31.4	<1	21.7	6.42	-749	-750	0.33	33.6	22.68	32.1	27.8	18.74	34.9
16	2764–2833	1200	2.25	-	<1	21.7	6.42	-749	-750	0.63	33.8	12.51	7.45	27.8	10.27	1.43

[a] Compact tension specimens (1TCT) of Alloy 600, Heat No. NX9244G. The specimens (Nos. J310–01 and J311–01) were tested in the solution-annealed (1115°C for 2h) and solution-annealed and thermally treated (1115°C for 2h and 600°C for 24h) conditions, respectively. Yield stresses of the materials at 320°C for these heat-treatment conditions are 146 and 156 MPa, respectively. Crack growth was determined by the compliance method with MTS ™clip gauges.

[b] Effluent dissolved-hydrogen and DO concentrations were determined with an Orbisphere hydrogen meter and high-sensitivity Chemetrics ampules, respectively.

[c] Frequency and rise time of the positive sawtooth waveform were 8×10^{-2} Hz and 12 s, respectively.

[d] Stress intensity, K_{max}, values at the end of the time period.

[e] $\Delta K = K_{max}(1 - R)$, where load ratio $R = K_{min}/K_{max}$.

[f] Rates are based on difference in crack lengths at the beginning of the subsequent test and the end of the previous test because the rates are below the sensitivity level of the compliance measurement system for the time of the experiment.

Table 17. Crack growth results at 320°C in simulated PWR water for Alloy 600 specimens[a] annealed at 1025°C

Test No.	Test Time (h)	Water Chemistry B Conc. (ppm)	Li Conc. (ppm)	H_2[b] Conc. ($cm^3 \cdot kg^{-1}$)	O_2[b] Conc. (ppb)	Cond. at 25°C ($\mu S \cdot cm^{-1}$)	pH at 25°C	Electrode Potential Alloy 600 mV(SHE) @ 289°C	Pt	Load Ratio[c]	Alloy 600 (Annealed) Specimen No. J320–01 K_{max}[d] ($MPa \cdot m^{1/2}$)	ΔK[e]	Rate ($10^{-10}\ m \cdot s^{-1}$)	Alloy 600 (TT) Specimen No. J321–01 K_{max}[d] ($MPa \cdot m^{1/2}$)	ΔK[e]	Rate ($10^{-10}\ m \cdot s^{-1}$)
1	0–165	1200	2.25	33.0	<1	21.3	6.39	-584	-657	0.40	25.3	15.18	19.8	24.4	14.64	10.0
2	165–335	1200	2.25	37.3	<1	21.3	6.39	-570	-686	0.70	25.8	7.74	11.3	24.5	7.35	6.64
3	360–408	1200	2.25	39.1	<1	21.3	6.39	-601	-700	0.40	26.2	15.72	18.6	24.6	14.76	8.09
4	410–505	1200	2.25	39.1	<1	22.0	6.44	-608	-704	0.60	26.7	10.68	10.4	24.7	9.88	2.55
5	505–557	1200	2.25	33.7	<1	22.7	6.39	-612	-704	0.50	27.1	13.55	16.2	24.8	12.40	6.21
6	557–600	1200	2.25	30.9	<1	22.7	6.39	-614	-706	0.30	27.6	19.32	22.6	25.4	17.78	25.4
7	600–887	1200	2.25	38.3	<1	22.2	6.38	-624	-710	0.80	27.9	5.58	2.63	25.5	5.10	1.08
8	889–1896	1200	2.25	35.7	<1	21.6	6.41	-643	-715	0.90	28.7	2.87	1.52[f]	26.0	2.60	1.18[f]
9	1898–1924	1200	2.25	29.2	<1	21.3	6.43	-672	-716	0.25	29.1	21.8	28.6	26.5	19.9	47.1
10	1925–2040	1200	2.25	29.1	<1	21.3	6.43	-673	-717	0.75	29.2	7.30	4.15	26.5	6.63	1.25
11	2041–2592	1200	2.25	27.7	<1	21.6	6.41	-640	-658	0.85	29.4	4.41	0.68[f]	26.5	3.98	<0.01[f]
12	2593–2760	1200	2.25	27.9	<1	21.3	6.37	-735	-739	0.73	29.9	8.23	5.77	26.6	7.31	1.15
13	2762–2785	1200	2.25	27.9	<1	21.3	6.37	-736	-740	0.20	30.5	24.4	38.7	27.4	21.9	77.8
14	2789–3384	1200	2.25	24.8	<1	21.3	6.42	-730	-733	0.95	34.8	1.74	0.65	31.3	1.56	<0.01[f]
15	3385–3863	1200	2.25	23.4	2	21.4	6.41	-741	-745	0.95	39.6	1.98	1.10	35.8	1.79	<0.01[f]
16	4225–4705	1200	2.25	25.7	2	21.6	6.39	-721	-730	0.95	45.8	2.29	2.27	40.3	2.01	0.25

[a] Compact tension specimens (1TCT) of Alloy 600, Heat No. NX9244G. The specimens (Nos. J320–01 and J321–01) were tested in the solution-annealed (1025°C for 2h) and solution-annealed and thermally treated (1025°C for 2h and 600°C for 24h) conditions, respectively. Yield stresses of the materials at 320°C for these heat-treatment conditions are 155 and 167 MPa, respectively. Crack growth was determined by the compliance method with MTS ™clip gauges.

[b] Effluent dissolved-hydrogen and DO concentrations were determined with an Orbisphere hydrogen meter and high-sensitivity Chemetrics ampules, respectively.

[c] Frequency and rise time of the positive sawtooth waveform were 8×10^{-2} Hz and 12 s, respectively.

[d] Stress intensity, K_{max}, values at the end of the time period.

[e] $\Delta K = K_{max}(1 - R)$, where load ratio $R = K_{min}/K_{max}$.

[f] Rates are based on difference in crack lengths at the beginning of the subsequent test and the end of the previous test because the rates are below the sensitivity level of the compliance measurement system for the time of the experiment.

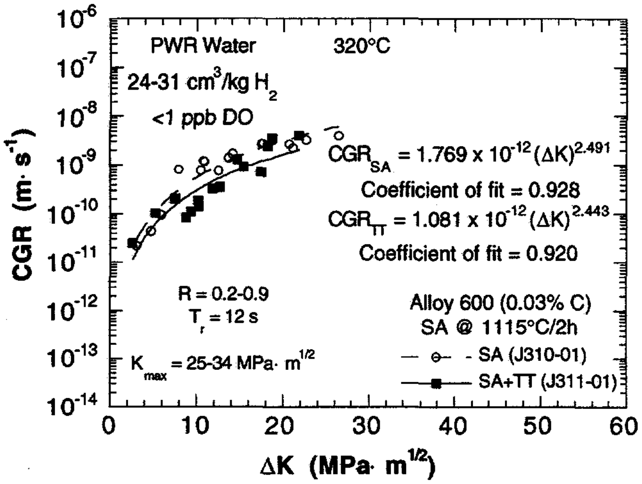

Figure 70. Dependence of CGRs in simulated PWR water at 320°C on ΔK of Alloy 600 specimens solution-annealed at 1115°C and solution-annealed at this temperature and thermally treated at 600°C for 24 h

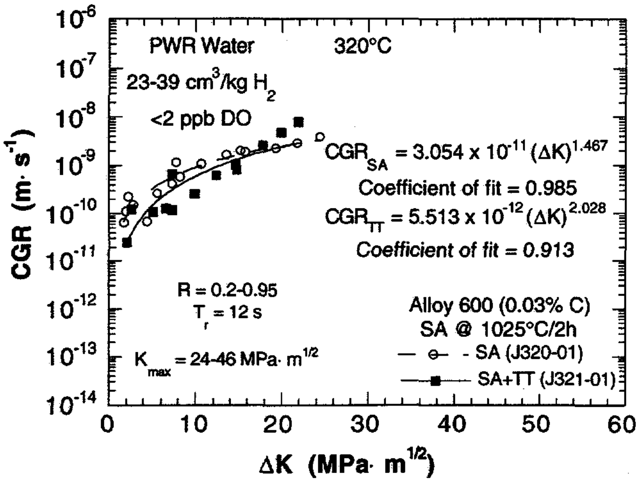

Figure 71. Dependence of CGRs in simulated PWR water at 320°C on ΔK of Alloy 600 specimens solution-annealed at 1025°C and solution-annealed at this temperature and thermally treated at 600°C for 24 h

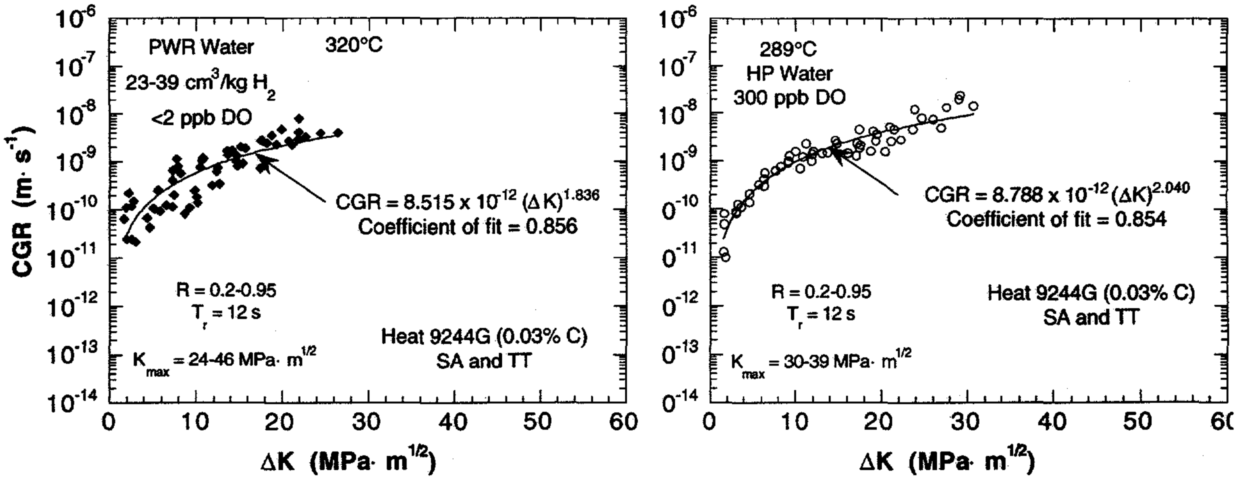

Figure 72. Combined data for dependence on ΔK of CGRs of low-carbon heat of Alloy 600 in simulated PWR (left) and BWR (right) water at 320 and 289°C, respectively

and are lower in water than in air (ratio <1) at higher values of ΔK. For high load ratios (i.e., R ≥ 0.95) and a K_{max} of ≈40 MPa·m$^{1/2}$, which correspond to ΔK values of ≤2 MPa·m$^{1/2}$, the rates in water are higher than in air by a factor of ≈10. Extrapolation of the curves to lower ΔK values, i.e., higher load ratios that approach constant load (R = 1.0), implies even greater

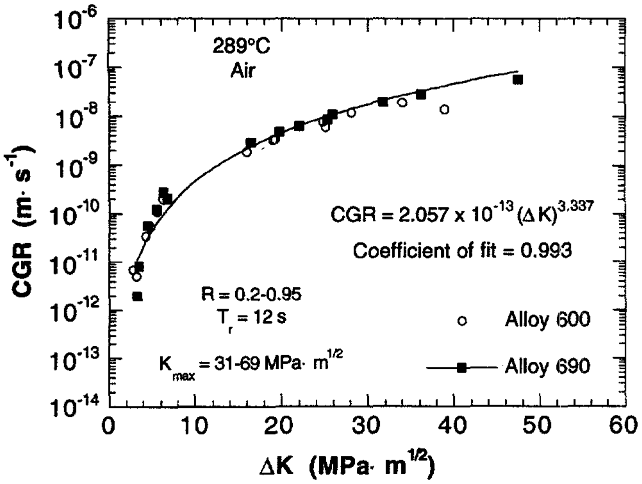

Figure 73.
Dependence on ΔK of CGR of Alloys 600 and 690 in air at 289°C

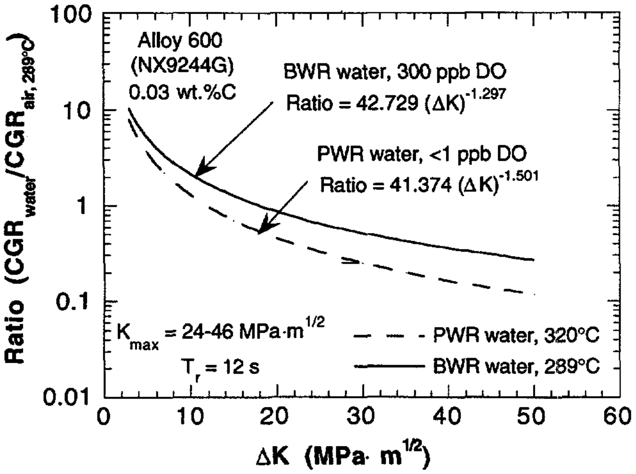

Figure 74.
Dependence on ΔK of ratio of CGRs of solution-annealed and thermally treated low-carbon Alloy 600 in simulated PWR water at 320°C and BWR water at 289°C to CGRs of mill-annealed Alloy 600 in air at 289°C

enhancement of the rates in water; however, this extrapolation leads to considerable uncertainty because the measured rates in both water and air approach the sensitivity of the crack length measurement system under these loading conditions, even in long-term tests (≈1000 h).

4.6 Morphology of Crack Path and Fracture Surface of Specimens

Figures 75-80 show the fracture surface, fracture morphology, and crack path in the crack–tip region of the specimens listed in Tables 15-17. The 1TCT specimens were sectioned vertically, and one–half of each specimen was split in the plane of the crack in liquid nitrogen. Corrosion–product films were removed from the fracture surface by a chemical process to reveal the morphology of the underlying material. The intact portion of the specimen that encompassed the crack was polished and etched to corroborate the mode of crack propagation and also to determine if crack branching had occurred during the test. The total crack lengths at the end of the test were consistent with values obtained by the compliance technique and no branching of the cracks had occurred. The Alloy 600 and 690 specimens from the CGR experiments in simulated PWR water exhibited a transgranular mode of crack propagation. This mode of crack propagation can be attributed to the strong contribution of mechanical cyclic loading in tests at R of 0.2-0.8 and the relatively small degree of crack extension that occurred in tests at R > 0.8.

ALLOY 600	HEAT TREATMENT	LOAD CONDITIONS	ENVIRONMENT
Spec. No. J26-02 **Heat No. NX8844J-26**	**Solution Annealed** **1038°C/1 h**	**K_{max} = 30–42 MPa·m$^{1/2}$** **R = 0.2–0.8** **Freq. = 0.077 Hz**	**PWR: 450 ppm B, 2.25 ppm Li,** **<2, 42, 55 cm^3 H_2·kg^{-1} H_2O,** **<1 ppb DO**

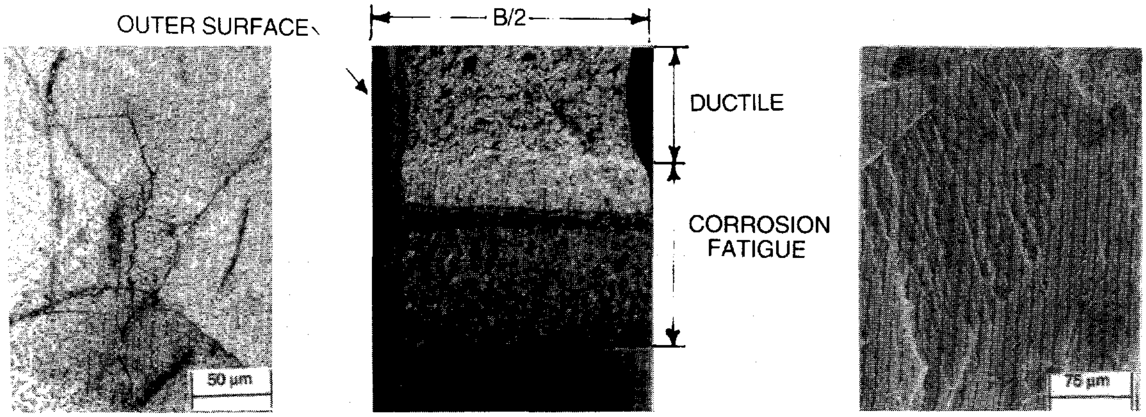

CRACK-TIP REGION   FRACTURE SURFACE   FRACTURE MORPHOLOGY

Figure 75. Crack path, fracture surface, and fracture morphology of 1TCT solution-annealed (1038°C for 1 h) specimen of Alloy 600 (No. J26-02) after crack growth experiment in simulated PWR water at 289°C

ALLOY 690	HEAT TREATMENT	LOAD CONDITIONS	ENVIRONMENT
Spec. No. K1B-02 **Heat No. NX8244HK**	**Solution Annealed** **1093°C/1 h**	**K_{max} = 31–47 MPa·m$^{1/2}$** **R = 0.2–0.8** **Freq. = 0.077 Hz**	**PWR: 450 ppm B, 2.25 ppm Li,** **<2, 42, 55 cm^3 H_2·kg^{-1} H_2O,** **<1 ppb DO**

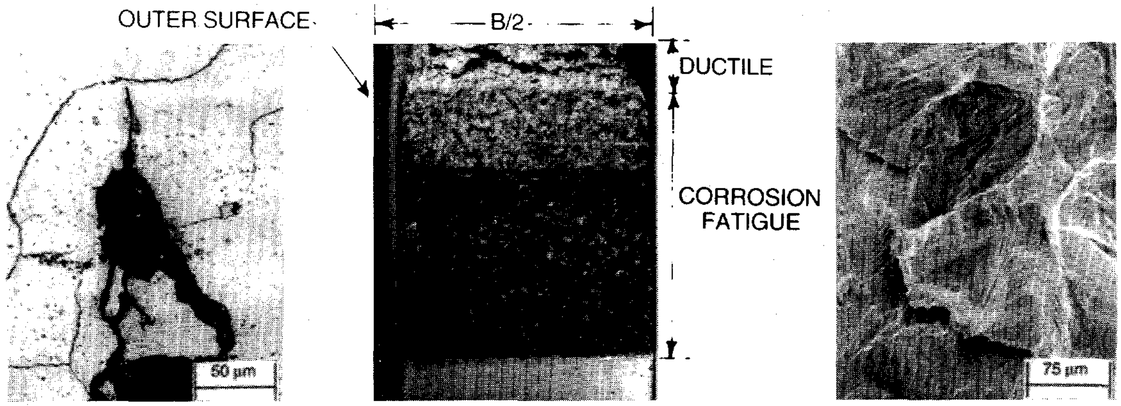

CRACK-TIP REGION   FRACTURE SURFACE   FRACTURE MORPHOLOGY

Figure 76. Crack path, fracture surface, and fracture morphology of 1TCT solution-annealed (1093°C for 1 h) specimen of Alloy 690 (No. K1B-02) after crack growth experiment in simulated PWR water at 289°C

ALLOY 600	HEAT TREATMENT	LOAD CONDITIONS	ENVIRONMENT
Spec. No. J310–01 **Heat No. NX9244G**	**Solution Annealed** **1115°C/2 h**	K_{max} = **26–34 MPa·m$^{1/2}$** **R = 0.3–0.9** **Freq. = 0.077 Hz**	**PWR: 1200 ppm B, 2.25 ppm Li,** **24-31 cm^3 H_2·kg^{-1} H_2O,** **<1 ppb DO**

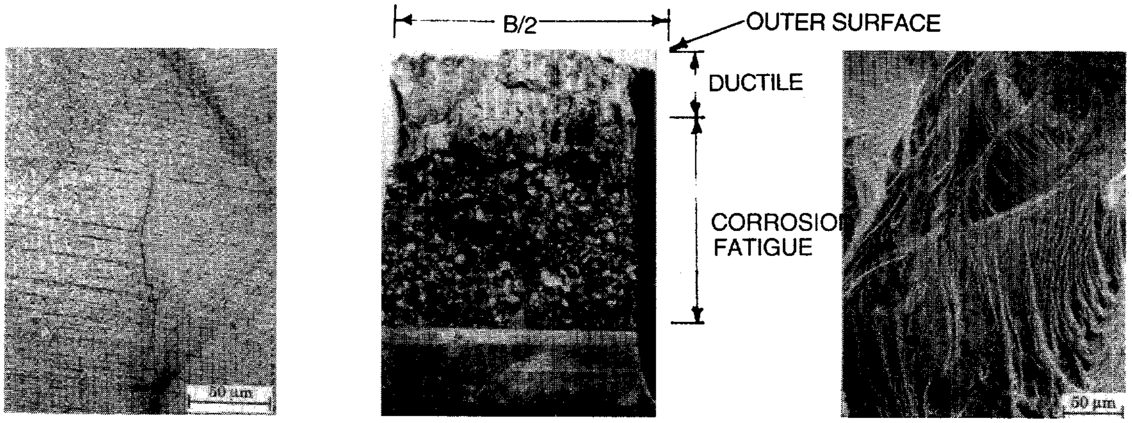

CRACK-TIP REGION

FRACTURE SURFACE

FRACTURE MORPHOLOGY

Figure 77. Crack path, fracture surface, and fracture morphology of 1TCT solution-annealed (1115°C for 2 h) specimen of Alloy 600 (No. J310-01) after crack growth experiment in simulated PWR water at 320°C

ALLOY 600	HEAT TREATMENT	LOAD CONDITIONS	ENVIRONMENT
Spec. No. J311–01 **Heat No. NX9244G**	**Solution Annealed** **1115°C/2 h and** **Thermally Treated** **600°C/24 h**	K_{max} = **25–28 MPa·m$^{1/2}$** **R = 0.3–0.9** **Freq. = 0.077 Hz**	**PWR: 1200 ppm B, 2.25 ppm Li,** **24-31 cm^3 H_2·kg^{-1} H_2O,** **<1 ppb DO**

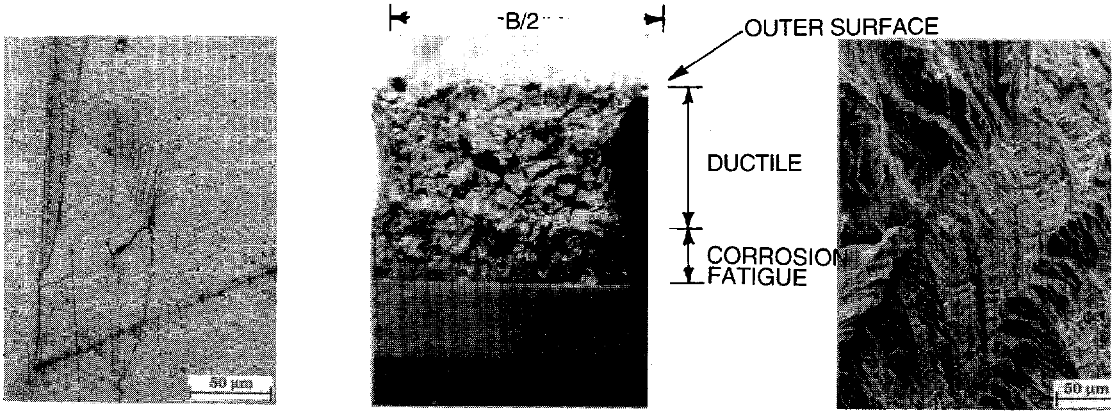

CRACK-TIP REGION

FRACTURE SURFACE

FRACTURE MORPHOLOGY

Figure 78. Crack path, fracture surface, and fracture morphology of 1TCT solution-annealed and thermally treated (1115°C for 2 h and 600°C for 24 h) specimen of Alloy 600 (No. J311-01) after crack growth experiment in simulated PWR water at 320°C

ALLOY 600	**HEAT TREATMENT**	**LOAD CONDITIONS**	**ENVIRONMENT**
Spec. No. J320–01 **Heat No. NX9244G**	**Solution Annealed** **1025°C/2 h**	K_{max} = 25–46 MPa·$m^{1/2}$ R = 0.20–0.95 Freq. = 0.077 Hz	**PWR: 1200 ppm B, 2.25 ppm Li,** **23-39 cm ^{3} H_2·kg^{-1} H_2O,** **<1 ppb DO**

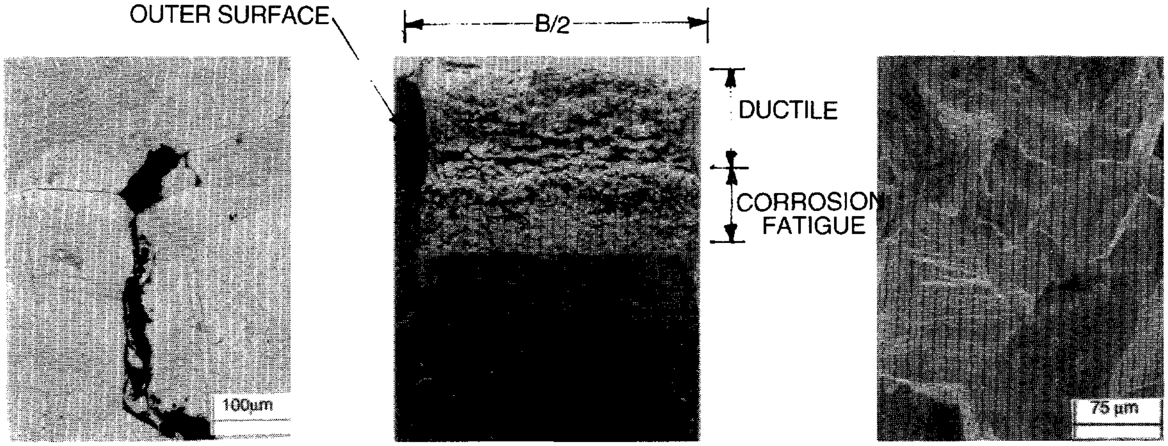

CRACK-TIP REGION FRACTURE SURFACE FRACTURE MORPHOLOGY

Figure 79. Crack path, fracture surface, and fracture morphology of 1TCT solution-annealed (1025°C for 2 h) specimen of Alloy 600 (No. J320-01) after crack growth experiment in simulated PWR water at 320°C

ALLOY 600	**HEAT TREATMENT**	**LOAD CONDITIONS**	**ENVIRONMENT**
Spec. No. J321–01 **Heat No. NX9244G**	**Solution Annealed** **1025°C/2 h and** **Thermally Treated** **600°C/24 h**	K_{max} = 24–40 MPa ·$m^{1/2}$ R = 0.20–0.95 Freq. = 0.077 Hz	**PWR: 1200 ppm B, 2.25 ppm Li,** **23-39 cm^3 H_2·kg^{-1} H_2O,** **<1 ppb DO**

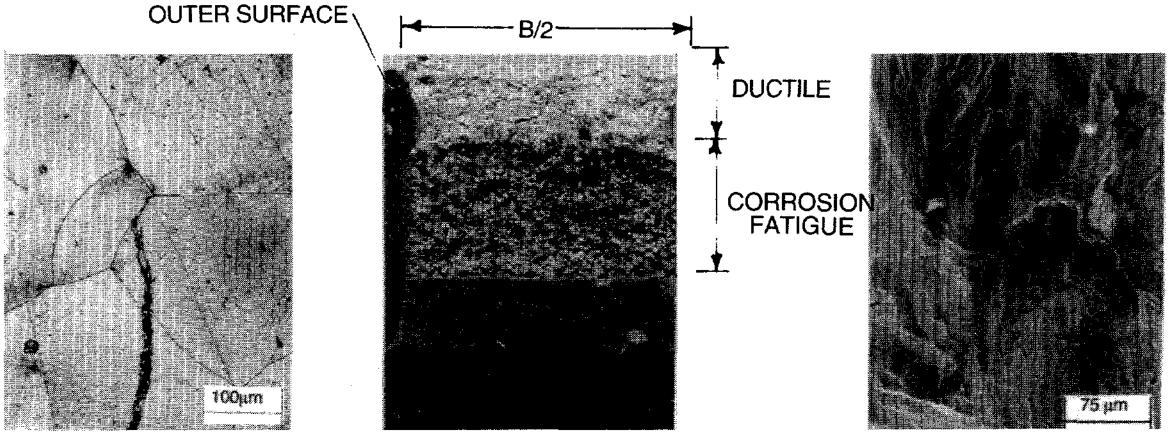

CRACK-TIP REGION FRACTURE SURFACE FRACTURE MORPHOLOGY

Figure 80. Crack path, fracture surface, and fracture morphology of 1TCT solution-annealed and thermally treated (1025°C for 2 h and 600°C for 24 h) specimen of Alloy 600 (No. J321-01) after crack growth experiment in simulated PWR water at 320°C

5 Summary of Results

5.1 Environmental Effects on Fatigue S–N Behavior of Primary Pressure Boundary Materials

Fatigue S–N data have been evaluated to establish the effects of various material and loading variables such as steel type, strain range, strain rate, temperature, sulfur content in steel, orientation, and DO level in water on the fatigue lives of carbon and low-alloy steels (CS and LAS). Current understanding of the fatigue S–N behavior of CS and LAS is given below.

In an air environment, the fatigue life of CS is a factor of ≈1.5 lower than that of LAS. For both steels, life is decreased by a factor of ≈1.5 when temperature is increased from room temperature to 288°C. In the temperature range of dynamic strain aging (200–370°C), some heats of CS and LAS are sensitive to strain rate. The effect of strain rate on fatigue life is not clear; life may be either unaffected, decrease for some heats, or increase for others. In this temperature range, however, cyclic stresses increase with decreasing strain rate. Also, transverse orientations may have poorer fatigue resistance than that of the rolling orientations because of the distribution and morphology of sulfide inclusions. Existing fatigue S–N data indicate that the ASME mean curve for LAS is in good agreement with the experimental data and that for CS is somewhat conservative.

In LWR environments, the fatigue lives of both CS and LAS is decreased significantly when five conditions are satisfied simultaneously, viz., strain amplitude, temperature, DO level in water, and sulfur content in steel are above a minimum level, and strain rate is below a threshold value. Only moderate decrease in life (by a factor of less than 2) is observed when any one of these conditions is not satisfied. The effect of LWR environments on fatigue lives of both CS and LAS is comparable. A minimum threshold strain is required for environmentally assisted decrease in fatigue lives of these steels. The threshold value most likely corresponds to the rupture strain of the surface oxide film. Limited data suggest that the threshold value is ≈20% higher than the fatigue limit for the steel. Environmental effects on fatigue life occur primarily during the tensile–loading cycle, and at strain levels greater than the threshold value required to rupture the surface oxide film. Consequently, loading and environmental conditions during the tensile–loading cycle in excess of the oxide rupture strain, are important parameters for environmentally assisted reduction in fatigue lives of these steels.

When all threshold conditions are satisfied, fatigue life decreases linearly with temperature above 150°C and logarithmically with DO above 0.05 ppm; the effect of DO saturates at ≈0.5 ppm. Also, fatigue life decreases logarithmically with decreasing strain rate below 1%/s; the effect of environment on life saturates at ≈0.001%/s. The existing fatigue S–N data are inadequate to establish unequivocally the effect of sulfur content on the fatigue life of these steels. When any one of the threshold conditions is not satisfied, environmental effects on life are minimal and relatively insensitive to changes in sulfur content. When the threshold conditions are satisfied, the fatigue life of LAS decreases with increasing sulfur content. However, the fatigue life of CS seems to be insensitive to sulfur content in the range of 0.002–0.015 wt.%.

Regarding the mechanism of crack initiation, fatigue life of a material is defined as the number of cycles to form an "engineering" crack, e.g., a 3-mm-deep crack. During cyclic loading, surface cracks of 10 μm or more form quite early in life, i.e., <10% of life even at low strain amplitudes. Fatigue life may be considered to be composed entirely of the growth of these short cracks. Studies on the formation and growth characteristics of short cracks in smooth fatigue specimens in LWR environments indicate that the decrease in fatigue lives of these steels in high–DO water is primarily caused by the effects of environment on the growth of short cracks <100 µm deep. In LWR environments, fatigue crack initiation may be explained as follows: (a) surface microcracks form quite early in fatigue life at persistent slip bands, edges of slip–band extrusions, notches that develop at grain or phase boundaries, or second–phase particles; (b) during cyclic loading, the protective oxide film is ruptured at strains greater than the rupture strain of surface oxides, and the microcracks grow by anodic dissolution/oxidation of the freshly exposed surface to sizes >100 µm; and (c) growth of these large cracks is characterized by accelerating growth rates that may be represented by the proposed ASME Section XI reference curves for these steels in water environments.

Statistical models have been developed to predict fatigue life of small smooth specimens of CS and LAS as a function of various material, loading, and environmental parameters. The functional form and bounding values of these parameters were based upon experimental observations and data trends. The statistical models were obtained by minimizing the squared Cartesian distances from the data point to the predicted curve instead of minimizing the sum of the square of the residual errors for either strain amplitude or fatigue life. The models are recommended for predicted fatigue lives of $\leq 10^6$ cycles. The results indicate that the ASME mean curve for CS is not consistent with the experimental data at strain amplitudes <0.2% or stress amplitudes <410 MPa (<60 ksi); the ASME mean curve is conservative. The statistical model for LAS is comparable with the ASME mean curve.

The design fatigue curves for CS and LAS in LWR environments were obtained by the procedure that has been used to develop the current ASME Code design fatigue curves. The design fatigue curve for a specific service condition is obtained by adjusting the best–fit experimental curve for the effect of mean stress and setting margins of 20 on cycles and 2 on strain to account for the uncertainties in life associated with material and loading conditions. The conservatism in the fatigue design curves has been evaluated. Data available in the literature were reviewed to evaluate the effects of various material, loading, and environmental variables on fatigue life. The results indicate that a factor of at least 1.5 on strain and 10 on cycles is needed to account for the differences and uncertainties in relating the fatigue lives of laboratory test specimens to those of large components.

Sample fatigue evaluations have been performed for CS and LAS components. The values of cumulative usage factor were determined either from the design fatigue curves based on the statistical model or by applying a fatigue life correction factor that was obtained from the statistical model or the correlations developed by EFD committee of Japan. For CS, the approach using a correction factor yields higher values of usage than those determined from the proposed design fatigue curves. The difference arises because the environmentally adjusted design curves not only account for the environment but also for the difference between the ASME mean air curve and statistical model air curve. For CS, this difference can be significant at low stress amplitudes; the current Code design curve yields higher values of fatigue usage.

5.2 Irradiation-Assisted Stress Corrosion Cracking

Slow-strain-rate-tensile tests were conducted on model SS alloys that were irradiated to a fluence of ≈0.45 x 10^{21} n·cm^{-2} (E >1 MeV) at 288°C in helium in the Halden reactor. SSRT tests in simulated BWR water at 288°C were completed for 14 of the alloys. Fractographic analysis by SEM also has been completed to determine susceptibilities to IGSCC and TGSCC. Heat-to-heat variations in susceptibilities to SCC were very significant. High-purity heats of Type 304 and 316 SS exhibited less ductility during SSRT tests and were more susceptible to IGSCC than CP heats. Type 304 SS alloys that contain either high levels of oxygen or sulfur exhibit low ductility, even in the nonirradiated condition.

Total elongation of the irradiated specimens from SSRT tests in simulated BWR water were correlated with the combined concentrations of nitrogen and silicon of the alloys. Alloys that contain low levels of nitrogen (< 0.01 wt.%) and silicon (< 0.5 wt.%) exhibited low ductility, irrespective of the carbon content. Alloys that contain high silicon (≈1.2 wt.%) exhibited low susceptibility to TGSCC and a high ductility despite a very low nitrogen content of ≈0.001 wt.%. A higher silicon content appears to be conducive to less irradiation-induced hardening, a lower density of Frank loops, a lower stacking fault energy, and a lower susceptibility to TGSCC and IGSCC after irradiation. When the nitrogen content was >≈0.015 wt.%, neither low ductility nor high susceptibility to TGSCC was observed regardless of silicon content. As fluence increases, high susceptibility to IGSCC is observed in an alloy that exhibits high susceptibility to TGSCC at low fluence. Therefore, it is desirable to avoid alloys that contain <0.01 wt.% nitrogen and <0.5 wt.% silicon.

To provide a better understanding of cracking of BWR core shroud welds, SMA welds were prepared from Type 304. 304L, and 316 SS plates to simulate BWR core-shroud welds. The microchemistry and microstructure of the welds were characterized by SIMS and TEM. Significant contamination by oxygen and fluorine was observed in HAZs of all SMA welds examined, whereas contamination in GTA welds was insignificant. Contamination occurred by impurities that originate from the coating on the SMA welding electrode and the air atmosphere. Similar contamination was observed in the HAZ of a low-carbon Type 304L SS core shroud weld that cracked in BWR-C.

Cracking incidents in Type 304L SS core shrouds have increased significantly in recent years, and many investigators have suspected that significant grain-boundary chromium depletion can occur in the HAZ of Type 304L SS welds during long-term irradiation under LWR conditions, even if total accumulated fluence is low. However, results of characterization of the HAZ of a specimen of Type 304L SS from the core shroud weld of BWR-C by field-emission-gun advanced analytical electron microscopy showed that grain-boundary carbides and grain-boundary chromium depletion were absent. Similar TEM characterization, conducted on laboratory-produced SMA welds of the Type 304 SSs revealed that grain-boundary carbides, and hence, classical thermal sensitization, were also absent even in the high-carbon materials. An analysis was conducted on the HAZ of a core shroud weld fabricated from Type 304 SS (0.063 wt.%C), which cracked in BWR-D, again revealed that grain-boundary carbides were absent. We believe that high oxygen contamination that is associated with SMA or submerged-arc (SA) welding of a core shrouds is conducive to preferential binding of chromium atoms to oxygen atoms in the weld HAZ, which thereby prevents the formation of chromium-rich $M_{23}C_6$ carbides, even in high-carbon Type 304 SS. In view of these observations, it is difficult to explain BWR core shroud cracking (fabricated from Type 304 or 304L SS) on the basis of either thermal sensitization or grain-boundary chromium-depletion model of IASCC. At the same time, it is important to obtain a crack growth data base from SMA- or SA-welded core shrouds and compare the results with data from TIG-welded or thermally sensitized materials (i.e., materials sensitized in laboratory).

Fluorine content in the heat-affected zone was higher on grain boundaries than in the base metal of core shroud welds. Several literature reports indicate that weld-related fluorine contamination exacerbates the susceptibility of welds to IGSCC during bend-beam tests in water. Because of the direct association of oxygen and fluorine contamination, this type of IGSCC has been termed "oxyfluorine-assisted" SCC. Thus, the failure of Type 304L as well as Type 304 SS core shrouds could be explained by a model based on oxyfluorine-assisted SCC, in which a synergism among oxygen, chromium, and fluorine plays a primary role. According to the model, susceptibility to IGSCC is influenced strongly by oxygen and fluorine on grain boundaries, because higher oxygen is conducive to more chromium bonded to oxygen on the grain boundaries. Hence, higher fluoride ion and lower chromium ion concentrations in the crack-tip water allow the strong catalytic role of fluoride on metal dissolution at the crack tip. The presence of calcium oxyfluoride precipitates appears to exacerbate the process because the precipitates dissolve readily in water, thereby releasing fluorine more rapidly in the crack-tip water.

The equipment for fracture toughness J-R testing of irradiated compact-tension (CT) specimens in a hot cell has been designed, fabricated or procured, and assembled. J–R curve tests are being conducted according to ASTM Specification E 1737 at room temperature and 288°C on nonirradiated specimens to validate the test procedure. The results of preliminary fracture toughness J–R curve and fatigue crack growth tests on two heats of thermally aged CF–8M cast SS have been used to develop correlations for estimating crack lengths from the DC potential and elastic unloading compliance methods.

5.3 Environmentally Assisted Cracking of Low-Carbon Alloys 600 and 690 in Simulated LWR Water

Corrosion–fatigue experiments were conducted on CT specimens of a low-carbon content (0.03 wt.%) heat of Alloy 600 in simulated PWR water to investigate the effects of load ratio and heat treatment condition on CGRs at 320°C. The specimens were fabricated from blocks of material that were solution-annealed at 1025 and 1115°C for 2 h and heat treated at 600°C for 24 h after solution-annealing at the two temperatures. Solution-annealing at 1025 and 1115°C produced ASTM grain sizes of ≈1.0-1.5 and 0.2, respectively, which correspond to large average grain diameters of ≈250-210 and 340 μm. Crack growth experiments were also conducted on solution-annealed specimens of Alloy 600 and 690 in simulated PWR water at 289°C.

"Best-fit" correlations for the CGR of alloys in water versus ΔK were obtained for each specimen and for the combined data from four specimens of the low-carbon Alloy 600 material with the above heat treatments. The effect of low-DO PWR water on the CGRs of this alloy relative to that in air was determined from the ratio of the CGRs in water at 320°C and in air at 289°C. This information was compared with similar data at 289°C for this heat of Alloy 600 in simulated BWR water that contained 300 ppb DO.

Over the stress intensity range ΔK of ≈3 to 47 $\mathrm{MPa \cdot m^{1/2}}$, CGRs of the low-carbon heat of Alloy 600 were higher in simulated BWR than in PWR water. The ratios of the CGRs in water and air were >1 at ΔK values <18 and <10 $\mathrm{MPa \cdot m^{1/2}}$ in BWR and PWR water, respectively, and were lower in water than in air (ratio <1) at higher values of ΔK. For high load ratios (i.e., $R \geq 0.95$) and a K_{max} of ≈40 $\mathrm{MPa \cdot m^{1/2}}$, which correspond to ΔK values of ≤2 $\mathrm{MPa \cdot m^{1/2}}$, the rates in water are higher than in air by a factor of ≈10. The results are consistent with premise that CGRs of nickel-base alloys and austenitic SS increase with DO concentration in high-temperature water. The results suggest that temperature (320 versus 289°C) plays a lesser role in crack propagation because the CGRs are lower in simulated PWR than in BWR water in these experiments despite the higher temperature of the low-DO PWR environment which also contains 23-39 $\mathrm{cm^3 \cdot kg^{-1}}$ H_2, 1200 ppm boron (as H_3BO_3), and 2.25 ppm lithium (as LiOH). Based on results from four specimens in each environment, these heat treatment conditions did not have a significant effect on the CGRs in simulated PWR water. Other heats of material with differing carbon content and heat treatment conditions could produce a wider variation in the results.

The morphology of corrosion–fatigue cracks in the Alloy 600 and 690 specimens was determined. Transgranular cracking occurred in water because of the strong contribution of mechanical cyclic loading in tests at R values of 0.2-0.8 and the relatively small degree of crack extension that occurred in tests at $R > 0.8$.

References

1. K. Iida, *A Review of Fatigue Failures in LWR Plants in Japan*, Nucl. Eng. Des. **138**, 297–312 (1992).

2. D. A. Hale, S. A. Wilson, E. Kiss, and A. J. Gianuzzi, *Low Cycle Fatigue Evaluation of Primary Piping Materials in a BWR Environment*, GEAP-20244, U.S. Nuclear Regulatory Commission (Sept. 1977).

3. D. A. Hale, S. A. Wilson, J. N. Kass, and E. Kiss, *Low Cycle Fatigue Behavior of Commercial Piping Materials in a BWR Environment*, J. Eng. Mater. Technol. **103**, 15–25 (1981).

4. S. Ranganath, J. N. Kass, and J. D. Heald, *Fatigue Behavior of Carbon Steel Components in High-Temperature Water Environments*, in BWR Environmental Cracking Margins for Carbon Steel Piping, EPRI NP-2406, Electric Power Research Institute, Palo Alto, CA, Appendix 3 (May 1982).

5. S. Ranganath, J. N. Kass, and J. D. Heald, *Fatigue Behavior of Carbon Steel Components in High-Temperature Water Environments*, in Low-Cycle Fatigue and Life Prediction, ASTM STP 770, C. Amzallag, B. N. Leis, and P. Rabbe, eds., American Society for Testing and Materials, Philadelphia, pp. 436–459 (1982).

6. J. B. Terrell, *Fatigue Strength of Smooth and Notched Specimens of ASME SA 106-B Steel in PWR Environments*, NUREG/CR-5136, MEA-2289, Materials Engineering Associates, Inc., Lanham, MD (Sept. 1988).

7. J. B. Terrell, *Effect of Cyclic Frequency on the Fatigue Life of ASME SA-106-B Piping Steel in PWR Environments*, J. Mater. Eng. **10**, 193–203 (1988).

8. N. Nagata, S. Sato, and Y. Katada, *Low-Cycle Fatigue Behavior of Pressure Vessel Steels in High-Temperature Pressurized Water*, ISIJ Intl. **31** (1), 106–114 (1991).

9. M. Higuchi and K. Iida, *Fatigue Strength Correction Factors for Carbon and Low-Alloy Steels in Oxygen-Containing High-Temperature Water*, Nucl. Eng. Des. **129**, 293–306 (1991).

10. M. Higuchi, K. Iida, and Y. Asada, *Effects of Strain Rate Change on Fatigue Life of Carbon Steel in High-Temperature Water*, in Fatigue and Crack Growth: Environmental Effects, Modeling Studies, and Design Considerations, PVP Vol. 306, S. Yukawa, ed., American Society of Mechanical Engineers, New York, pp. 111–116 (1995); also in Proc. of Symposium on Effects of the Environment on the Initiation of Crack Growth, ASTM STP 1298, W. A. Van Der Sluys, R. S. Piascik, and R. Zawierucha, eds., American Society for Testing and Materials, Philadelphia, pp. 216–231 (1997).

11. H. Kanasaki, M. Hayashi, K. Iida, and Y. Asada, *Effects of Temperature Change on Fatigue Life of Carbon Steel in High Temperature Water*, in Fatigue and Crack Growth: Environmental Effects, Modeling Studies, and Design Considerations, PVP Vol. 306, S. Yukawa, ed., American Society of Mechanical Engineers, New York, pp. 117–122 (1995).

12. G. Nakao, H. Kanasaki, M. Higuchi, K. Iida, and Y. Asada, *Effects of Temperature and Dissolved Oxygen Content on Fatigue Life of Carbon and Low–Alloy Steels in LWR Water Environment*, in Fatigue and Crack Growth: Environmental Effects, Modeling Studies, and Design Considerations, PVP Vol. 306, S. Yukawa, ed., American Society of Mechanical Engineers, New York, pp. 123–128 (1995).

13. H. Mimaki, H. Kanasaki, I. Suzuki, M. Koyama, M. Akiyama, T. Okubo, and Y. Mishima, *Material Aging Research Program for PWR Plants*, in Aging Management Through Maintenance Management, PVP Vol. 332, I. T. Kisisel, ed., American Society of Mechanical Engineers, New York, pp. 97–105 (1996).

14. M. Higuchi and K. Iida, *Reduction in Low–Cycle Fatigue Life of Austenitic Stainless Steels in High–Temperature Water*, in Pressure Vessel and Piping Codes and Standards, PVP Vol. 353, D. P. Jones, B. R. Newton, W. J. O'Donnell, R. Vecchio, G. A. Antaki, D. Bhavani, N. G. Cofie, and G. L. Hollinger, eds., American Society of Mechanical Engineers, New York, pp. 79–86 (1997).

15. W. J. Shack and W. F. Burke, *Fatigue of Type 316NG SS*, in Environmentally Assisted Cracking in Light Water Reactors, Semiannual Report, October 1989–March 1990, NUREG/CR–4667 Vol. 10, ANL–91/5, pp. 3–19 (March 1991).

16. O. K. Chopra and W. J. Shack, *Effects of LWR Environments on Fatigue Life of Carbon and Low–Alloy Steels*, in Fatigue and Crack Growth: Environmental Effects, Modeling Studies, and Design Considerations, PVP Vol. 306, S. Yukawa, ed., American Society of Mechanical Engineers, New York, pp. 95–109 (1995).

17. O. K. Chopra and W. J. Shack, *Effects of Material and Loading Variables on Fatigue Life of Carbon and Low–Alloy Steels in LWR Environments*, in Transactions of 13th Int. Conf. on Structural Mechanics in Reactor Technology (SMiRT 13), Vol. II, M. M. Rocha and J. D. Riera, eds., Escola de Engenharia – Universidade Federal do Rio Grande do Sul, Porto Alegre, Brazil, pp. 551–562 (1995).

18. O. K. Chopra and W. J. Shack, *Evaluation of Effects of LWR Coolant Environments on Fatigue Life of Carbon and Low–Alloy Steels*, in Proc. of Symposium on Effects of the Environment on the Initiation of Crack Growth, ASTM STP 1298, W. A. Van Der Sluys, R. S. Piascik, and R. Zawierucha, eds., American Society for Testing and Materials, Philadelphia, pp. 247–266 (1997).

19. O. K. Chopra and D. J. Gavenda, *Effects of LWR Coolant Environments on Fatigue Lives of Austenitic Stainless Steels*, in Pressure Vessel and Piping Codes and Standards, PVP Vol. 353, D. P. Jones, B. R. Newton, W. J. O'Donnell, R. Vecchio, G. A. Antaki, D. Bhavani, N. G. Cofie, and G. L. Hollinger, eds., American Society of Mechanical Engineers, New York, pp. 87–97 (1997).

20. D. J. Gavenda, P. R. Luebbers, and O. K. Chopra, *Crack Initiation and Crack Growth Behavior of Carbon and Low–Alloy Steels*, in Fatigue and Fracture 1, PVP Vol. 350, S. Rahman, K. K. Yoon, S. Bhandari, R. Warke, and J. M. Bloom, eds., American Society of Mechanical Engineers, New York, pp. 243–255 (1997).

21. O. K. Chopra and W. J. Shack, *Effects of LWR Coolant Environments on Fatigue S–N Curves for Carbon and Low–Alloy Steels*, in Pressure Vessel and Piping Code and Standards, PVP Vol. 339, T. S. Esselman, ed., American Society of Mechanical Engineers, New York, pp. 185–198 (1996).

22. W. A. Van Der Sluys, *Evaluation of the Available Data on the Effect of the Environment on the Low Cycle Fatigue Properties in Light Water Reactor Environments*, in Proc. 6th Int. Symp. on Environmental Degradation of Materials in Nuclear Power Systems – Water Reactors, R. E. Gold and E. P. Simonen, eds., The Metallurgical Society, Warrendale, PA, pp. 1–4 (1993).

23. S. Majumdar, O. K. Chopra, and W. J. Shack, *Interim Fatigue Design Curves for Carbon, Low–Alloy, and Austenitic Stainless Steels in LWR Environments*, NUREG/CR–5999, ANL–93/3 (April 1993).

24. J. Keisler, O. K. Chopra, and W. J. Shack, *Fatigue Strain–Life Behavior of Carbon and Low–Alloy Steels, Austenitic Stainless Steels, and Alloy 600 in LWR Environments*, NUREG/CR–6335, ANL–95/15 (Aug. 1995).

25. J. Keisler, O. K. Chopra, and W. J. Shack, *Statistical Models for Estimating Fatigue Strain–Life Behavior of Pressure Boundary Materials in Light Water Reactor Environments*, Nucl. Eng. Des. **167**, 129–154 (1996).

26. W. A. Van Der Sluys and S. Yukawa, *Status of PVRC Evaluation of LWR Coolant Environmental Effects on the S–N Fatigue Properties of Pressure Boundary Materials*, in Fatigue and Crack Growth: Environmental Effects, Modeling Studies, and Design Considerations, S. Yukawa, ed., American Society of Mechanical Engineers, New York, pp. 47–58 (1995).

27. A. G. Ware, D. K. Morton, and M. E. Nitzel, *Application of NUREG/CR–5999 Interim Design Curves to Selected Nuclear Power Plant Components*, NUREG/CR–6260, INEL–95/0045 (March 1995).

28. F. P. Ford, S. Ranganath, and D. Weinstein, *Environmentally Assisted Fatigue Crack Initiation in Low–Alloy Steels – A Review of the Literature and the ASME Code Design Requirements*, EPRI Report TR–102765 (Aug. 1993).

29. F. P. Ford, *Quantitative Prediction of Environmentally Assisted Cracking*, Corros. **52** (5), 375–395 (1996).

30. T. T. Pleune and O. K. Chopra, *Artificial Neural Networks and Effects of Loading Conditions on Fatigue Life of Carbon and Low–Alloy Steels*, in Fatigue and Fracture 1, PVP Vol. 350, S. Rahman, K. K. Yoon, S. Bhandari, R. Warke, and J. M. Bloom, eds., American Society of Mechanical Engineers, New York, pp. 413–423 (1997).

31. W. H. Cullen, M. Kemppainen, H. Hänninen, and K. Törrönen, *The Effects of Sulfur Chemistry and Flow Rate on Fatigue Crack Growth Rates in LWR Environments*, NUREG/CR-4121 (1985).

32. J. H. Bulloch, *A Review of the Fatigue Crack Extension Behaviour of Ferritic Reactor Pressure Vessels Materials in Pressurized Water Reactor Environments*, Res. Mech. **26**, 95–172 (1989).

33. W. A. Van Der Sluys and R. H. Emanuelson, *Environmental Acceleration of Fatigue Crack Growth in Reactor Pressure Vessel Materials and Environments*, in Environmentally Assisted Cracking: Science and Engineering, ASTM STP 1049, W. B. Lisagor, T. W. Crooker, and B. N. Leis, eds., American Society for Testing and Materials, Philadelphia, pp. 117–135 (1990).

34. Van Der Sluys, W. A., and Emanuelson, R. H., *Environmental Acceleration of Fatigue Crack Growth in Reactor Pressure Vessel Materials*, EPRI Report TR-102796 (Aug. 1993).

35. T. A. Auten, S. Z. Hayden, and R. H. Emanuelson, *Fatigue Crack Growth Rate Studies of Medium Sulfur Low Alloy Steels Tested in High Temperature Water*, in Proc. 6th Int. Symp. on Environmental Degradation of Materials in Nuclear Power Systems – Water Reactors, R. E. Gold and E. P. Simonen, eds., The Metallurgical Society, Warrendale, PA, pp. 35–40 (1993).

36. J. D. Atkinson, J. Yu, and Z.-Y. Chen, *An Analysis of the Effects of Sulfur Content and Potential on Corrosion Fatigue Crack Growth in Reactor Pressure Vessel Steels*, Corros. Sci. **38** (5), 755–765 (1996).

37. G. L. Wire and Y. Y. Li, *Initiation of Environmentally-Assisted Cracking in Low-Alloy Steels*, in Fatigue and Fracture – 1996 – Volume 1, PVP Vol. 323, H. S. Mehta, ed., American Society of Mechanical Engineers, New York, pp. 269–289 (1996).

38. L. A. James, H. B. Lee, G. L. Wire, S. R. Novak, and W. H. Cullen, *Corrosion Fatigue Crack Growth in Clad Low-Alloy Steels – Part II: Water Flow Rate Effects in High-Sulfur Plate Steel*, J. Pressure Vessel Technol. **119** (3), pp. 255–263 (1997).

39. O. K. Chopra, D. J. Gavenda, and W. J. Shack, in *Environmentally Assisted Cracking in Light Water Reactors, Semiannual Report, October 1994–March 1995*, NUREG/CR-4667 Vol. 20, ANL-95/41, pp. 1–19 (Jan. 1996).

40. E. Lenz, N. Wieling, and H. Munster, *Influence of Variation of Flow Rates and Temperature on the Cyclic Crack Growth Rate under BWR Conditions*, in Proc. 3rd Int. Symp. on Environmental Degradation of Materials in Nuclear Power Systems – Water Reactors, G. J. Theus and J. R. Weeks, eds., The Metallurgical Society, Warrendale, PA, pp. 283–288 (1988).

41. L. A. James, G. L. Wire, and W. H. Cullen, *The Effect of Water Flow Rate Upon the Environmentally-Assisted Cracking Response of a Low-Alloy Steel*, J. Pressure Vessel Technol. **117** (3), 238–244 (1995).

42. O. K. Chopra, W. F. Michaud, W. J. Shack, and W. K. Soppet, in *Environmentally Assisted Cracking in Light Water Reactors, Semiannual Report, April–September 1993*, NUREG/CR-4667 Vol. 17, ANL-94/16, pp. 1–22 (June 1994).

43. K. J. Miller, *Damage in Fatigue: A New Outlook*, in Pressure Vessels and Piping Codes and Standard: Volume 1 – Current Applications, PVP Vol. 313-1, K. R. Rao and Y. Asada, eds., American Society of Mechanical Engineers, New York, pp. 191–192 (1995).

44. C. M. Suh, R. Yuuki, and H. Kitagawa, *Fatigue Microcracks in a Low Carbon Steel*, Fatigue Fract. Engng. Mater. Struct. **8**, 193–203 (1985).

45. N. E. Dowling, *Crack Growth During Low–Cycle Fatigue of Smooth Axial Specimens*, in Cyclic Stress–Strain and Plastic Deformation Aspects of Fatigue Crack Growth, ASTM STP 637, American Society for Testing and Materials, Philadelphia, pp. 97–121 (1977).

46. K. Tokaji, T. Ogawa, and S. Osako, *The Growth of Microstructurally Small Fatigue Cracks in a Ferritic–Pearlitic Steel*, Fatigue Fract. Engng. Mater. Struct. **11**, 331–342 (1988).

47. K. Tokaji, T. Ogawa, and Y. Harada, *The Growth of Small Fatigue Cracks in a Low Carbon Steel; The Effect of Microstructure and Limitations of Linear Elastic Fracture Mechanics*, Fatigue Fract. Engng. Mater. Struct. **9**, 205–217 (1986).

48. M. W. Brown, *Interface Between Short, Long, and Non–Propagating Cracks*, in The Behavior of Short Cracks, EGF Pub. 1, M. J. Miller and E. R. de los Rios, eds., Mechanical Engineering Publication, London, pp. 423–439 (1986).

49. K. Tokaji and T. Ogawa, *The Growth of Microstructurally Small Fatigue Cracks in Metals*, in Short Fatigue Cracks, ESIS 13, M. J. Miller and E. R. de los Rios, eds., Mechanical Engineering Publication, London, pp. 85–99 (1992).

50. K. Tokaji, T. Ogawa, Y. Harada, and Z. Ando, *Limitations of Linear Elastic Fracture Mechanics in Respect of Small Fatigue Cracks and Microstructure*, Fatigue Fract. Engng. Mater. Struct. **9**, 1–14 (1986).

51. E. R. de los Rios, Z. Tang, and K. J. Miller, *Short Crack Fatigue Behavior in a Medium Carbon Steel*, Fatigue Fract. Engng. Mater. Struct. **7**, 97–108 (1984).

52. E. R. de los Rios, A. Navarro, and K. Hussain, *Microstructural Variations in Short Fatigue Crack Propagation of a C–Mn Steel*, in Short Fatigue Cracks, ESIS 13, M. J. Miller and E. R. de los Rios, eds., Mechanical Engineering Publication, London, pp. 115–132 (1992).

53. J. D. Atkinson, J. H. Bulloch, and J. E. Forrest, *A Fractographic Study of Fatigue Cracks Produced in A533B Pressure Vessel Steel Exposed to Simulated PWR Primary Water Environments*, in Proc. 2nd Int. Atomic Energy Agency Specialists' Meeting on Subcritical Crack Growth, NUREG/CP-0067, MEA-2090, Vol. 2, pp. 269–290 (April 1986).

54. H. Hänninen, K. Törrönen, M. Kempainen, and S. Salonen, *On the Mechanisms of Environment Sensitive Cyclic Crack Growth of Nuclear Reactor Pressure Vessel Steels*, Corros. Sci. **23**, 663–679 (1983).

55. K. Törrönen, M. Kempainen, and H. Hänninen, *Fractographic Evaluation of Specimens of A533B Pressure Vessel Steel*, EPRI Report NP-3483, Project 1325-7 (May 1984).

56. E. D. Eason, E. E. Nelson, and J. D. Gilman, *Modeling of Fatigue Crack Growth Rate for Ferritic Steels in Light Water Reactor Environments*, PVP-Vol. 286, Changing Priorities of Code and Standards, ASME, pp. 131–142 (1994).

57. H. S. Mehta and S. R. Gosselin, *An Environmental Factor Approach to Account for Reactor Water Effects in Light Water Reactor Pressure Vessel and Piping Fatigue Evaluations*, EPRI Report TR-105759 (Dec. 1995).

58. H. S. Mehta and S. R. Gosselin, *An Environmental Factor Approach to Account for Reactor Water Effects in Light Water Reactor Pressure Vessel and Piping Fatigue Evaluations*, in Fatigue and Fracture Volume 1, PVP Vol. 323, H. S. Mehta, ed., American Society of Mechanical Engineers, New York, pp. 171–185 (1996).

59. M. E. Mayfield, E. C. Rodabaugh, and R. J. Eiber, *A Comparison of Fatigue Test Data on Piping with the ASME Code Fatigue Evaluation Procedure*, ASME paper 79-PVP-92, American Society of Mechanical Engineers, New York (1979).

60. L. F. Kooistra, E. A. Lange, and A. G. Pickett, *Full-Size Pressure Vessel Testing and Its Application to Design*, J. Eng. Power **86**, 419–428 (1964).

61. A. F. Deardorff and J. K. Smith, *Evaluation of Conservatisms and Environmental Effects in ASME Code, Section III, Class 1 Fatigue Analysis*, SAND94-0187, prepared by Structural Integrity Associates, Inc., San Jose, CA, under contract to Sandia National Laboratories, Albuquerque (Aug. 1994).

62. J.-H. Park and H. M. Chung, *in Environmentally Assisted Cracking in Light Water Reactors, Semiannual Report, January 1996-June 1996*, NUREG/CR-4667 Vol. 22, ANL-97/9, pp. 44-48 (June 1997).

63. J.-H. Park and H. M. Chung, *in Environmentally Assisted Cracking in Light Water Reactors, Semiannual Report, July 1996-December 1996*, NUREG/CR-4667 Vol. 23, ANL-97/10, pp. 35-40 (Oct. 1997).

64. H. M. Chung and J. E. Sanecki, *in Environmentally Assisted Cracking in Light Water Reactors, Semiannual Report, April 1995-December 1995*, NUREG/CR-4667 Vol. 21, ANL-96/1, pp. 44-49 (July 1996).

65. H. M. Chung, W. E. Ruther, J. E. Sanecki, A. G. Hins, N. J. Zaluzec, and T. F. Kassner, *Irradiation-Assisted Stress Corrosion Cracking of Austenitic Stainless Steels: Recent Progress and New Approaches*, J. Nucl. Mater. **239**, 61-79 (1996).

66. C. T. Ward, D. L. Mathis, and R. W. Staehle, *Intergranular Attack of Sensitized Austenitic Stainless Steels by Water Containing Fluoride Ions*, Corrosion **25**, 394-396 (1969).

67. W. E. Berry, E. L. White, and W. K. Boyd, Corrosion **29**, *Stress Corrosion Cracking of Sensitized Stainless Steel in Oxygenated High Temperature Water*, 451-469 (1973).

68. G. J. Theus and J. R. Gels, in *Corrosion Problems in Energy Conversion and Generation*, C. S. Tedmon, Jr., ed., The Electrochemical Society, pp. 384–396 (1974).

69. P. E. C. Bryant and P. R. Habicht, *Fluorine–Induced Intergranular Corrosion of Sensitized Austenitic and Austenoferritic Stainless Steels*, Combustion Engineering Internal Report TIS–5065, also in Proc. IAEA Workshop on Stress Corrosion Cracking, March 29-31, 1976.

70. M. Takemoto, T. Shonohara, M. Shirai, and T. Shinogaya, *External Stress Corrosion Cracking (ESCC) of Austenitic Stainless Steel*, Mater. Perform. **24(6)**, 26-32 (1985).

71. N. C. Huang and Z. Nagy, *Kinetics of the Ferrous/Ferric Electrode Reaction in the Absence of Chloride Catalysis*, J. Electrochem. Soc. **134**, 2215-2220 (1987).

72. F. Zucchi, G. Trabanelli, and G. Demertzis, *The Intergranular Stress Corrosion Cracking of Sensitized AISI 304 in NaF and NaCl Solutions*, Corros. Sci. **28**, 69-79 (1988).

73. P. L. Andresen, in *Proc. EPRI Workshop on Significance and Control of Chromate in BWRs*, Nov. 13–14, 1990, Chicago.

74. C. K. Lee and H. C. Shih, *Effect of Halide Ions on Electrochemical Behavior of Stress Corrosion Cracking of 67/33 α-Brass in Aqueous Environments*, Corrosion **52**, 690-696 (1996).

75. K. Shimizu, K. Kobayashi, G. E. Thompson, P. Skeldon, and G. C. Wood, *The Migration of Fluoride Ions in Growing Anodic Oxide Films on Tantalum*, J. Electrochem. Soc. **144**, 418-423 (1997).

76. T. H. Hughes and E. E. Gruber, *Development of Hot-Cell J-R Test Facility*, in Environmentally Assisted Cracking in Light Water Reactors, Semiannual Report, July-December 1996, NUREG/CR–4667 Vol. 23, ANL–97/10, pp. 42-52 (Oct. 1997).

77. O. K. Chopra, *Estimation of Fracture Toughness of Cast Stainless Steels During Thermal Aging in LWR Systems*, NUREG/CR–4513 Rev. 1, ANL–93/22 (Aug. 1994).

78. A. Saxena and S. J. Hudak, *Review and Extension of Compliance Information for Common Crack Growth Specimens*, Int. J. Fracture **14**, 453-468 (1978).

79. W. E. Ruther, W. K. Soppet, and T. F. Kassner, *Corrosion Fatigue of Alloys 600 and 690 in Simulated LWR Environments*, NUREG/CR–6383, ANL–95/37 (April 1996).

80. W. E. Ruther, W. K. Soppet, D. J. Gavenda, and T. F. Kassner, *Environmentally Assisted Cracking of Alloys 600 and 690 in Simulated LWR Water*, in Environmentally Assisted Cracking in Light Water Reactors, Semiannual Report, October 1994-March 1995, NUREG/CR–4667 Vol. 20, ANL–95/41, pp. 20–30 (Jan. 1996).

81. W. E. Ruther, W. K. Soppet, and T. F. Kassner, *Environmentally Assisted Cracking of Alloys 600 and 690 in Simulated LWR Water,* in Environmentally Assisted Cracking in Light Water Reactors, Semiannual Report, January 1996-June 1996, NUREG/CR-4667 Vol. 22, ANL-97/9, pp. 49–68 (June 1997).

82. W. E. Ruther, W. K. Soppet, and T. F. Kassner, *Environmentally Assisted Cracking of Alloys 600 and 690 in Simulated LWR Water,* in Environmentally Assisted Cracking in Light Water Reactors, Semiannual Report, July 1996-December 1996, NUREG/CR-4667 Vol. 23, ANL-97/10, pp. 52–67 (Oct. 1997).

NRC FORM 335
(2-89)
NRCM 1102,
3201, 3202

U.S. NUCLEAR REGULATORY COMMISSION

BIBLIOGRAPHIC DATA SHEET

(See instructions on the reverse)

1. REPORT NUMBER
(Assigned by NRC, Add Vol., Supp., Rev., and Addendum Numbers, if any.)

NUREG/CR-4667, Vol. 24
ANL-98/6

2. TITLE AND SUBTITLE

Environmentally Assisted Cracking in Light-Water Reactors
Semiannual Report January 1997-June 1997

3. DATE REPORT PUBLISHED

MONTH	YEAR
April	1998

4. FIN OR GRANT NUMBER

W6610

5. AUTHOR(S)

O. K. Chopra, H. M. Chung, E. E. Gruber/ANL
T. M. Karlsen/OECD
T. F. Kassner, J.-H. Park, W. E. Ruther/ANL
J. E. Sanecki, W. J. Shack, J. L. Smith/ANL
W. K. Soppet, R. V. Strain, N. J. Zaluzec/ANL

6. TYPE OF REPORT

Technical: Semiannual

7. PERIOD COVERED *(Inclusive Dates)*

January 1997-June 1997

8. PERFORMING ORGANIZATION - NAME AND ADDRESS *(If NRC, provide Division, Office or Region, U.S. Nuclear Regulatory Commission, and mailing address; if contractor, provide name and mailing address.)*

Argonne National Laboratory
9700 South Cass Avenue
Argonne, IL 60439

Subcontractor:
OECD Halden Reactor Project
Halden N-1751
Norway

9. SPONSORING ORGANIZATION - NAME AND ADDRESS *(If NRC, type "Same as above"; if contractor, provide NRC Division, Office or Region, U.S. Nuclear Regulatory Commission, and mailing address.)*

Division of Engineering Technology
Office of Nuclear Regulatory Research
U.S. Nuclear Regulatory Commission
Washington, DC 20555-0001

10. SUPPLEMENTARY NOTES

M. B. McNeil, NRC Project Manager

11. ABSTRACT *(200 words or less)*

This report summarizes work performed by Argonne National Laboratory on fatigue and environmentally assisted cracking (EAC) in light water reactors from January 1997 to June 1997. Topics that have been investigated include (a) fatigue of carbon, low–alloy, and austenitic stainless steels (SSs) used in reactor piping and pressure vessels, (b) irradiation–assisted stress corrosion cracking of Types 304 and 304L SS, and (c) EAC of Alloys 600 and 690. Fatigue tests were conducted on ferritic and austenitic SSs in water that contained various concentrations of dissolved oxygen (DO) to determine whether a slow strain rate applied during various portions of a tensile–loading cycle is equally effective in decreasing fatigue life. Slow–strain–rate–tensile tests were conducted in simulated boiling water reactor (BWR) water at 288°C on SS specimens irradiated to a low fluence in the Halden reactor and the results were compared with similar data from a control–blade sheath and neutron-absorber tubes irradiated in BWRs to the same fluence level. Crack–growth–rate tests were conducted on compact–tension specimens from several heats of Alloys 600 and 690 in low-DO, simulated pressurized water reactor environments.

12. KEY WORDS/DESCRIPTORS *(List words or phrases that will assist researchers in locating the report.)*

Corrosion Fatigue
Crack Growth
Irradiation-Assisted Stress Corrosion Cracking
Radiation-Induced Segregation
Stress Corrosion Cracking
A106-Gr B Steel
A533-Gr B Steel
Type s 304, 304L, 316, and 316NG Stainless Steel
Alloys 600 and 690

13. AVAILABILITY STATEMENT

unlimited

14. SECURITY CLASSIFICATION

(This Page)
unclassified

(This Report)
unclassified

15. NUMBER OF PAGES

16. PRICE